DETECTION AND CHARACTERISATION OF VESSELS IN RETINAL IMAGES

By

Temitope Mapayi

213554614

A thesis submitted in fulfillment of the academic requirements for the Degree of Doctor of Philosophy in the School of Mathematics, Statistics & Computer Science, College of Agriculture, Engineering and Science, University of KwaZulu-Natal, Durban, South Africa.

May 2015

UNIVERSITY OF KWAZULU-NATAL

COLLEGE OF AGRICULTURE, ENGINEERING AND SCIENCE

DECLARATION

The research described in this thesis was conducted at the University of KwaZulu-Natal under the supervision of Prof. S. Viriri and Prof. Jules-Raymond Tapamo. I hereby declare that all the materials incorporated in this thesis are my own original work except where acknowledgement is made by name or in the form of a reference. The work contained herein has not been submitted in part or whole for a degree at any other university.

Signed:.....
Temitope Mapayi
Date: May 2015

As the candidate's supervisor, I have approved / disapproved this dissertation for submission

Signed:.....
Prof. Serestina Viriri
Date: May 2015

Signed:.....
Prof. Jules-Raymond Tapamo
Date: May 2015

UNIVERSITY OF KWAZULU-NATAL

COLLEGE OF AGRICULTURE, ENGINEERING AND SCIENCE

DECLARATION 1 - PLAGIARISM

I, Temitope Mapayi, declare that:

A. The research reported in this thesis, except where otherwise indicated, is my original research.

B. This thesis has not been submitted for any degree or examination at any other university.

C. This thesis does not contain other persons' data, pictures, graphs or other information, unless specifically acknowledged as being sourced from other persons.

D. This thesis does not contain other persons' writing, unless specifically acknowledged as being sourced from other researchers. Where other written sources have been quoted, then:

   (a) Their words have been re-written but the general information attributed to them has been referenced.

   (b) Where their exact words have been used, then their writing has been placed in italics and inside quotation marks, and referenced.

E. This thesis does not contain texts, graphics or tables copied and pasted from the Internet, unless specifically acknowledged, and the source being detailed in the thesis and in the References sections.

Signed:.....

UNIVERSITY OF KWAZULU-NATAL

COLLEGE OF AGRICULTURE, ENGINEERING AND SCIENCE

DECLARATION 2 - PUBLICATIONS

DETAILS OF CONTRIBUTION TO PUBLICATIONS that form part and/or include research presented in this thesis (include publications in preparation, submitted, in press and published and give details of the contributions of each author to the experimental work and writing of each publication)

A. Temitope Mapayi, Serestina Viriri, Jules-Raymond Tapamo: A New Adaptive Thresholding Technique for Retinal Vessel Segmentation Based on Local Homogeneity Information. Lecture Notes in Computer Science (LNCS) - Springer International Publishing Switzerland, Volume 8509, pp 558-567, 2014.

B. Temitope Mapayi, Serestina Viriri, Jules-Raymond Tapamo: Retinal Vessel Segmentation based on K-Means Clustering and Difference Image. Proceedings of the 2014 Annual Symposium of the Pattern Recognition Association of South Africa (PRASA) 27^{th} to 28^{th} of November, 2014. Cape Town, South Africa.

C. Temitope Mapayi, Serestina Viriri, Jules-Raymond Tapamo: Comparative Study of Retinal Vessel Segmentation Based on Global Thresholding Techniques. Computational and mathematical methods in medicine, vol. 2015, 2015.

D. Temitope Mapayi, Serestina Viriri, Jules-Raymond Tapamo: Adaptive Thresholding Technique for Retinal Vessel Segmentation based on GLCM-Energy Information. Computational and mathematical methods in medicine, vol. 2015, 2015.

E. Temitope Mapayi, Serestina Viriri, Jules-Raymond Tapamo: Retinal Vessel Segmentation Based on Phase Congruence and GLCM Sum-

Entropy. 2015 IEEE International Conference on Industrial Technology, 17^{th} to 19^{th} of March, 2015. Seville, Spain.

F. Temitope Mapayi, Serestina Viriri, Jules-Raymond Tapamo: Retinal Vessel Segmentation: A Comparative Study of Fuzzy C-Means and GLCM Sum-Entropy on Phase Congruence. International Journal of Advanced Robotic Systems *(In Press)*

G. Temitope Mapayi, Serestina Viriri, Jules-Raymond Tapamo, Adedayo O. Adio: Automatic Segmentation and Characterisation of Retinal Vessel Using Tortuosity Measures. Machine Vision and Application *(Under Review)*

Signed:.....

This work is dedicated to God, my ALL in ALL

And

to the memory of my late mother, Victoria O. Mapayi

ABSTRACT

As retinopathies such as diabetic retinopathy (DR) and retinopathy of prematurity (ROP) continue to be the major causes of blindness globally, regular retinal examinations of patients can assist in the early detection of the retinopathies. The manual detection of retinal vessels is a very tedious and time consuming task as it requires about two hours to manually detect vessels in each retinal image. Automatic vessel segmentation has been helpful in achieving speed, improved diagnosis and progress monitoring of these diseases but has been challenging due to complexities such as the varying width of the retinal vessels from very large to very small, low contrast of thin vessels with respect to background and noise due to nonhomogeneous illumination in the retinal images. Although several supervised and unsupervised segmentation methods have been proposed in the literature, the segmentation of thinner vessels, connectivity loss of the vessels and time complexity remain the major challenges. In order to address these problems, this research work investigated different unsupervised segmentation approaches to be used in the robust detection of large and thin retinal vessels in a timely efficient manner.

Firstly, this thesis conducted a study on the use of different global thresholding techniques combined with different pre-processing and post-processing techniques. Two histogram-based global thresholding techniques namely, Otsu and Isodata were able to detect large retinal vessels but fail to segment the thin vessels because these thin vessels have very low contrast and are difficult to distinguish from the background tissues using the histogram of the retinal images. Two new multi-scale approaches of computing global threshold based on inverse difference moment and sum-entropy combined with phase congruence are investigated to improve the detection of vessels. One of the findings of this study is that the multi-scale approaches of computing global threshold combined with phase congruence based techniques improved on the detection of large vessels and some of the thin vessels. They, however, failed to maintain the width of the detected vessels. The reduction

in the width of the detected large and thin vessels results in low sensitivity rates while relatively good accuracy rates were maintained. Another study on the use of fuzzy c-means and GLCM sum entropy combined on phase congruence for vessel segmentation showed that fuzzy c-means combined with phase congruence achieved a higher average accuracy rates of 0.9431 and 0.9346 but a longer running time of 27.1 seconds when compared with the multi-scale based sum entropy thresholding combined with phase congruence with the average accuracy rates of 0.9416 and 0.9318 with a running time of 10.3 seconds. The longer running time of the fuzzy c-means over the sum entropy thresholding is, however, attributed to the iterative nature of fuzzy c-means. When compared with the literature, both methods achieved considerable faster running time.

This thesis investigated two novel local adaptive thresholding techniques for the segmentation of large and thin retinal vessels. The two novel local adaptive thresholding techniques applied two different Haralick texture features namely, local homogeneity and energy. Although these two texture features have been applied for supervised image segmentation in the literature, their novelty in this thesis lies in that they are applied using an unsupervised image segmentation approach. Each of these local adaptive thresholding techniques locally applies a multi-scale approach on each of the texture information considering the pixel of interest in relationship with its spacial neighbourhood to compute the local adaptive threshold. The localised multi-scale approach of computing the thresholds handled the challenge of the vessels' width variation. Experiments showed significant improvements in the average accuracy and average sensitivity rates of these techniques when compared with the previously discussed global thresholding methods and state of the art. The two novel local adaptive thresholding techniques achieved a higher reduction of false vessels around the border of the optic disc when compared with some of the previous techniques in the literature. These techniques also achieved a highly improved computational time of 1.9 to 3.9 seconds to segment the vessels in each retinal image when compared with the state of the art. Hence, these two novel local adaptive thresholding techniques are proposed for the segmentation of the vessels in the retinal images.

This thesis further investigated the combination of difference image and k-

means clustering technique for the segmentation of large and thin vessels in retinal images. The pre-processing phase computed a difference image and k-means clustering technique was used for the vessel detection. While investigating this vessel segmentation method, this thesis established the need for a difference image that preserves the vessel details of the retinal image. Investigating the different low pass filters, median filter yielded the best difference image required by k-means clustering for the segmentation of the retinal vessels. Experiments showed that the median filter based difference images combined with k-means clustering technique achieved higher average accuracy and average sensitivity rates when compared with the previously discussed global thresholding methods and the state of the art. The median filter based difference images combined with k-means clustering technique (that is, DIMDF) also achieved a higher reduction of false vessels around the border of the optic disc when compared with some previous techniques in the literature. These methods also achieved a highly improved computational time of 3.4 to 4 seconds when compared with the literature. Hence, the median filter based difference images combined with k-means clustering technique are proposed for the segmentation of the vessels in retinal images.

The characterisation of the detected vessels using tortuosity measure was also investigated in this research. Although several vessel tortuosity methods have been discussed in the literature, there is still need for an improved method that efficiently detects vessel tortuosity. The experimental study conducted in this research showed that the detection of the stationary points helps in detecting the change of direction and twists in the vessels. The combination of the vessel twist frequency obtained using the stationary points and distance metric for the computation of normalised and non-normalised tortuosity index (TI) measure was investigated. Experimental results showed that the non-normalised TI measure had a stronger correlation with the expert's ground truth when compared with the distance metric and normalised TI measures. Hence, a non-normalised TI measure that combines the vessel twist frequency based on the stationary points and distance metric is proposed for the measurement of vessel tortuosity.

ACKNOWLEDGEMENTS

I am highly grateful to the Almighty God, The Father of Mercy and Comfort, to whom I owe my very life and existence. I would like to express my deep appreciation and gratitude to the following people for the help, encouragement and support received to complete this thesis.

To my supervisors, Professor S. Viriri and Professor J.R. Tapamo, I am very grateful. Your candid encouragement, patience and the sacrifice made to read this work over and over is noteworthy. Your passion for scientific discovery has been my inspirational tool for hope.

Thanks to my wife, Oluwatosin Damilola. You were always there to encourage me and stood by me through the good and challenging times. Thanks to my son, Oluwatomi Samuel, for your patience with me in the course of this research. Thanks to my elder sisters, Mrs Oluwafunke Egba, Major Oluwatoyin Adewusi, and brothers, Mr Jide, Mr Oladimeji and Late Mr. Ajibola, for your encouragement and support. To all the Adenitans, you are wonderful and greatly appreciated.

To my fellow members at the Computer Vision, Image Processing and Pattern recognition research group, I really appreciate you all. Thanks to Soren Greenwood, for his technical support. To Mr. Luke Joel, Miss Oluwakorede Oluyide, Dr Christianah Obagbuwa, Mr Olakunle Ogundele, Mr Jude Adeleke and all my fellow post-graduate students at the School of Mathematics, Statistics & Computer Science, University of KwaZulu-Natal, you are all wonderful. Thanks to Dr Jane Morgan for her words of encouragement. To Dr Eddy Kimba, you are such a wonderful office mate.

To my Ophthalmology expert, Dr Adedayo Adio, your swift willingness and availability to offer your expert advice as well as your words of encouragement are wonderful. You are greatly appreciated.

Dr Olujoke Olufemi, Mr. Adedapo Adeyinka, Dr O.W.F Onifade, Dr Olumide Longe, Prof. P.A. Owolawi, Dr Tunde Sawyer Mr and Mrs Olugbenga Imole, Mr Dumbili Emeka, Mr Olaifa Moses and Mr Dada Gbenga, your words of encouragement and support are greatly appreciated.

To all my leaders and friends at WEM, you are all wonderful. Engineer and Mrs Martins Akeredolu, Mr and Mrs. Micheal Adewumi, Mr and Mrs Deino Babayemi, Mr and Mrs Kolade Idowu, Prince Adelaja, Rotimi Oyeleye, Aderogba Adebayo, Sado Emmanuel and a host of others, I appreciate you all.

The Netherlands, Univ. Med. Center Utrecht, Image Science Institute, for granting me access to its DRIVE (Digital Retinal Images for Vessel Extraction) database.

Clemson, SC, Clemson University for granting me access to its STARE (STructured Analysis of the REtina) database.

International Diabetes Federation, for granting me the permission to use their chart.

Contents

List of Tables

List of Figures

List of Algorithms

List of Abbreviations & Acronyms

AFR ..... Africa

ANN ..... Artificial Neural Network

ASM ..... Angular Second Moment

AUC ..... Area under Curve

CLAHE ..... Contrast Limited Adaptive Histogram Equalization

CONTR ..... Contrast

COR ..... Correlation

CT ..... Computed Tomography

DIGF ..... Difference Image Based on Gaussian Filter

DIMDF ..... Difference Image Based on Median Filter

DIMDGF ..... Difference Image Based on Median and Gaussian Filters

DIMDMNF ... Difference Image Based on Median and Mean Filters

DIMNF ..... Difference Image Based on Mean Filter

DIMNGF ..... Difference Image Based on Mean and Gaussian Filters

DR ..... Diabetic Retinopathy

DRIVE ..... Digital Retinal Images for Vessel Extraction

ENER ..... Energy

EUR ..... Europe

FN ..... False Negative

FP ..... False Positive

FPR ..... False Positive Rate

GLCM ..... Gray Level Co-occurrence Matrix

GMM ..... Gaussian Mixture Model

IDF ..... International Diabetes Federation

IDM ..... Inverse Difference Moment

MAP ..... Maximum a Posteriori

MENA ..... Middle East & North Africa

MFR ..... Matched Filter Response

MRI ..... Magnetic Resonance Imaging

NAC ..... North American & Caribbean

OCT ..... Optical Coherence Tomography

PCA ..... Principal Component Analysis

ROC ..... Receiver Operating Characteristic

ROP ..... Retinopathy of Prematurity

SACA ..... South And Central America

SEA ..... South East Asia

SOM ..... Self-Organizing Map

STARE ..... STructured Analysis of the Retina

SVM ..... Support Vector Machines

TI ..... Tortuosity Index

TN ..... True Negative

TP ..... True Positive

TPR ..... True Positive Rate

VAR ..... Variance

WP ..... Western Pacific

Chapter 1

INTRODUCTION

1.1 General Introduction

Medical imaging has become an important tool in medicine today due to the advances in the hardware and software resources used for the acquisition, processing and storage of the images [2], [3], [4], [5]. Medical imaging technology has significantly improved the diagnosis and treatment planning of patients in the various aspects of the medical field [6],[7], [8]. Although some earlier studies have been made on the automatic detection of vessels and lesions in retinal images [9], [10], digital retinal photography and image analysis in ophthalmology are increasingly becoming helpful in the diagnosis and progress monitoring of diabetic retinopathy (DR), retinopathy of prematurity (ROP) and cardiovascular diseases [11], [12], [13], [14], [15], [16]. The use of digital image analysis by ophthalmologist is aimed at improving the reliability of physician's judgment by reducing human error as well as helping to achieve timely accurate diagnosis and progress monitoring of the diseases. This, in turn, assists the ophthalmologists to efficiently manage more patients within reasonable time [17].

Image segmentation is an important step in image analysis that involves the partitioning of a digital image into multiple regions with uniform and homogeneous attributes such as intensity, colour or texture [18]. It is used to locate and detect boundaries and objects of interest in images. Retinal vessel network composed of veins and arteries are elongated features visible in the retinal image. Retinal vessel segmentation is a task in which these vessels are delineated from retinal images using specific visual criteria. Efficient vessel network detection and vessel feature analysis are of great importance in ophthalmology for the diagnosis and progress monitoring of the various retinopathies and vascular diseases [19]. Several automatic methods for retinal vessel

segmentation [20], [21], [22], [23], [24, 25], [26], [27], [28],[29], [30], [31], [32], [33], have been published in the literature. The vessel segmentation techniques are divided into two major categories namely, supervised and unsupervised methods. Supervised methods [20], [22], [23], [28], [32], [34], [35], [36], [37] require some prior labelled training samples for the segmentation of retinal vessels. Although the supervised vessel segmentation techniques [20], [22], [23], [28], [32], [34], [35], [36], [37] have shown higher vessel detection and accuracy rates than the majority of the unsupervised methods [21], [26], [27], [38], [34], [39], [40], [41], [42], reliable labelled training samples by experts which could sometimes be extremely difficult, expensive or unavailable is a major drawback [16]. Moreover, the performance of these techniques is highly dependent on the labelled training sample as a new set of labelled training sample is often required for retraining to obtain good segmentation performance when detecting vessels on a new set of retinal images [28]. Unsupervised vessel segmentation methods [21], [26], [27], [38], [43], [34], [39], [40], [44], [45], [46], [41], [42], on the other hand search and use underlying patterns to classify each pixel in the retinal image as either vessel or background. Although unsupervised vessel segmentation methods are computationally faster when compared with the supervised vessel segmentation methods since no training time is required, there are major drawbacks such as connectivity loss of vessel network [21], [38] and inability to detect thin vessels [38], [39], [42], [47], [48].

Tortuosity has been described to be a reliable vascular morphology feature in differentiating ROP severity [49]. Increase in vessel tortuosity is also one of the first changes in vessels morphology to occur in DR patients [50], [51]. Although several tortuosity measurement techniques [52], [53], [54], [55], [56], [57], [58], [59], [60] have been proposed, none has gained universal acceptance [61].

1.1.1 Diabetic Retinopathy

Diabetes, a disease characterised by abnormal high glucose levels in the blood and excessive urination with persistent thirst, has become a growing menace worldwide [63]. According to the international diabetes federation (IDF) [62], 382 million people were affected by diabetes worldwide in 2013. There has also been a projection of 55% increment in the number of people living with diabetes globally between the years 2013 and 2035 by IDF, with 109% increment in Africa, 96 % in the Middle East and North Africa, 71% in South-East Asia, 60% in South and Central America , 46% in Western Pacific, 37% in North America and Caribbean and 22% in Europe as shown in Figure 1.1. According to the projection, the number of people living with diabetes will have

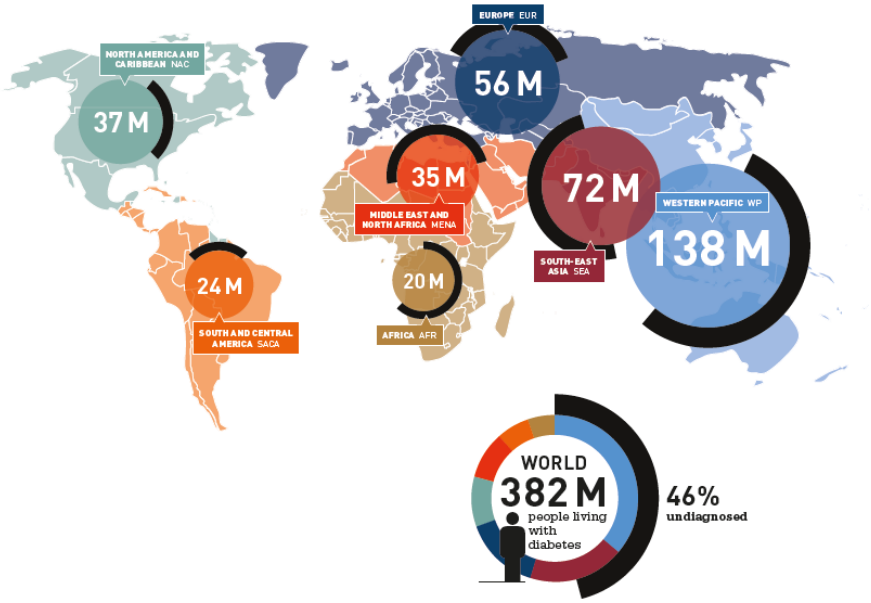

Figure 1.1: Population of People Living With Diabetes in 2013 [62]

increased from 382 million to 592 million people by the year 2035 as shown in Figure 1.2.

DR, an eye disease secondary to diabetes, is a major cause of visual loss and blindness worldwide [64]. Recently, 35% of diabetic patients have been estimated to be living with DR worldwide [65]. There are basically two stages of DR: the early stage, which is the non-proliferative DR and the advanced stage, which is the proliferative DR [66]. Although DR remains symptomless in the early stages [67], retinal vessels are the predominant damage targets of diabetes at these early stages. Different abnormalities such as changes in vessel shape, branching pattern, width, tortuosity, or the appearance of retinal lesions, can be associated with the presence of retinopathies [68]. Regular retinal examinations for diabetic patients can help in an early detection of DR and significant reduction of the cases of blindness [69], [67], [70].

1.1.2 Retinopathy of Prematurity

Retinopathy of prematurity (ROP), a vasoproliferative disease of the eye that affects premature newborns, has become a major cause of blindness to children in many middle income countries [71]. There are at least 50,000 children that are blind due to ROP globally [72]. Literature reports on children in schools for the blind indicated that

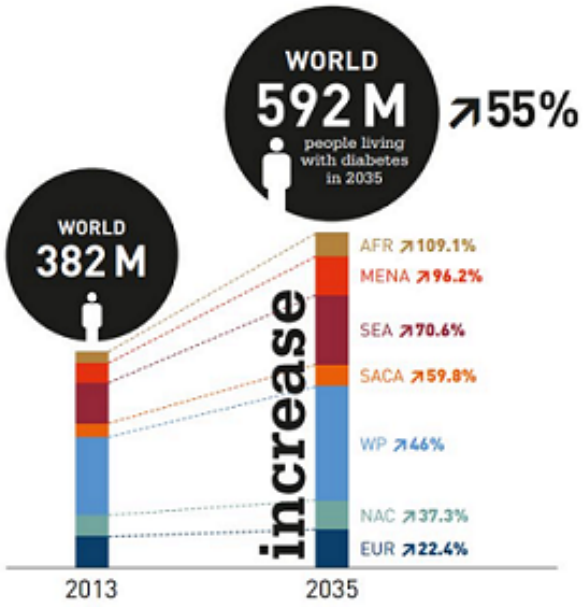

Figure 1.2: Projection of People Living With Diabetes Between 2013 and 2035 [62]

ROP is becoming the main cause of blindness in China, South Asia, Latin America and Eastern Europe [73]. ROP was also responsible for 10.6% of blindness cases of children in schools for the blind in South Africa in 1995 [74]. Using the proxy indicator of infant mortality rates in [75] gives a likely distribution chart of blindness in children resulting from ROP as shown in Figure 1.3.

In order to improve on the prevention of blindness cases due to ROP epidemic, automatic detection and analysis of retinal vessels are currently being explored for the early detection and efficient management of ROP in babies [76].

1.2 Motivation

In the face of the global prevalence of DR and ROP, the cases of vision loss and blindness (as shown in Figure 1.4) tend to increase in the absence of efficient detection and management approaches of the diseases [67]. The families, communities and countries affected by these epidemics are also likely to suffer serious economic setbacks caused by the financial burden, reduced-earnings and reduced-productivity due to visual impairment and blindness [62].

Ophthalmologists, with the help of detected vessel network, focus on retinal vessel feature analysis during the diagnosis of the diseases [77]. Manual detection and analysis

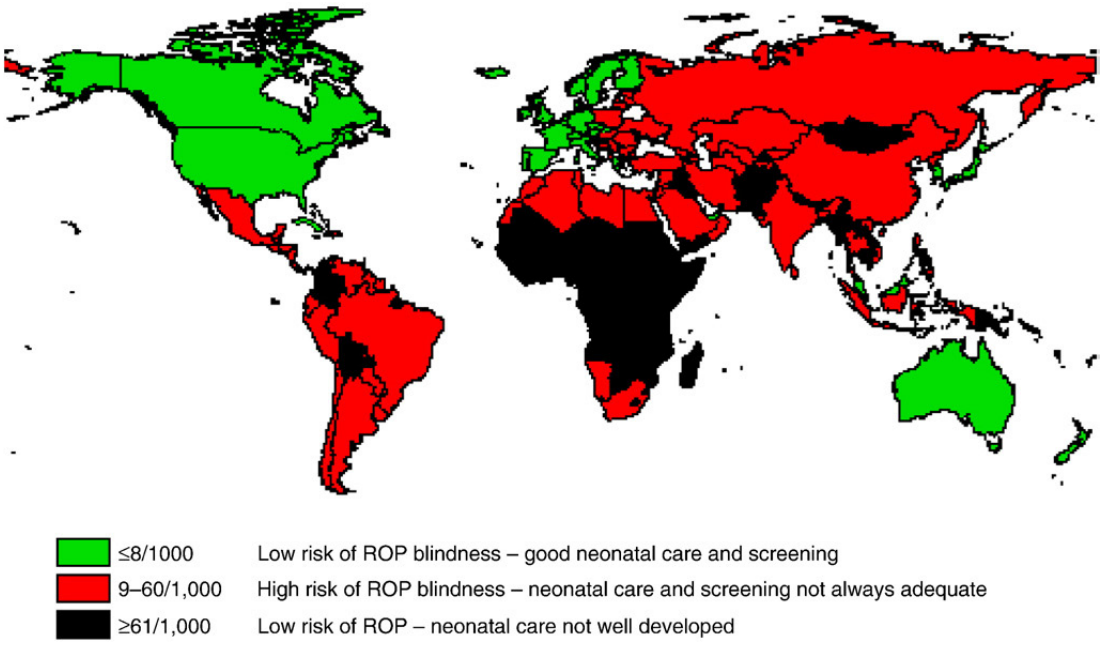

Figure 1.3: Distribution Chart of Children Blindness Due To ROP Using Proxy Indicator of Infant Mortality Rates [75]

of the retinal vessels has been a very tedious and time consuming task that requires about two hours to detect vessels in each retinal image [22] and requires trained and skilled personnel who are often scarce [78], [79], [80]. However, with the help of automatic vasculature segmentation and analysis, ophthalmologist can now diagnose and efficiently manage the diseases [19].

In order to reliably and efficiently diagnose and manage these diseases, ophthalmologists need highly accurate and fast automatic segmentation techniques for the detection of both large and thin vessels in the retinal images.

1.3 Problem Statement

Automated vessel segmentation has been a challenging problem due to complexities such as varying width of retinal vessels from very large to very small, low contrast of thin vessels with respect to background and noise due to nonhomogeneous illumination caused by the complex acquisition of the retinal images [1], [47]. Although existing methods have made great progress in this field, it remains the subject of on-going research as there is need for further improvement. Supervised vessel segmentation techniques are computationally expensive since training time is required [32], [81]. An-

Figure 1.4: Vision Loss and Blindness Caused by Retinopathies

other major drawback of the supervised vessel segmentation techniques is that their performance is highly dependent on the labelled training sample by experts which could sometimes be extremely difficult, expensive or unavailable [16]. Furthermore, a new set of labelled training sample is often required for retraining to obtain good segmentation performance when detecting vessels on a new set of retinal images [22], [28]. Although some unsupervised vessel segmentation methods are computationally fast when compared with the supervised segmentation methods, their major drawbacks are connectivity loss of vessel network and inability to detect thin vessels [21], [38], [39], [42], [47], [48], [82]. While some unsupervised techniques [43], [34], [46], [83], [84] have made some progress at improving the automatic detection of retinal vessels, there is need for further improvement in the detection of thinner vessels and the computational running time required for the segmentation of vessels. The presence of a lot of false positives around the border of the optic disk also remains a challenge in the vessel segmentation techniques [20], [42].

Although several tortuosity measurement techniques [52], [53], [54], [55], [56], [57], [58], [59], [60] have been proposed, results obtained suggest the need for further improvement. The Arc-chord ratio techniques [52], [53], [54], [55], [56] failed to differentiate varying vessels when they have the same length but different number of vessel twists.

Techniques based on inflection points alone are also not robust enough as all the vessels twists are not sufficiently described using them [85]. Although chain code has been applied for vessel tortuosity measurement in [60], the major drawbacks of chain code are the inaccuracies obtained in areas of high curvature and unacceptable errors in the regions of low curvature [86].

1.4 Thesis Objectives

This research aims to propose fast unsupervised segmentation model for an automatic detection of large and thin vessels, and characterise the detected vessel using tortuosity measure. The specific objectives of this research are:

(a) To model a fast unsupervised segmentation technique that detects both large and thin vessels in retinal images.

(b) To optimise the accuracy rate of the detected retinal vessels by minimising false detection of vessels.

(c) To model vessel tortuosity measure that combines distance metric and vessel twists.

1.5 Contributions

The major contributions of this thesis are presented in this section. Firstly, this thesis contributes to knowledge by conducting a comparative study on the use of different global thresholding techniques combined with different pre-processing and post-processing techniques. Through the investigation of the phase congruence-based global thresholding approach and Contrast Limited Adaptive Histogram Equalisation (CLAHE)-based global thresholding approach, this thesis shows that global thresholding techniques are limited in efficiently segmenting thin vessels in retinal images. This thesis also shows that CLAHE based global thresholding techniques based on Otsu and Isodata thresholds detected the large vessels but failed to detect the thin vessels due to the fact that the thin vessels have very low contrast and are difficult to be distinguished from the background tissues using these histogram based thresholding techniques. Two new multi-scale approaches of computing global threshold based on the different texture information such as inverse difference moment and sum-entropy combined with phase congruence pre-processing that could help achieve an improved detection of large and

some thin vessels were implemented to extend the technique proposed by Amin and Hong [48] for the detection of retinal blood vessels. When compared with [48], the two multi-scale approaches presented higher average accuracy rates. Another comparative study on the use of fuzzy c-means combined with phase congruence and GLCM sum entropy combined with phase congruence for vessel segmentation was achieved in this thesis. The investigation demonstrated the higher average accuracy rate but a longer running time fuzzy c-means combined with phase congruence when compared with the multi-scale based sum entropy thresholding combined with phase congruence. The longer running time of the fuzzy c-means over the multi-scale based sum entropy thresholding is attributed to the iterative nature of fuzzy c-means. When compared with the literature, both methods achieved considerable faster running time.

Another contribution of this thesis is the proposition of two novel local adaptive thresholding techniques based on two different Haralick texture features, namely local homogeneity and energy, for the segmentation of large and thin retinal vessels. Although these two texture features have been applied for supervised image segmentation in the literature, their novelty in this thesis lies in that they are applied using an unsupervised image segmentation approach. Each of these local adaptive thresholding techniques locally applies a multi-scale approach on the different texture information considering the pixel of interest in relationship with its spacial neighbourhood to compute the local adaptive threshold. The localised multi-scale approach of computing the thresholds handle the challenge of the vessel width variation. The visual results showed that the two novel local adaptive thresholding techniques achieved higher reduction of false vessels around the border of the optic disc when compared with the state of the art. The average accuracy, average sensitivity rates and the AUC values of these local adaptive thresholding techniques also show significant improvements when compared with the unsupervised and supervised vessel segmentation methods in the literature. When compared with the literature [22], [23], [28], [32], [33], [38], [43], [34], [39], [42], [47], [48], [82], [87], [84], [88], [83], the local adaptive thresholding techniques achieve highly improved computational time of 1.9 to 3.9 seconds to segment vessels in each retinal image.

This thesis also contributes to knowledge by investigating various difference images combined with k-means clustering technique for the segmentation of large and thin vessels in retinal images. Different low pass filters such as median filter, mean filter and Gaussian filter are applied each to smoothen and compute various difference images. When investigating the difference images combined with the k-means clustering technique, this research established that good vessel segmentation requires a difference

image that preserves the vessel details of the retinal image. Investigating the different low pass filters, the median filter yields the best difference image required by the k-means clustering for the segmentation of retinal vessels. Further investigations show that the linear combination of the median filter based difference images with Gaussian and mean filter based difference images respectively when combined with k-means clustering technique leads to the detection of more thinner vessels. The false detection around the border of the optic disc are however higher on the segmented vessel obtained by using the hybrid difference images combined with the k-means clustering but lesser on the segmented vessel obtained when using k-means combined with median filter based difference images. The median filter based difference images combined with k-means clustering technique achieved significantly improved average accuracy rates, average sensitivity rates and the AUC values when compared with the state of the art. Median filter based difference images combined with k-means clustering technique (that is DIMDF) also achieved a higher reduction of false vessels around the border of the optic disc when compared with some very good previous techniques in the literature. When compared with the literature [22], [23], [28], [32], [33], [38], [43], [34], [39], [42], [47], [48], [82], [87], [84], [88], [83], the median filter based difference images combined with the k-means clustering technique achieved a highly improved computational time of 3.4 to 4 seconds to segment vessels in each retinal image.

Furthermore, this thesis contributes to knowledge by utilising stationary points on the vessels to detect vessel twists. The detection of the stationary point does not only help in checking the change of direction and twists in the vessels but also helps in detecting the straightness and non-straightness of the vessels. A new model that combines distance metric and vessel twist frequency based on stationary points for the computation of normalised and non-normalised tortuosity index (TI) measure was investigated. This thesis demonstrated that the non-normalised TI measure has significantly improved performance when compared with distance metric and normalised TI measures.

1.6 Scope of Research and Limitation

This research scope is to provide contributions toward the segmentation of vessels in retinal images using relevant retinal vessel segmentation datasets with their ground truths from publicly available online repositories. Contributions are also provided toward the characterisation of detected vessels through the investigated tortuosity measures and the performances evaluated using the expert's ground truth. The subjective

decisions of the observers in the preparation of the ground truths of the datasets are assumed ignorable throughout this thesis. This is based on the fact that no one knows the reasons for the subjectivity of the human observations during the preparation of the ground truth of the datasets considered in this thesis.

1.7 Thesis Outline

Chapter 2 reviews the state-of-the-art of retinal vessel segmentation and characterisation using tortuosity measure. In Chapter 3, the materials and methods such as global thresholding techniques, local adaptive thresholding techniques, clustering-based techniques and tortuosity measurement investigated in this research are presented. Different image pre-processing algorithms are also presented. Chapter 4 presents the experimental results and discussion. The performances of the various methods investigated in this research are also compared with the state of the art. Chapter 5 draws the conclusions and presents the recommendations for future work.

Chapter 2

LITERATURE REVIEW

2.1 Medical Imaging

Medical imaging has become a significant field of research due to the advances in the hardware and software resources used for the acquisition, processing and storage of the images [2], [3], [4], [5], [89]. With the help of several imaging modalities such as magnetic resonance imaging (MRI), digital mammography, computed tomography (CT), and some other imaging techniques, physicians are better informed with detailed knowledge of healthy or diseased anatomy for efficient diagnosis, patient monitoring and treatment as well as clinical studies [90].

2.1.1 Retinal Fundus Imaging

Retinal fundus imaging in ophthalmology has been of great use in medical diagnosis and progression monitoring of various retinopathies such as diabetic retinopathy (DR), retinopathy of prematurity (ROP) as well as hypertensive and cardiovascular diseases [13], [91]. Several digital imaging modalities such as optical coherence tomography (OCT) [92], [93], [94], fluorescein angiography [95], indocyanine green angiography [96], [97], [98], fundus autofluorescence, multifocal electroretinography [99] and coloured fundus photography [13] are used in ophthalmology. OCT has also been described as a useful retinal imaging tool for the diagnosis and the monitoring of patients responses to therapy [100], [101]. In fluorescein angiography [95], [102] and indocyanine green angiography [96], [97], [98], fluorescein dye is administered. After the circulation of the fluorescein dye across the body and the retinal blood vessels, a light beam with a suitable wavelength is used to excite free fluorescein molecules [95], [102]. There is, however, a higher transmission of wavelength in indocyanine green angiography when

compared to the wavelength used in fluorescein angiography. Though similar to fluorescein angiography, fundus autofluorescence [103], [104],[105] does not use fluorescein dye. Multifocal electroretinography measures the local electroretinogram from different parts of the posterior retinal by utilising the electrical receptions obtained through a corneal electrode [106]. Modifications in the retinal functions both before and after retinal detachment surgery are assessed with the aid of multifocal electroretinography [107]. Coloured fundus photography however remains an important retinal imaging modality due to its safety and cost-effective mode of retinal abnormalities documentation [13].

2.1.2 Anatomic Structures in Retinal Images

There are several important anatomic structures in the human retina (See Figure 2.1(a)). The robust detection of the different anatomic structures of the retina is necessary for a reliable characterisation of healthy or diseased retina. Several automated techniques have successfully been used to detect different anatomic features as well as retinopathy features in retinal images [29], [30], [108], [109], [110] (See Figure 2.1(b) & 2.1(c)).

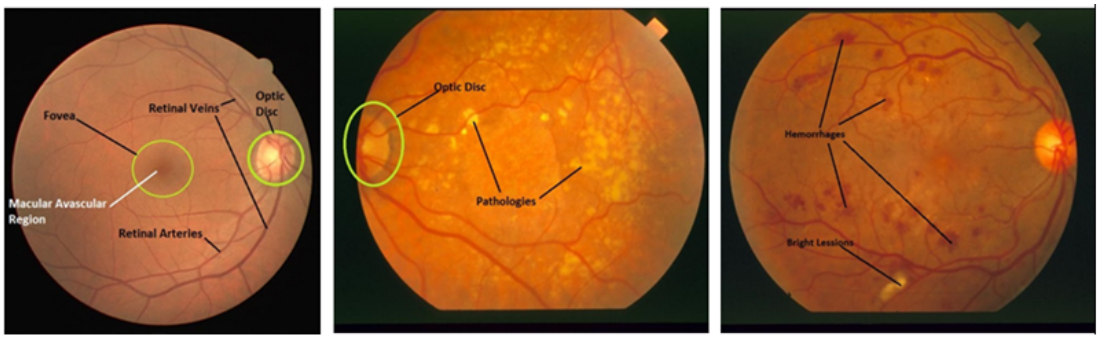

Figure 2.1: Retinal Image Anatomic Structures

The localisation of optic disk was implemented using different techniques; different features of the optic disk such as intensity, morphology and colour [30], [111], [112], Hough transform [113], [114], [115], Principal Component Analysis (PCA)[30, 116], convergence of blood vessels [117], [118] and colour space transformation combined with mathematical morphological techniques [119].

The segmentation of the vessel network is of great use in ophthalmology as it helps ophthalmologists to focus on retinal vessel morphological features which are often early

indicators of some retinopathies [120] and are of prognostic importance in ROP [121].

In related development, several works have implemented the automatic detection of various pathologies in retinal images using different segmentation techniques. Spencer et al. [122] implemented a morphological transformation for microaneurysms segmentation. Several other works such as [123], [124], [125], [126], [127] implemented microaneurysms segmentation using different automated approaches. Various investigations have been performed on the automated detection of exudates and cotton wool spot in retinal images in [124], [126], [128], [129]. However, there is still room for further improvement in the separation of hard exudates from other bright lesion-like appearing structures as well as the detection of tiny exudates [130].

2.2 Retinal Vessel Segmentation

Retinal vessel network composed of veins and arteries are elongated features visible in the retinal image. Retinal vessel segmentation is a task in which these vessels are delineated from retinal images using specific visual criteria. Efficient vessel network detection and vessel feature analysis are of great importance for the diagnosis and progress monitoring of the various retinopathies and vascular diseases. Manual detection and analysis of the retinal vessels have been very tedious and time consuming tasks that require trained and skilled personnel who are often scarce [78], [79]. Automatic vessel segmentation is of great use in ophthalmology in achieving timely and accurate diagnosis of retinopathies [19].

Several retinal vessel segmentation techniques have been proposed in the literature and the segmentation techniques can be divided into two major approaches namely unsupervised and supervised methods. Two major publicly available databases (DRIVE [131] and STARE [132]) are often used to evaluate the effectiveness and robustness of the previously proposed vessel segmentation methods. The performance of the segmentation results obtained in most of these previously proposed retinal vessel segmentation methods is qualitatively and quantitatively analysed using sensitivity, specificity and accuracy metrics. Sensitivity measure indicates the ability of a segmentation technique to detect vessels in the retinal images while specificity measure indicates the ability of a segmentation technique to detect the background in retinal images. The accuracy measure indicates the degree of conformity of the segmented retinal image to an expert's ground truth. In order to ascertain a good segmentation performance, the sensitivity, specificity and accuracy measures of a segmentation method must be high [69]. The area under the curve (AUC) is another performance measure used for retinal

segmentation results. AUC is extracted from a receiver operating characteristic (ROC) curve. ROC curve is a plot of rightly classified pixels versus the fraction of wrongly classified pixels as vessels.

2.2.1 Supervised Vessel Segmentation Methods

In supervised vessel segmentation methods, different algorithms are used for learning the set of rules required for the retinal vessel extraction. A set of manually segmented retinal vessels by trained and skilled personnels is considered as the reference image. These reference images are used for the training phase of the supervised segmentation techniques. The availability of reliable labelled training samples by experts for the supervised segmentation methods is sometimes expensive or unavailable [16].

Ricci and Perfetti [20] proposed automated vessel segmentation based on line operators. Two segmentation methods were considered. One of the segmentation methods used two orthogonal line detectors with the grey level of the target pixel to construct a feature vector for supervised classification. The training set was formed by pixel samples from the 20 labeled training images on the DRIVE database while a training set for STARE comprises of samples randomly extracted from test images on STARE. A supervised classification of the pixels as either vessels or background is implemented using support vector machine. An average accuracy rate of 0.9595 and an AUC value of 0.9633 were achieved on DRIVE database while the average accuracy rate of 0.9646 and an AUC value of 0.9680 were achieved on STARE database. Although this method presents the highest average accuracy rate while compared to all other supervised vessel segmentation methods (see Table 2.1) and unsupervised vessel segmentation methods (see Table 2.2), the average sensitivity rate of this method was not presented. The high false detections around the border of the optic disc is a major drawback of this technique. The need for a new set of training samples and the retraining of classifier before applying it on a new dataset also remains the drawback of this method.

Staal et al. [22] utilised ridge information and k-nearest neighbour classifier with sequential forward feature selection for retinal vessel segmentation. The accuracy rate and the AUC rate of this method achieved on both databases are only available in the paper. However, the detailed performance of this method on each image of DRIVE dataset and the average performance rates are available on DRIVE website [131] while the average sensitivity rate achieved by this method on STARE database is obtained from Mendonca et al. [84]. An average sensitivity rate of 0.7345, average accuracy rate of 0.9442 and an AUC value of 0.9520 were achieved on DRIVE database and an

average sensitivity rate of 0.6970, average accuracy rate of 0.9516 and an AUC value of 0.9614 were achieved on STARE database. They, however, used only 19 of the 20 images in the STARE database. One of the drawbacks of this technique is its inability to segment thinner vessels. Another drawback is that this method required an average time of about 900 seconds (15 minutes) to segment each image. Furthermore, this method is expensive as it requires a time consuming manual labelling (about 2 hours per image) and a retraining of the classifier before applying it on a new dataset.

Soares et al. [23] implemented the combination of two-dimensional (2-D) Gabor wavelet transform and Bayesian classifier for retinal vessel segmentation. A feature vector comprising a multi-scale 2-D Gabor wavelet transform responses and pixel intensity was generated from the retinal images for training the classifier. The training set was formed by pixel samples from the 20 labeled training images on the DRIVE database while leave-one-out tests were performed (that is every image is segmented using samples from the other 19 images) for the training set of the vessel segmentation method on STARE database. Each of the pixels in the retinal image was further classified as vessel or background tissue using a Bayesian classifier. An average accuracy rate of 0.9466 and an AUC value of 0.9614 were achieved on DRIVE database while an average accuracy rate of 0.9480 and an AUC value of 0.9671 were achieved on STARE database. Although the technique had a good performance, segmentation of thinner vessels as well as false detections around the border of the optic disc remain a challenge. Another drawback of this method is that it required 9 hours for the training phase and an average time of about 190 seconds (3 minutes, 10 seconds) to segment vessels in each retinal image. The need for a retraining of classifier before applying it on a new dataset remains the limitation of this method.

Fraz et al. [24, 25] implemented a supervised segmentation technique based on an ensemble classifier of bootstrapped decision trees for the segmentation retinal vessel network. This ensemble classifier was constructed by using 200 weak learners and trained on 200000 training samples from DRIVE training set and 75000 training samples from STARE. An average sensitivity rate of 0.7406, average accuracy rate of 0.9480 and an AUC value of 0.9747 were achieved on DRIVE database while average sensitivity rate of 0.7548, average accuracy rate of 0.9534 and an AUC value of 0.9768 were achieved on STARE database. The required time to train the classifier for the DRIVE database is 100 seconds and the ensemble for STARE takes 49 seconds. The time required to process a retinal image is about 100 seconds. The limitation of this method is that the higher the training samples, the higher the time required. Another drawback of this method is its need for a new set of training samples and the retraining of classifier

before applying it on a new dataset. There is also a need to improve the computational time and the ability to detect the thinner vessels.

Marin et al. [28] generated a 7-D vector composed of grey-level and moment invariants-based features for pixel representation, and a multilayer feed forward artificial neural network (ANN) classifier was used for the vessel segmentation. The classifier used in this method was trained only on DRIVE images to segment vessels on both DRIVE and STARE databases. An average sensitivity rate of 0.7067, average accuracy rate of 0.9452 and an AUC value of 0.9588 were achieved on DRIVE database and an average sensitivity rate of 0.6944, average accuracy rate of 0.9526 and an AUC value of 0.9769 were achieved on STARE database. This technique required an average time of about 90 seconds to segment each retinal image. Although good accuracy rates were obtained, the drawback of this technique is its inability to detect thinner vessels. There is also a need for the improvement of the computational time.

Lupascu et al. [32] implemented a supervised segmentation technique for detecting vessels using Ada-Boost classifier. A feature vector comprising of local and spatial properties of the vessels were generated from the responses of various filters (matched filters, Gabor wavelet transform, Gaussian filter and its derivatives). Ada-Boost classier was further trained and used to classify each pixel as either vessel or non-vessel. An average sensitivity rate of 0.6728, average accuracy rate of 0.9597 and an AUC value of 0.9561 were achieved on DRIVE database. This method required 4 hours for the training phase and an average time of about 125 seconds (2 minutes, 4 seconds) to segment each image on DRIVE test database. The drawback of this method is the high computational time required to segment vessels in each retinal image. Another drawback of this method is its inability to detect the thin vessels.

Niemeijer et al. [35] implemented vessel segmentation method based on pixel classification. Each pixel of the green plane of the retinal image and responses of Gaussian matched filter were used to construct feature vectors. Subsequently, these feature vectors were used for the training and classification of pixels as vessels or background using a kNN-classifier. An average sensitivity rate of 0.7145, average accuracy rate of 0.9416 and an AUC value of 0.9294 were achieved on DRIVE database. The major drawback of this technique is its inability to detect thin vessels.

You et al. [133] combined radial projection with SVM using a semi-supervised self-training approach for the segmentation of vessels. Radial projections were used to locate the vessel centre-lines and the low contrast blood vessels. Having enhanced the vessels using modified steerable wavelet, a feature vector was generated using line strength measures. SVM classifier was used further in a semi-supervised self training

Table 2.1: Performance of Supervised Methods on DRIVE & STARE Databases

Methods	Average Accuracy		Average Sensitivity		AUC		Average Time
	DRIVE	STARE	DRIVE	STARE	DRIVE	STARE	Seconds
Human observer [131],[132]	0.9473	0.9354	0.7761	0.8949	N/A	N/A	7200
Ricci and Perfetti [20]	0.9595	0.9584	N/A	N/A	0.9558	0.9602	N/A
Staal et al.[22]	0.9442	0.9516	0.7345	0.6970	0.9520	0.9614	900
Soares et al.[23]	0.9466	0.9480	N/A	N/A	0.9614	0.9671	190
Fraz et al. [24, 25]	0.9480	0.9534	0.7406	0.7548	0.9747	0.9768	49 &100
Marin et al. [28]	0.9452	0.9526	N/A	N/A	0.9588	0.9769	90
Lupascu et al. [32]	0.9597	N/A	0.6728	N/A	0.9561	N/A	125
Niemeijer et al. [35]	0.9377	N/A	0.7145	N/A	0.9294	N/A	N/A
You et al. [133]	0.9434	0.9497	0.7410	0.7260	N/A	N/A	N/A

manner for the classification of each pixel as either vessel or non-vessel. An average sensitivity rate of 0.7410 and an average accuracy rate of 0.9434 were achieved on DRIVE database while an average sensitivity rate of 0.7260 and an average accuracy rate of 0.9497 were achieved on STARE database. A major drawback of this method is the over-estimation of narrow vessels due to vessel-like noise.

2.2.2 Unsupervised Vessel Segmentation Methods

The approaches based on unsupervised classification attempt to discover inherent patterns of blood vessels in retinal images that can be used further to determine that a particular pixel belongs to vessel or not. The training data or hand labelled ground truths do not contribute to the design of the algorithms of this approach.

2.2.2.1 Matched filtering-Based Techniques

Earliest automatic techniques used for the detection of retinal vessels utilise matched filter response (MFR). A 2-D kernel is designed for properties such as vessel curvature, vessel diameter and pixel intensity in the retinal image combined with MFR and additional image processing techniques were used for retinal vessel network segmentation.

Chaudhuri et al. [26] implemented MFR by initially approximating the intensity of grey-level profiles of the cross-sections of retinal vessels using a Gaussian shaped curve. An Otsu global thresholding technique was further applied to the matched filter response image to segment the retinal vessels. The results achieved by [26] are obtained from [35] and DRIVE database website [131]. This technique however achieved a poor detection of the vessels with the low average sensitivity rate of 0.3357, an average accuracy rate of 0.8773 and an AUC value of 0.7878 were achieved on DRIVE database. This technique presents the lowest performance while compared to all other

unsupervised vessel segmentation methods (see Table 2.2).

Hoover et al. [21] identified that a single global threshold does not provide adequate classification. Hoover et al. [21] further segmented retinal vessels by applying a threshold probing technique combining local vessel attributes with region-based attributes on MFR image. While compared to [26] where a basic global thresholding of an MFR image was implemented, the method proposed in [21] reduced the false positive rate by as much as 15 times. Although the performance of this method was not available in the paper, the average accuracy rate and the AUC rate achieved by this technique was presented by Staal et al. [22]. The average sensitivity rate and the average accuracy rate of this method on STARE database are obtained from Mendonca et al. [84]. An average sensitivity rate of 0.6751, an average accuracy rate of 0.9275 and an AUC value of 0.7590 were achieved on STARE database. The single scale matched filter applied by Chaudhuri et al. [26] and Hoover et al. [21] however failed to produce strong responses to all the vessels in the retinal image as there are large variations in the widths of the vessels.

Chanwimaluang and Fan [27] proposed the combination of matched filter and entropy for the segmentation of retinal vessels. The performance measure of the proposed technique was only visual. Zhang et al. [33], having identified that the general matched filter (MF) responds to both vessels edges and the non-vessel edges, extended the general matched filter with the first-order derivative of the Gaussian (FDOG) properties of the retinal vessels. The MF-FDOG implemented in [33] is composed of the original MF, which is a zero-mean Gaussian function, and the first-order derivative of Gaussian(FDOG). An average accuracy rate of 0.9382 and an average accuracy rate of 0.9475 were achieved on DRIVE and STARE databases respectively. This method however failed to segment the thinner vessels. This method required an average time of 10 seconds to segment vessels in each retinal image.

Wang et al. [43] proposed multi-wavelet kernels and multi-scale hierarchical decomposition for the detection of retinal vessels. Vessels were enhanced using matched filtering with multi-wavelet kernels. The enhanced image was normalised using multi-scale hierarchical decomposition. A local adaptive thresholding technique based on the vessel edge information was used to generate the segmented vessels. An average accuracy rate of 0.9461 and an AUC value of 0.9543 were achieved on DRIVE database while the average accuracy rate of 0.9521 and an AUC value of 0.9682 were achieved on STARE database. Although good accuracy rates were obtained, this method fails to detect thin vessels. Another drawback of this method is its average computational time of 210 seconds (3.5 minutes) to segment vessels in each retinal image.

Cinsdikici and Aydin [82] implemented the combination of matched filter and an ANT colony algorithm for the detection of retinal vessels. An average accuracy rate of 0.9293 and an AUC value of 0.9407 were achieved on DRIVE database. This method required an average time of 35 seconds to segment vessels in each retinal image. The drawbacks of this method are its inability to detect thinner vessels and over-estimation of detected vessels.

Chakraborti et al [39] implemented an unsupervised segmentation technique that combines vesselness filter and matched filter using orientation histogram for the segmentation of retinal vessels. An average sensitivity rate of 0.7205 and an average accuracy rate of 0.9370 were achieved on DRIVE database while an average sensitivity rate of 0.6786 and an average accuracy rate of 0.9379 were achieved on STARE database. Although this method achieves a fast computational time of 8 seconds to segment vessels in each retinal image, it fails to segment the thin vessels.

2.2.2.2 Multi-Scale-Based Techniques

In order to handle the limitation of single scale matched filter weak responses due to large variation in the widths of the vessels, multi-scale filters were introduced for segmentation of vessel networks.

Vlachos and Dermatas [41] proposed a multi-scale retinal vessel segmentation method. The algorithm is based on multi-scale line-tracking procedure and morphological post-processing. An average sensitivity rate of 0.7468 and an average accuracy rate of 0.9285 were achieved on DRIVE database. The drawback of this method is its inability to detect the thin vessels.

Li et al. [47] implemented the multi-scale production of the matched filter (MPMF) responses as the multi-scale data fusion strategy. The proposed MPMF vessel extraction scheme applied multi-scale matched filtering, scale multiplication in the image enhancement step and double thresholding in the vessel classification step. Incorporating the multi-scale information assist to concurrently detect the vessels with variant widths. Vessel segmentation results generated by using MPMF without any post-processing on DRIVE achieved an average sensitivity rate of 0.7154 and an average accuracy rate of 0.9343 on DRIVE database. Vessel segmentation results generated by using MPMF combined with a post-processing phase achieved an average sensitivity rate of 0.7191 and the average accuracy rate of 0.9407 were achieved on STARE database. This method required 8 seconds to detect vessels without post-processing and required 30 seconds to detect vessels while combined with a post-processing phase. Although this

method achieved a faster computational time without post-processing, the accuracy rate is relatively low. It is also noted that this method spent most of the time on the post-processing phase. The three scales applied by this method failed to accurately segment the thin vessels. Hence, there is a need for further improvement.

Yedidya and Hartley [134] implemented a method based on Kalman filter for the tracking of vessels. They applied a set of matched filters of different widths and orientations to detect seed points. Vessels were tracked using the gradient information from both edges of the blood vessel on the detected seed points. The ROC curve presented by Staal et al. [22] was slightly higher while compared to the method proposed by these authors. The drawback of this method is its inability to detect the thin vessels due to poor gradient information. The time (20 to 40 seconds) required by this method to segment the vessel network in a retinal image also needs further improvement.

Martinez-Perez et al. [135] used a combination of scale space analysis and region growing to segment the vessel network. The performance of this method obtained from Niemeijer et al. [35] and DRIVE database website [131] showed that an average sensitivity rate of 0.6389 and average accuracy rate of 0.9181 were achieved on DRIVE database. The major drawbacks of this method are its inability to segment thin vessels and a lot of false detection of vessels around the border of the optic disc.

Yin et al. [87] implemented a probabilistic tracking-based method for vessel segmentation. A Bayesian method with maximum a posteriori (MAP) was used for detecting the retinal vessel edge points. The proposed segmentation method in [87] achieved an average sensitivity rate of 0.6522 and an average accuracy rate of 0.9267 on DRIVE database while an average sensitivity rate of 0.7248 and an average accuracy rate of 0.9412 were achieved on STARE database. One of the drawbacks of this method is its inability to detect thin vessels. Another drawback is that this method required a very high average time of about 378 seconds (6.3 minutes) to segment vessels in each retinal image.

2.2.2.3 Morphological Processing-Based Techniques

Zana and Klein [40] implemented a vessel segmentation method based on the use of mathematical morphology and cross-curvature evaluation. Having established the fact that vessels are piecewise linear and connected, this method enhances and differentiates the vessels from the background using mathematical morphological operators with linear structuring elements. The performance of [40] on DRIVE database is available in [35], [131]. An average sensitivity rate of 0.6971, average accuracy rate of 0.9377

and an AUC value of 0.8984 were achieved on DRIVE database. The drawback of this technique is its inability to segment the thinner vessels.

Fraz et al. [34, 44, 45] combined vessel centre-lines detection and morphological bit plane slicing for the detection of vessel network in retinal images. A first-order derivative of a Gaussian filter was used to extract vessel centre-lines. The orientation and shape of the vessels were further determined using multidirectional morphological top-hat operator with linear structural elements followed by bit plane slicing. Different colour representations such as the green component of the original RGB image, the Intensity channel of the HSI colour space, the luminosity channel of NTSC (YIQ) colour space and the L* component of the L*A*B* representation were analysed in [45]. Vessel centre-lines were extracted using the different colour channel but the vessel shape and orientation maps were generated from the green channel of RGB using the morphological bit plane slicing. The final segmented image was obtained by the reconstruction of these two images. Fraz et al. [45] achieved an average sensitivity rate of 0.7152 and an average accuracy rate of 0.9430 on DRIVE database while an average sensitivity rate of 0.7311 and an average accuracy rate of 0.9442 were achieved on STARE database. Fraz et al. [34] also detected vessel centre-lines by applying difference of offset Gaussian filter in four directions to the background of normalised retinal image. This was followed by the evaluation of average derivative values of the filter response images using the method proposed by Mendonca and Campilho [84]. Fraz et al. [34] achieved an average sensitivity rate of 0.7302 and an average accuracy rate of 0.9422 on DRIVE database while an average sensitivity rate of 0.7318 and an average accuracy rate of 0.9423 were achieved on STARE database. Fraz et al. [34] required an average 37.4 seconds and 39.5 seconds for the vessel segmentation of each retinal image on DRIVE and STARE databases respectively. Although these techniques made good progress, there is need for further improved processing time and the detection of more thin vessels.

Mendonca and Campilho [84] combined differential filters for centre-line extraction with morphological operators for filling vessel segments while considering intensity and morphological properties. A multi-scale top-hat transform using circular structuring elements of different radius was applied to detect vessels of different widths in the retinal images. An average sensitivity rate of 0.7315 and an average accuracy rate of 0.9463 were achieved on DRIVE database while an average sensitivity rate of 0.7123 and an average accuracy rate of 0.9479 were achieved on STARE database. This method required about 150 seconds to segment vessels in each retinal image. Although this method made great progress, there is still need for improvement on the segmentation

of thinner vessels and the computational time.

Miri and Mahloojifar [88] found ridges by applying multi-structure elements to enhanced retinal image. Morphological operators by reconstruction was further applied to get rid of the ridges outside the vessel tree. An average sensitivity rate of 0.7352 and an average accuracy rate of 0.9458 were achieved on the DRIVE database. This method also required about 50 seconds to segment vessels in each retinal image. This technique achieved a good performance, but some thin vessels were not detected. There is also a further need to improve its processing time.

Jiménez et al. [136] implemented vessel centre-lines detection and a combination of morphological operations for retinal vessel segmentation. Vessel centre-lines were extracted by applying difference of offset Gaussian filter in four directions to the background of normalised retinal image. Morphological enhancement using modified top-hat transform with variable size structural elements and binary morphological reconstruction are further applied to the vessel. A region growth process is subsequently applied to centre-lines for the vessel filling phase. An average sensitivity rate of 0.6960 and average accuracy rate of 0.9430 were achieved on DRIVE database. This technique failed to detect the thin vessels.

2.2.2.4 Adaptive Thresholding-Based Techniques

Jiang and Mojon [38] implemented an adaptive local thresholding based on a verification-based multi-threshold probing scheme for the detection of vessel network. Vessels' properties such as contrast, curvilinear angle, width, and size were modelled into the verification phase, and a number of thresholds were used to probe and detect vessel network. The combination of the resulting detected vessel networks obtained from probed thresholds followed by post processing phase generated the final segmented vessel network. An average sensitivity rate of 0.6399, average accuracy rate of 0.9212 and an AUC value of 0.9114 were achieved on DRIVE database while the average accuracy rate of 0.9009 and an AUC value of 0.929 were achieved on STARE database. This technique required an average time of about 8-10 seconds to segment each image. The drawback of this technique is its inability to detect the thin vessels and the limitation of unconnected vessel network.

Akram and Khan [46] enhanced the vascular pattern using 2-D Gabor wavelet and followed by a multilayered thresholding technique that applied different threshold values iteratively to generate grey level segmented image. An average accuracy rate of 0.9469 and an AUC value of 0.9632 were achieved on DRIVE database while an average

accuracy rate of 0.9502 and an AUC value of 0.9706 were achieved on STARE database. Although this technique made good progress in the detection of vessels, there is a need for further improvement on detection of thinner vessels.

Qin et al. [137] combined multi-scale analysis based on Gabor filters, scale multiplication and region based thresholding to achieve adaptive thresholding for vessel segmentation. The drawback of this technique is its inability to detect the thin vessels.

2.2.2.5 Model-Based Techniques

Szpak and Tapamo [138] combined the gradient based approach and level set technique to segment vessels in retinal images. An average accuracy rate of 0.9299 was achieved on DRIVE database. This method was however unable to detect the thin vessels.

Zhao et al. [139] implemented a segmentation method based on level set and region growing for the detection of retinal vessels. The contrast limited adaptive histogram equalisation and 2-D Gabor wavelets were applied in the pre-processing phase to enhance the vessels. An anisotropic diffusion filter was further applied to smooth the image and preserve the boundaries of vessels. Two methods namely, region growing method and a region-based active contour model with level set were further applied to extract the retinal vessels. The segmentation results obtained from the methods were combined to obtain the final segmented vessel network. An average sensitivity rate of 0.7354 and an average accuracy rate of 0.9477 were achieved on DRIVE database while an average sensitivity rate of 0.7187 and an average accuracy rate of 0.9509 were achieved on STARE database. This method required an average time of less than 120 seconds to segment each image.

Salazar-Gonzalez et al. [140] proposed a vessel segmentation method based on graph cut technique. The blood vessels were enhanced using a contrast enhancement process on the green channel of the coloured retinal image using an adaptive histogram equalisation. The final vessel segmentation was obtained using a graph constructed based on the prior information and the spatial pixel connections. An average sensitivity rate of 0.6782 and an average accuracy rate of 0.9478 were achieved on DRIVE database while an average sensitivity rate of 0.7197 and an average accuracy rate of 0.9479 were achieved on STARE database. This method was unable to detect the thinner vessels.

Cai and Chun [141] applied an unsupervised segmentation approach based on normalised cut technique to segment blood vessels in retinal images. A candidate window which may contain blood vessels was selected using gradient matrix while normalised cut is applied to detect the vessels on the selected window. A tracking

strategy is applied in the post-processing phase to remove noise. The ROC curve presented by this method is slightly lower while compared to the method proposed by Staal et al. [22] and Soares et al. [23]. The segmentation performance and the time (30 seconds) required by this method to segment the vessel network in a retinal image also needs further improvement.

Xiao et al. [83] proposed a Bayesian method with spatial constraint for the segmentation of retinal vessels. The spatial dependence of the posterior probability of each pixel in relation to their neighboring pixels was utilised. An energy function was further defined. Furthermore, the vessel network were detected by applying the modified level set approach to minimise the energy function. An average sensitivity rate of 0.7513 and an average accuracy rate of 0.9529 were achieved on DRIVE database while an average sensitivity rate of 0.7147 and an average accuracy rate of 0.947 were achieved on STARE. The execution time of this technique to segment each image is about 81 seconds as each iteration required less than 10 seconds and the convergence of the algorithm may be achieved in less than 10 iterations.

2.2.2.6 Phase Congruence-Based Techniques

Kovesi [142] proposed a combination of different log-Gabor filters using Fourier phase information to measure phase congruency. The proposed phase congruence model in [142] that uses the Fourier phase information has been very promising in the detection of object boundary in the presence of noise due to illumination and contrast variation.

Amin and Yan [48] implemented the detection of retinal blood vessels using phase congruency at an high speed. The threshold values used were, however, not dynamically computed but ranged from 0.32 to 0.37. An average sensitivity rate of 0.6608 and an average accuracy rate of 0.9191 were achieved on DRIVE database while an average sensitivity rate of 0.7261 and an average accuracy rate of 0.9081 were achieved on STARE database. This method required 10 seconds to segment vessels in each retinal image. Although the technique performed well in terms of speed, there is a need for improved accuracy rates and a dynamically computed thresholding approach that addresses the detection of the thin vessels. Vessels cross-sectional profiles in the Fourier domain were represented and characterised using phase congruence by Zhu [143]. A bank of Gabor filter was used to transform the input image. The performance of the proposed technique in [143] was only done by the visual assessment of results.

Tagore et al. [144] applied phase congruency to improve the contrast of vessel segments against the retinal background. A hierarchical clustering based histogram

thresholding was then used to segment the contrast enhanced vessels. An average accuracy rate of 0.9424 and an AUC value of 0.9531 were achieved on DRIVE database while an average accuracy rate of 0.9497 and an AUC value of 0.9611 were achieved on STARE database. This method is limited in its ability to detect thin vessels.

Dai et al [145] implemented a multi-scale line filter combined with phase congruency for retinal vasculature segmentation. The multi-scale line filter was used to reduce the influence of step edges while phase congruency was used for the post processing to detect low contrast vessels. An average sensitivity rate of 0.6542 and an average accuracy rate of 0.9347 were achieved on DRIVE database while an average sensitivity rate of 0.6503 and an average accuracy rate of 0.9392 were achieved on STARE database. The drawback of this method is its inability to accurately detect vessel widths. This method also failed to detect some thin vessels.

2.2.2.7 Clustering-Based Techniques

Saffarzadeh et al. [42] implemented a pre-processing phase based on k-means followed by the use of multi-scale line operators for the detection of retinal vessel network. With the help of k-means, the visibility of the vessels was enhanced and the impact of bright lesions reduced. The retinal vessels were finally detected using the line detection operator in three scales. An average accuracy rate of 0.9387 and an AUC value of 0.9303 were achieved on DRIVE database while an average accuracy rate of 0.9483 and an AUC value of 0.9431 were achieved on STARE database. This technique required an average time of about 7.6 seconds to segment each retinal image. The drawback of this method is the presence of false vessel detection across the retinal images and the border of the optic disc. This method also failed to detect the thinner vessels.

Tolias and Panas [146] implemented a fuzzy c-means algorithm to segment vessels in retinal angiogram images starting from the optic disc. This method is a tracking-based approach that applies local information to detect vessels between two points using 1-D vessel profile. The major drawback of this method is the incompletion in the detection of vessels due to termination at branch points. This method also failed to segment thinner vessels due to their low contrast against background. Kande et al. [147] combined matched filtering and a spatially weighted fuzzy c-means for vessel segmentation in retinal images. Intensity information from red and green channels of the same retinal image were used to correct uneven illumination in coloured retinal images. The matched filter was used further to enhance the contrast of the blood vessels and a spatially weighted fuzzy c-means was used to segment the retinal vascular

tree. An average accuracy rate of 0.8911 and an AUC value of 0.9518 were achieved on DRIVE database while an average accuracy rate of 0.8976 and an AUC value of 0.9298 were achieved on STARE database. The major drawback of this method is the high detection of false vessels around the border of the optic disc.

An hybrid approach comprising of a fuzzy clustering and mathematical morphology was proposed by Yang et al. [148]. A morphological top-hat operation was used for retinal image smoothing and background information removal. The vessels were then extracted through fuzzy clustering. The algorithm was only tested through visual comparisons. While compared to Otsu thresholding, their method presented a better result. Sun et al. [149] implemented morphological multi-scale enhancement in combination with fuzzy filter and watershed transformation for vascular segmentation. The proposed technique in [149], however, did not use any full retinal image in its experiment.

Table 2.2: Performance of Unsupervised Methods on DRIVE & STARE Databases

Methods	**Average Accuracy**		**Average Sensitivity**		**AUC**		**Average Time**
	DRIVE	**STARE**	**DRIVE**	**STARE**	**DRIVE**	**STARE**	Seconds
Human observer [131], [132]	0.9473	0.9354	0.7761	0.8949	N/A	N/A	7200
Hoover et al. [21]	N/A	0.9275	N/A	0.6751	N/A	0.7590	N/A
Chaudhuri [26]	0.8773	N/A	0.3357	N/A	0.7878	N/A	N/A
Zhang et al. [33]	0.9382	0.9475	N/A	N/A	N/A	N/A	10
Jiang and Mojon [38]	0.9212	N/A	0.6399	0.9009	0.8984	0.929	10
Wang et al. [43]	0.9461	0.9521	N/A	N/A	0.9543	0.9682	210
Fraz et al. [34]	0.9422	0.9423	0.7302	0.7318	N/A	N/A	37.4
Chakraborti et al [39]	0.9370	0.9379	0.7205	0.6786	N/A	N/A	8
Zana and Klein [40]	0.9416	N/A	0.6971	N/A	0.8984	N/A	N/A
Fraz et al. [45]	0.9430	0.9442	0.7152	0.7311	N/A	N/A	N/A
Akram and Khan [46]	0.9469	0.9502	N/A	N/A	0.963	0.970	N/A
Vlachos and Dermatas [41]	0.9285	N/A	0.7468	N/A	N/A	N/A	N/A
Saffarzadeh et al. [42]	0.9387	0.9483	N/A	N/A	0.9303	0.9431	7.6
Li et al. [47]	0.9343	0.9407	0.7154	0.7191	N/A	N/A	8 & 30
Amin and Yan [48]	0.9191	0.9081	0.6608	0.7261	N/A	N/A	10
Cinsdikici and Aydin [82]	0.9293	N/A	N/A	N/A	0.9407	N/A	35
Xiao et al. [83]	0.9529	0.9470	0.7513	0.7147	N/A	N/A	81
Martinez-Perez et al. [135]	0.9181	N/A	0.6389	N/A	N/A	N/A	N/A
Yin et al. [87]	0.9267	0.9412	0.6522	0.7248	N/A	N/A	378
Mendonca and Campilho [84]	0.9463	0.9479	0.7315	0.7123	N/A	N/A	150
Miri and Mahloojifar [88]	0.9458	N/A	0.7352	N/A	N/A	N/A	50
Jiménez et al. [136]	0.9430	N/A	0.6960	N/A	N/A	N/A	N/A
Szpak and Tapamo [138]	0.9299	N/A	N/A	N/A	N/A	N/A	N/A
Zhao et al. [139]	0.9477	0.9509	0.7354	0.7187	N/A	N/A	119
Salazar-Gonzalez et al. [140]	0.9478	0.9479	0.6782	0.7197	N/A	N/A	N/A
Tagore et al. [144]	0.9424	0.9497	N/A	N/A	0.9531	0.9611	N/A
Dai et al [145]	0.9347	0.9392	0.6542	0.6503	N/A	N/A	N/A
Kande et al. [147]	0.8911	0.8976	N/A	N/A	0.9518	0.9298	N/A
Lupascu et al. [150]	0.9459	N/A	0.6562	N/A	N/A	N/A	N/A
Lupascu et al. [150]	0.9482	N/A	0.6565	N/A	N/A	N/A	N/A

Lupascu et al. [150] trained a self-organising map (SOM) on retinal images and

proposed two vessel segmentation techniques. The map was further divided into two classes using k-means clustering technique and modified fuzzy c-means clustering algorithm. The entire image is fed into the SOM again and the class of the best matching unit on the SOM is assigned to each pixel. A post-processed technique based on hill climbing strategy on connected components was used to detect the vessel network. An average sensitivity rate of 0.6562 and an average accuracy rate of 0.9459 were achieved using the k-means clustering technique on DRIVE database while an average sensitivity rate of 0.6565 and an average accuracy rate of 0.9482 were achieved using the fuzzy c-means clustering on DRIVE database. The drawback of this method is the high presence of false vessel detection around the border of the optic disc. This method also failed to detect the thinner vessels.

2.3 Retinal Vessel Tortuosity Measurement

Retinal vessel morphological features such as vessel tortuosity, vessel width, branching angle and branching coefficient are often early symptom indicators of some retinopathies [68], [120] and are of prognostic importance in ROP [121]. One of the first changes in vessels morphology to occur in DR patients is the increase in vessel tortuosity [50], [51], [61]. Tortuosity has also been identified as a more reliable vascular parameter in differentiating ROP severity than the vessel width [49]. Retinal vessel network tortuosity is the measure of twists and curvature of a vessel. Vessel tortuosity measures are used to determine the possibility of retinal images to be healthy or diseased even when there are no visible pathologies as shown in Figure 2.2.

High blood pressure has been linked to diabetes due to its relationship with hypertension [151], [152], [153] and tortuosity has also been identified as an indicator of high blood pressure. The degeneration of retinal vessel walls and changes in their elastic properties have also been identified to be major causes of vessel tortuosity [52]. The duration of diabetic disease has a strong effect on changes in vessel tortuosity [154], [155]. DR is often accompanied by an increase in the tortuosity of small vessels [156], [157], [158], [159].

Although vessel tortuosity are visually analysed and determined by ophthalmologists based on the curvature and twisting rate of vessels, qualitative grading of vessel tortuosity suffers from inter-observer and intra-observer variations [160]. Several methods have been applied to quantitatively (numerically) determine the measure of tortuosity of a vessel [68], [85]. The term often called the tortuosity index (TI) is used for the estimation of the vessel tortuosity. TI provides a reproducible measure of vessel

Figure 2.2: (a) Coloured Retinal Image With Normal Vessels (b) Coloured Retinal Image With Tortuos Vessels.

characteristics. Several tortuosity measurement methods have been proposed in the literature. Vessel tortuosity was first computed as the ratio of the actual vessel length to the length of the underlying chord by Lotmar et al. [55] and further applied in [53], [54], [56], [57]. This approach assumes a vessel to be non-tortuous if it is a straight line and tortuous while the radius of curvature is longer than the chord length of the vessel. The techniques, however, failed to differentiate varying vessels with the same length but with different tortuosity as shown in Figure 2.3.

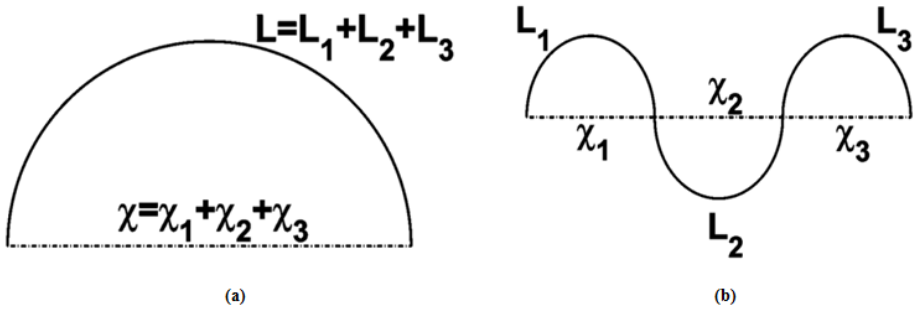

Figure 2.3: (a) & (b) have the same arc length and chord length but different tortuosity i.e. if T = $\frac{L}{X}$ [85].

Bullit et al. [85] applied the number of inflection points for the automatic vessel tortuosity measure to overcome the drawback of the arc length over chord length ratio methods. The use of inflection points as described in [85] is, however, insufficient

to describe all the vessels twists. Hart et al. [58] implemented automatic tortuosity measurement using the integral curvature methods. Dougherty and Varro [161] used second derivatives along central axis of the blood vessels for automatic tortuosity measurement. Grisan et al. [59], [162] implemented automatic tortuosity measures using the arc to chord ratio and the points of changing curvature sign. This algorithm applied manually traced vessel centre points for inflection point placement. Capowski et al [49] addressed tortuosity measurement using the number of direction changes in vessel course. Azegrouz et al. [52] proposed a vessel-thickness tortuosity measurement method utilising the average of the two curvature values computed at two boundary points of the vessel. Vessel tortuosity measurement based on a chain code was recently proposed in [60]. The major drawbacks of chain code are its inaccuracies in areas of high curvature and regions of low curvature [86].

Generally, automatic tortuosity measurement methods based on local tortuosity measurement perform better while compared to the techniques based on global tortuosities [57]. However, the contribution of each local tortuosity measure is considered for computing the global tortuosity measure.

2.4 Summary

In the face of the global prevalence of DR and ROP, the cases of vision loss and blindness tend to increase in the absence of efficient detection and management approaches of the diseases. The use of automatic vessel segmentation and analysis in retinal images by ophthalmologist, however, provides an efficient means of diagnosis and management of the various retinopathies thus alleviating the limitation of manual detection and analysis of the retinal vessels.

Although the superior performance of the supervised methods over the unsupervised methods have been shown in the literature, these supervised methods are computationally expensive since training time is required [32], [81]. Another major drawback of the supervised vessel segmentation techniques [20], [22], [23], [32] is that their performance is highly dependent on the labelled training sample by experts which could sometimes be extremely difficult, expensive or unavailable [16]. Furthermore, a new set of labelled training sample is often required for retraining to obtain good segmentation performance when detecting vessels on a new set of retinal images [20], [22], [23]. While some of the previous unsupervised segmentation methods [21], [38], [39], [41], [42], [47], [48], [82] are computationally faster when compared to the supervised vessel segmentation methods, they are, however, faced with the inability to detect the thin vessels

[41], [42], [69], [135] as well as the limitation of unconnected vessel network structures [38]. Although some unsupervised techniques [43], [34], [46], [83], [84] have made some progress in improving the automatic detection of retinal vessels, there is a need for further improvements in the detection of thinner vessels and the computational running time required for the segmentation of vessels. The presence of a lot of false positives around the border of the optic disk also remains a challenge in the vessel segmentation techniques [20], [42].

Although several vessel tortuosity methods have been discussed in the literature, there is still need for an improved method that efficiently detects vessel tortuosity. The drawback of the arc-chord ratio methods [53], [54], [56], [57] was identified as the inability to differentiate varying vessels tortuosity when they have the same length but different number of vessel twists. Methods based on inflection points are also not robust enough as all the vessels twists are not sufficiently described [85]. The major drawbacks of chain code based curvature measurement method were also identified to be inaccuracies obtained in the areas of high curvature and regions of low curvature [86].

The following chapter shall investigate the use of unsupervised segmentation approach for a robust automatic segmentation of retinal vessel network. An investigation into the tortuosity measurement method that efficiently detects vessel directional change and twists shall also be presented.

Chapter 3

Materials and Methods

3.1 Introduction

Generally, automated vessel segmentation is a challenging problem due to complexities such as the varying width of retinal vessels from very large to very small, low contrast of thin vessels with respect to background and noise due to nonhomogeneous illumination caused by the complex acquisition of the retinal images [1], [47]. Since efficient vessel network detection is a very important step needed in ophthalmology for reliable retinal vessel characterisation, an efficient segmentation technique that requires no labelled training sample and performs the segmentation of large and thin vessels in a timely efficient manner is highly needed. This chapter describes the dataset used in this research. The unsupervised segmentation methods investigated in this research are also presented. Furthermore, an investigation on the vessel tortuosity measures that combine distance metric and vessel twists for the characterisation of the detected vessel is presented.

3.2 Dataset

The retinal images used for vessel segmentation in this research were obtained from two major publicly available databases namely, DRIVE (Digital Retinal Images for Vessel Extraction) [131] and STARE [132]. These two databases are selected because the retinal vessel segmentation methodologies are evaluated on them.

DRIVE [131] is a publicly available database consisting of 40 colour retinal fundus images. These images were obtained from a diabetic retinopathy screening program in the Netherlands. The images were acquired using a Canon CR5 non-mydriatic 3CCD

camera with a 45 degree field of view (FOV). Each image was captured using a 24-bit RGB colour at 768×584 pixels. The FOV of each image is circular with a diameter of approximately 540 pixels. This set of forty colour retinal fundus images are divided into two groups. The first group of the images is a training set made up of twenty images. The second group is a testing set made up of twenty images. All the human observers that manually segmented the vessels in the retinal images were instructed and trained by an experienced ophthalmologist. They were asked to mark all the pixels for which they were for at least 70% certain that they were vessel. A set of manual segmentation of the vessel network is available for the training images. Two manual segmentations sets X and Y are available for the test cases. In set X, 577,649 pixels were marked as vessel and 3,960,494 pixels as background (12.7% vessel). In set Y, 556,532 pixels were marked as vessel and 3,981,611 as background (12.3% vessel). It was, however, observed that it took a human observer an average time of 7200 seconds (2 hours) to segment the vessels in each of the retinal images. Set X of the manual segmentations of the test cases is used as gold standard while set Y is often compared to the performance of the automatic segmentation techniques on the database. Figure 3.1 shows an image in set X (that is gold standard) and its equivalent in set Y (i.e second human observer) on DRIVE database.

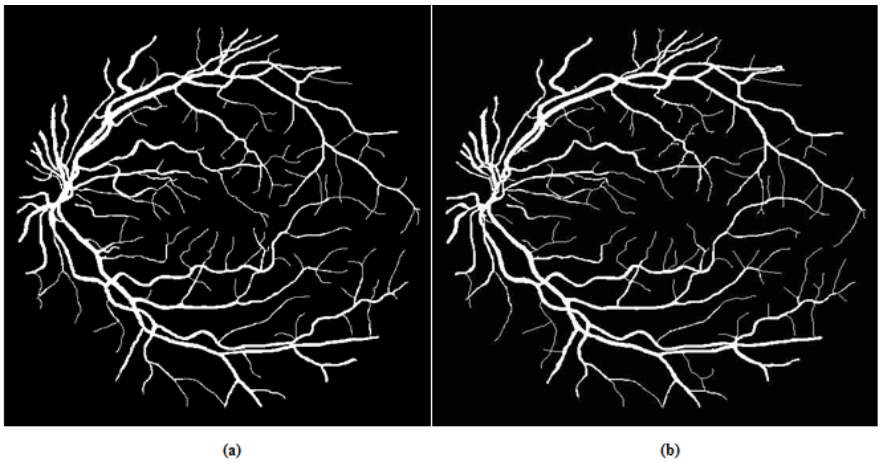

Figure 3.1: (a) Segmented vessels of an image on DRIVE database by the first human observer (also referred to as Set X) used as the ground truth of DRIVE database in the literature (b) Segmented vessels of the same image on DRIVE database by the second human observer (also referred to as Set Y).

STARE (STructured Analysis of the Retina) [132] is a publicly available database

that consists of 20 retinal images captured with the use of TopCon TRV-50 fundus camera with 24-bit grey-scale resolution and spatial resolution of 700 × 605 pixels. The approximate diameter of the FOV is 650 × 500 pixels. Two observers manually segmented all the images. The first observer segmented 10.4% of pixels as vessel, against 14.9% vessels for the second observer. The segmentations of the two observers are fairly different in that the second observer segmented many more of the thinner vessels than the first one. The 20 manually segmented images provided by the first observer is used as the ground truth for the comparative performance evaluation of different vessel segmentation algorithms in the literature. Figure 3.2 shows a ground truth of segmented vessel and its equivalent for the second human observer on STARE database.

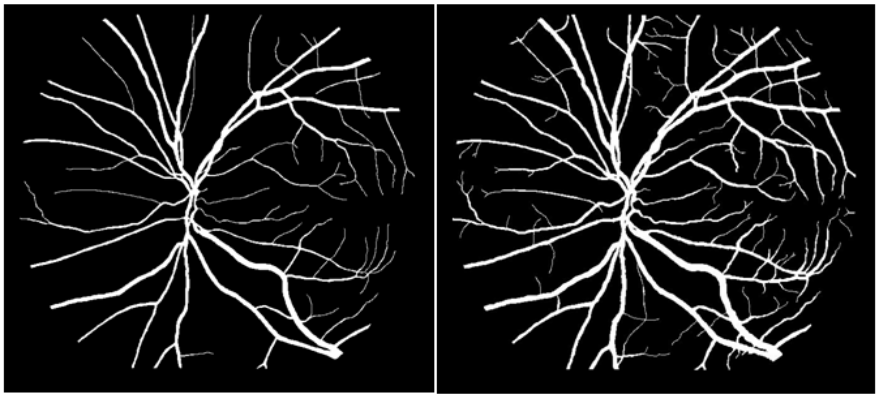

Figure 3.2: (a) Segmented vessels of an image on STARE database by the first human observer used as the ground truth of in the literature ground truth (b) Segmented vessels of the same image on STARE database by the second human observer.

In related development, 50 digital fundus images containing 50 different vessel segments were used for the vessel tortuosity measurement. An expert's ground truth that determines the state of each vessel segment as either tortuous or normal was also obtained from an ophthalmologist consultant.

3.3 Unsupervised Segmentation Method

In the previous chapter, this research showed that the supervised vessel segmentation methods [20], [22], [23], [28], [32], [34], [35], [36], [37] achieved higher vessel detection and accuracy rates than the previously proposed unsupervised methods [21], [38], [39],

[42], [47], [48], [82]. The major drawbacks of the supervised vessel segmentation techniques [20], [22], [23], [32] were shown to be the high dependence of their performance on the labelled training sample by the experts which could sometimes be extremely difficult, expensive or unavailable [16] and the requirement of new sets of labelled training sample for the retraining of the classifiers to obtain good segmentation performance when detecting vessels on new sets of retinal images [23], [28]. The previous chapter also showed that supervised vessel segmentation approach is time-consuming as it requires manually detected vessels and supervised training before the classification of pixel as either vessel or background. In contrast to the supervised vessel segmentation methods, unsupervised segmentation methods do not require labelled data for training. It was also showed in the previous chapter that while some of the previous unsupervised segmentation methods [21], [38], [39], [41], [42], [47], [48], [82] are computationally faster when compared to the supervised vessel segmentation methods, they are faced with the inability to detect the thin vessels [41], [42], [69], [135] and connectivity loss of vessel network structures [38], [69]. Although some unsupervised techniques [43], [34], [46], [83], [84] have made some progress at improving the automatic detection of retinal vessels, their needs for further improvements in the detection of thinner vessels and the computational running time required for the segmentation of vessels were also discussed. The need for the reduction of false vessels around the border of the optic disk in the segmented vessels [20], [42] was also identified.

In the following sections 3.4, 3.5 and 3.6, different unsupervised vessel segmentation methods are investigated to address the problems of inability to detect the thinner vessels [41], [42], [69], [135], connectivity loss in vessel network [38], computational running time complexity [43], [34], [46], [83], [84], [32], [81] and false vessels around the border of the optic disk [20], [42]. Since unsupervised vessel segmentation are not dependent on labelled training set, the investigated methods also overcome the major drawback of supervised segmentation methods which is their high dependence on the labelled training [16], retraining of the classifiers [23], [28].

The unsupervised vessel segmentation methods investigated in this research are grouped into three categories namely global thresholding techniques, local adaptive thresholding techniques and clustering-based techniques.

3.4 Global Thresholding Techniques

Retinal fundus images are often characterised by noise due to illumination and contrast variation. Due to this, the use of global thresholding techniques for the detection of

vessels in these noisy retinal images becomes challenging. Although global thresholding technique was applied on matched filter response (MFR) in [26], a threshold probing technique that combined local vessel attributes with region-based attributes improved the performance of the global thresholding method applied on the MFR for retinal vessel segmentation in [21]. It is also important to state that a poor choice of pre-processing technique applied to handle the retinal image noise can also result in a poor detection of vessel in retinal images [33].

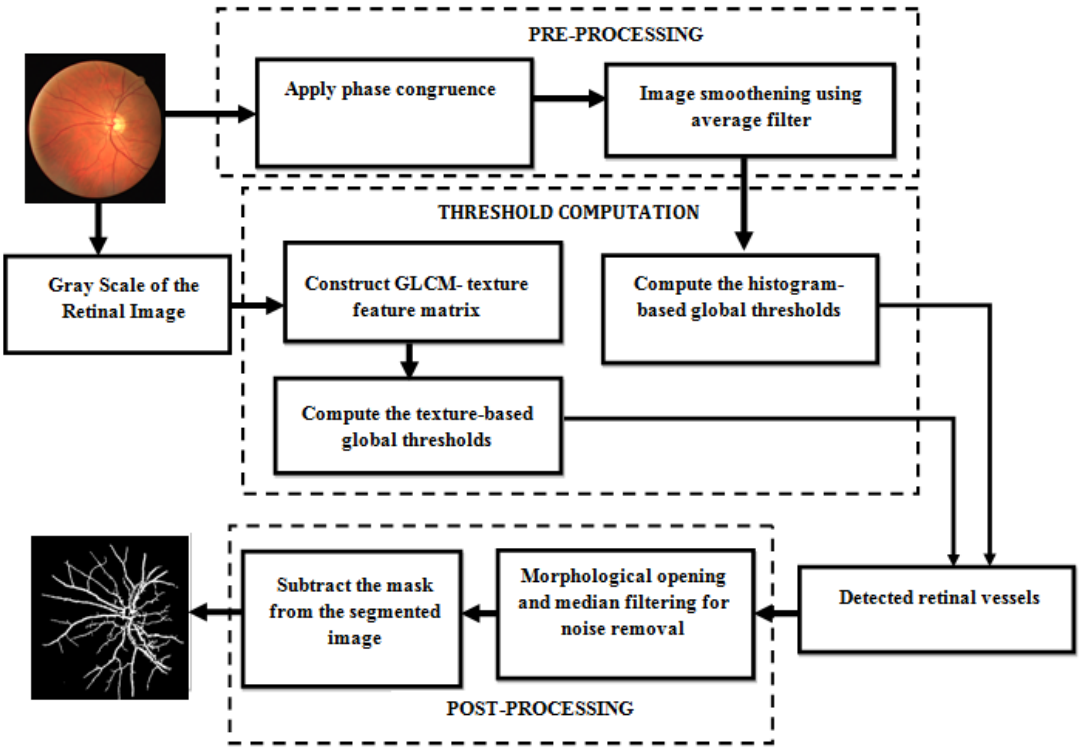

Figure 3.3: Phase Congruence-Based Global Thresholding Approach.

This section presents a further study on the use of different global thresholding techniques while combined with different pre-processing and post-processing techniques. Two different techniques namely Contrast Limited Adaptive Histogram Equalisation (CLAHE) and phase congruence while combined with different filtering techniques are used to enhance the vessels in the pre-processing phase. For the purpose of simplification, the segmentation techniques used in this section are categorised into two major approaches namely CLAHE-based global thresholding approach and phase congruence-based global thresholding approach. The phase congruence-based global thresholding approach investigates the use of texture-based global thresholds and histogram-based

global thresholds for the segmentation of retinal vessels as described in Figure 3.3. In a related development, the CLAHE-based global thresholding approach investigates the use of Otsu and ISODATA thresholding for retinal vessel segmentation as described in Figure 3.4.

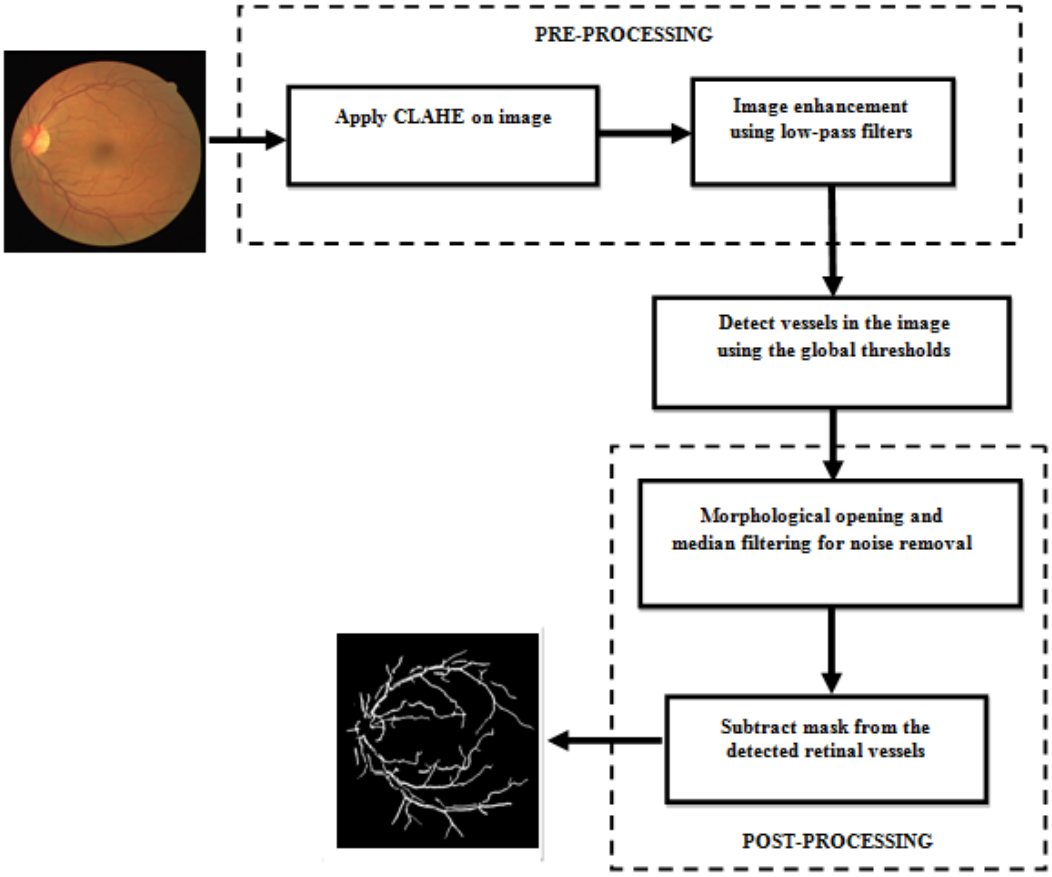

Figure 3.4: CLAHE-Based Global Thresholding Approach.

3.4.1 Pre-Processing Phase

Complexities such as noise due to illumination and contrast variation make the detection of large and thin vessels a very challenging problem [47]. The use of efficient pre-processing techniques to remove the noise and enhance the vessels are highly needed to produce good retinal vessel segmentation results. The different techniques applied in the pre-processing phase are described in sections 3.4.1.1 and 3.4.1.2 below.

3.4.1.1 Contrast Limited Adaptive Histogram Equalisation (CLAHE)

CLAHE is an efficient technique for enhancing images [163]. CLAHE algorithm is used for partitioning the retinal image into contextual regions, and the histogram equalisation is applied to each one. Figure 3.5 shows the coloured, grey scale and the green channel of the retinal fundus image.

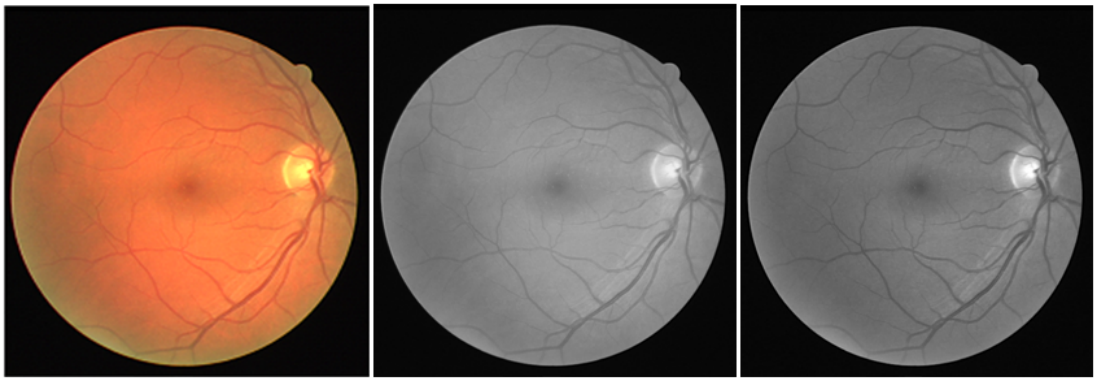

Figure 3.5: (a) Coloured Retinal Image (b) Grey-Scale Retinal Image (c) Green Channel of the Coloured Retinal Image

CLAHE further computes the local histogram at each pixel of the retinal image, performs histogram clipping, histogram renormalisation and output pixel mapping to an intensity proportional to its rank within the histogram. Given that h_i is the histogram bin and $(m \times m)$ the contextual region, the rank r_p for a pixel with intensity p is computed as

$$r_p = \frac{\sum_{i=0}^{p} min(\beta, h_i) + (p+1)\left(\frac{\sum_{k=0}^{N} max(0, h_k - \beta)}{m \times m}\right)}{m \times m} \tag{3.1}$$

where the clip limit β determines the contrast enhancement limit and $\sum_{i=0}^{p} min(\beta, h_i)$ describes the rank in a clipped histogram. Since each region will have a different number of clipped pixels, It is beneficial to redistribute the part of the histogram that exceeds the clip limit β evenly among all histogram bins to normalise the ranks computed in different regions. This normalisation is provided by $\sum_{j=0}^{p} \frac{\sum_{k=0}^{N} max(0, h_k - \beta)}{m \times m}$, where h_k is the histogram bin in the different region. The rank of intensity i_{in} at (x,y) is computed, and scaled to produce a fractional rank r, such that $0.0 \leq r \leq 1.0$.

The output intensity level i_{out} is then computed in some grey scale ranging between

i_1 and i_2 as:

$$i_{out} = i_1 + r \times (i_2 - i_1) \tag{3.2}$$

where i_1 and i_2 are the minimum and maximum intensity levels respectively.

3.4.1.2 Phase Congruence

A phase is congruent when the phases of all the Fourier components at the positions are aligned [143]. Morrone and Owens [164] defined phase congruency function in relation to the Fourier decomposition of a signal at some position x to be:

$$PC(x) = max_{\phi(x)\epsilon[0,2\pi]} \frac{\sum_k A_k \cos(\phi_k(x) - \overline{\phi(x)})}{\sum_k A_k(x)} \tag{3.3}$$

where the amplitude A_k is the k_{th} Fourier component, and $\phi_k(x)$ is the local phase at location k. The amplitude weighted mean local phase angle of all the Fourier terms at the position under consideration yields the value $\overline{\phi(x)}$ that maximises equation (3.3). Computing the cosine of the difference between the actual phase angle of a frequency component and the weighted mean, $\overline{\phi(x)}$, gives the Taylor expansion $\cos(x) \approx 1 - x^2/2$ for lower values of x.

Venkatesh and Owens [165] as an alternative to [164], computed points of maximum phase congruency through the search for the local energy function peaks. The local energy function E(x) of a luminance profile I (x) is defined in [165] as

$$E(x) = \sqrt{F^2(x) + H^2(x)} \tag{3.4}$$

Such that F(x) is the signal I(x) after the removal of its DC component while H(x) is the Hilbert transform of F(x).

Given that I is the signal and M_e^k and M_o^k are the even-symmetric (cosine) and odd-symmetric (sine) wavelets respectively at scale k, the amplitude of the transform is computed as

$$A_k(x) = \sqrt{((I(x) * M_e^k) + (I(x) * M_o^k))} \tag{3.5}$$

and the phase is computed as

$$\phi(x) = \arctan 2(I(x) * M_e^k, I(x) * M_o^k) \tag{3.6}$$

The energy E(x) was further computed in terms of phase congruency *PC(x)* and

Fourier amplitudes A_k in [165] as

$$E(x) = PC(x) \sum_k A_k(x) \tag{3.7}$$

Given phase offset $\phi_k(x)$ and weighted mean phase angle of $\overline{\phi(x)}$, the local energy $|E(x)|$ is also computed as

$$E(x) = \sum_k A_k(x) \cos(\phi_k(x) - \overline{\phi(x)}) \tag{3.8}$$

Hence, the phase congruency is computed as

$$PC(x) = \frac{|E(x)|}{\sum_k A_k(x)}, 0 \leq PC(x) \leq 1 \tag{3.9}$$

Kovesi [142] handled the ill-conditioned computation of phase congruency when all the Fourier amplitudes are very small by adding a small positive constant ε, to the denominator of the phase congruency expression as

$$PC(x) = \frac{|E(x)|}{\sum_k A_k(x) + \varepsilon} \tag{3.10}$$

where the value of ε is determined by the precision of the performance of the different operations on the signal.

Kovesi [142] also estimated the level of noise in the calculation of the local energy on the premise that when a signal noise is additive, the noise power spectrum is constant, and that the features like edges occur only at disjointed locations. Hence, the phase congruency that includes the removal of the estimated signal noise is computed as

$$PC(x) = \frac{\sum_\theta \sum_k W_\theta(x) \lfloor A_{k,\theta} \triangle \phi_{k,\theta}(x) - T \rfloor}{\sum_\theta \sum_k A_{k,\theta}(x) + \varepsilon} \tag{3.11}$$

In order to compute an overall measure of phase congruency in 2-D images, a computationally efficient phase congruence model on 2-D images was proposed in [142]. Hence, equation (3.11) for signal is rewritten for 2-D images in [142] as

$$PC(x,y) = \frac{\sum_\theta \sum_k W_\theta(x,y) \lfloor A_{k,\theta} \triangle \phi_{k,\theta}(x,y) - T_\theta \rfloor}{\sum_\theta \sum_k A_{k,\theta}(x,y) + \varepsilon} \tag{3.12}$$

where *(x,y)* is the position of the pixel in the green channel of the retinal image, while k and θ represent the scale and orientation respectively. W_θ is the weighing factor for the distributed frequency, while T_θ estimates the image noise. The energy is

computed using $A_{k,\theta} \triangle \phi_{k,\theta}(x, y)$, while ε is added to the denominator such that the divisor will be nonzero. Figure 3.6 shows the output of pre-processed images using phase congruence.

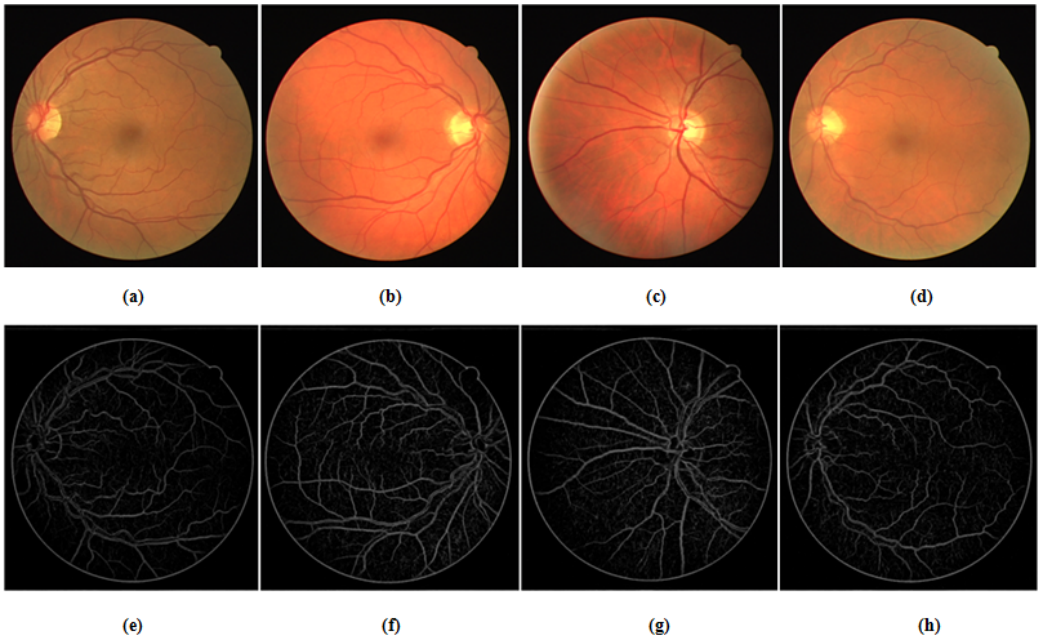

Figure 3.6: (a) to (d) Coloured Retinal Images on DRIVE database (e) to (h) Phase Congruence-Based Pre-Processed Images

3.4.2 Global Thresholding

Automatic thresholding is potentially useful to dynamically select an optimal grey-level threshold value for the segmentation of retinal vessels in the image from the background tissue based on their intensity distribution. Global thresholding methods apply information obtain globally (for example, image histogram, global texture properties) to the entire image [166]. The different global thresholding techniques studied in this research are discussed in sections 3.4.2.1, 3.4.2.2, 3.4.2.3 and 3.4.2.4.

3.4.2.1 Otsu Thresholding

Global thresholding technique based on Otsu [167] is used on the results computed from phase congruence and CLAHE with filters for the initial estimation of the vessel network. The threshold that minimises the intra-class variance as a weighted sum

of variances of the two classes is explored in Otsu's method. The weighted sum of variances of two classes is expressed as

$$\sigma_{\omega}^2(t) = \omega_1(t)\sigma_1^2(t) + \omega_2(t)\sigma_2^2(t) \tag{3.13}$$

such that weights ω_i describe the probabilities of the two classes separated by a threshold t and σ_i^2 variances of the classes. The class probability $\omega_1(t)$ is then computed from the histogram as:

$$\omega_1(t) = \sum_{0}^{t} p(i) \tag{3.14}$$

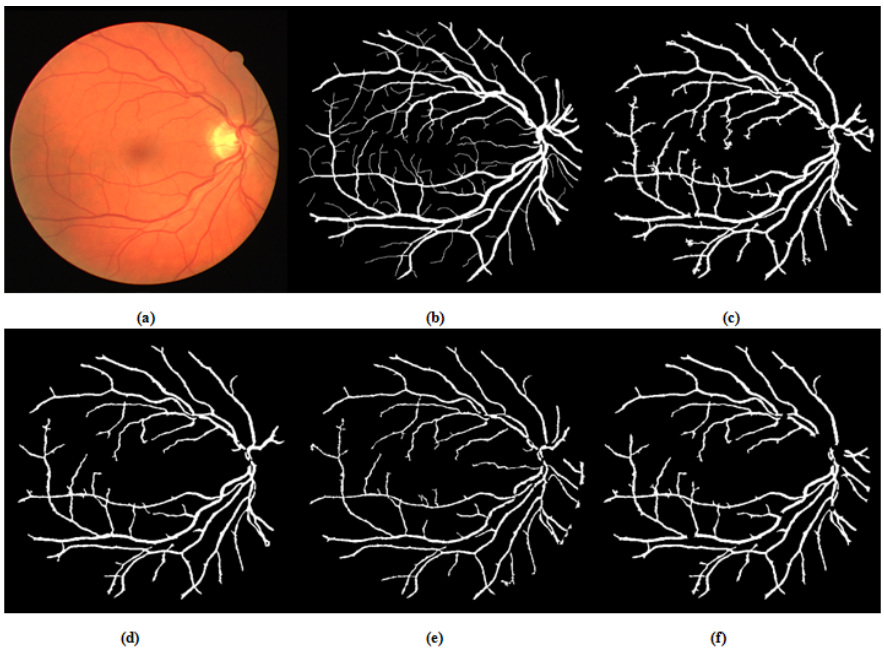

Figure 3.7: Segmented vessels obtained through CLAHE with Otsu thresholding technique and different filters. (a) DRIVE coloured retinal image. (b) DRIVE database gold standard image. (c) Segmented vessels using Otsu threshold with Gaussian filter. (d) Segmented vessels using Otsu threshold with average filter. (e) Segmented vessels using Otsu threshold with adaptive filter. (f) Segmented vessels using Otsu threshold with combination of average and Gaussian filters.

where p(i) is the normalised frequency of each grey level value i. The class mean

$\mu_1(t)$ is computed as:

$$\mu_1(t) = \frac{[\sum_0^t p(i)x(i)]}{\omega_1} \tag{3.15}$$

such that *x(i)* is the value at the centre of the *ith* histogram bin. $\omega_2(t)$ and $\mu(t)$ can likewise be computed on the histogram for bins greater than t. Otsu further showed that minimising the intra-class variance is the same as maximising inter-class variance. Hence, the desired threshold $\sigma_b^2(t)$ is given as

$$\sigma_b^2(t) = \sigma^2(t) - \sigma_\omega^2(t) = \omega_1(t)\omega_2(t)[\mu_1(t) - \mu_2(t)]^2 \tag{3.16}$$

where $\mu_1(t)$ and $\mu_2(t)$ are the mean of the first and second group respectively. Hence, the Otsu threshold is

$$T_h = \sigma_b^2(t) \tag{3.17}$$

Figure 3.7 shows the segmented vessels obtained from CLAHE and Otsu thresholding after post-processing on DRIVE database.

3.4.2.2 Isodata Threshold Selection

Isodata threshold technique divides the histogram of the image output from phase congruence method into two using an initial threshold value t_0. The threshold is computed as:

$$t_h = \frac{m_1 + m_2}{2} \tag{3.18}$$

where m_1 and m_2 are the mean values of the two different parts of the histogram. This process continues until $t_h \approx t_{h-1}$ and Isodata threshold is

$$T_h = t_h \tag{3.19}$$

Figure 3.8 shows the segmented vessels obtained from CLAHE and Isodata thresholding after post-processing on DRIVE database

3.4.2.3 Inverse Difference Moment (IDM)-Based Thresholding

Image signal statistics, particularly first- and second-order statistics, are good texture feature descriptors used for supervised segmentation techniques. Moments, first-order statistics, are concerned with individual image pixel properties while second-order

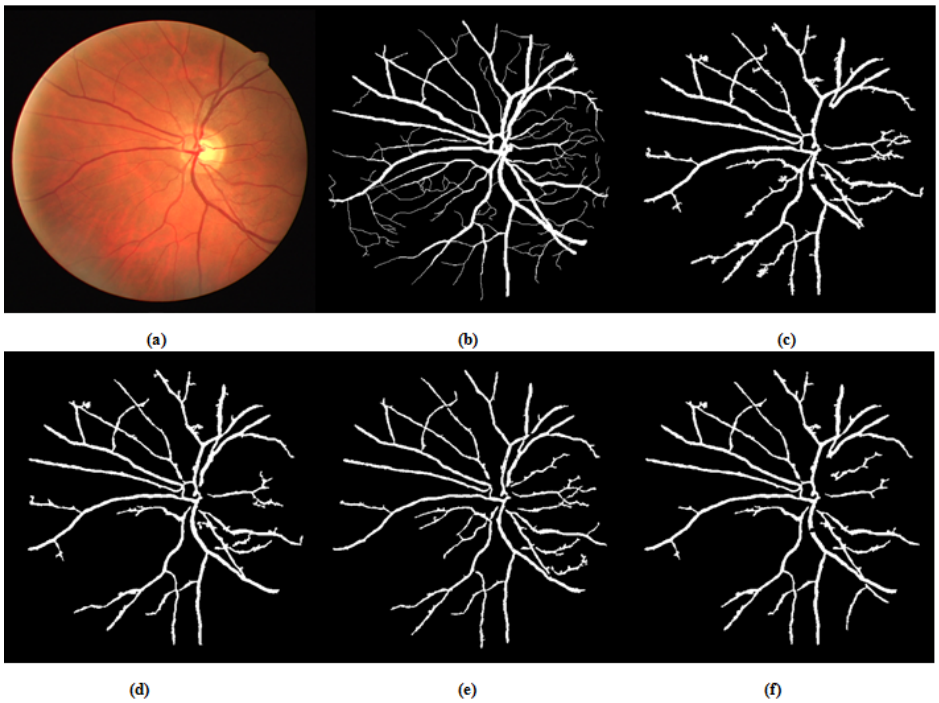

Figure 3.8: CLAHE and ISODATA thresholding technique with different filters. (a) DRIVE coloured retinal image.(b) DRIVE database gold standard image. (c) Segmented vessels using ISODATA threshold with Gaussian filter. (d) Segmented vessels using ISODATA threshold with average filter. (e) Segmented vessels using ISODATA threshold with adaptive filter. (f) Segmented vessels using ISODATA threshold with combination of average and Gaussian filters.

statistics such as grey level co-occurrence matrix (GLCM) are concerned with individual pixel properties as well as the spatial inter-dependency of the two pixels at particular relative positions.

GLCM is popularly known for its usage in texture image segmentation [168]. Haralick features [168] computed from GLCM have been used for both supervised [169], [170] and unsupervised [171], [172], [173] [174] image segmentation techniques. Six of the features proposed by Haralick et. al.[168] were considered to be the most relevant [175]. The features considered are Energy (ENER), Entropy (ENT), Contrast (CONTR), Variance (VAR), Correlation (COR) and Inverse Difference Moment (IDM). Some other unsupervised grey level co-occurrence based segmentation techniques have also been proposed in the literature [175], [176], [177].

Although IDM was originally used in [168] for supervised segmentation, this research utilises it for an unsupervised segmentation approach. The IDM texture infor-

mation applied in this research is computed using the GLCM of the grey scale of the retinal fundus image. Due to the large variation in the widths of the vessels [47], a multi-scale approach is adopted for the computation of a global threshold to segment the vessel network. The GLCM for the retinal fundus image is computed using the relative distance 'd' between the pixel pair and their relative orientation 'Φ' across four directions (horizontal: 0^0, diagonal: 45^0, vertical: 90^0 and anti-diagonal: 135^0) as

$$C_{i,j} = \sum_{x=0}^{M-1} \sum_{y=0}^{N-1} (P\{V(x,y) = i \ \& \ V(x \pm d\Phi_1, \ y \pm d\Phi_2) = j\}) \tag{3.20}$$

where $V(x,y) = i$, means i is the grey level of the pixel (x,y), and P is defined as

$$P(x) = \begin{cases} 1 & \text{if x is true} \\ 0 & \text{Otherwise} \end{cases} \tag{3.21}$$

The IDM feature across the different distances, 'd', and varying relative orientations, 'Φ', is defined as

$$IDM_{(d,\Phi)} = \sum_{i,j} p_{(i,j)}/(1 + (i+j)^2) \tag{3.22}$$

where $p_{(i,j)}$ is the $(i,j)^{th}$ entry in a normalised grey scale spatial dependence matrix $C_{(i,j)}/R$ and R is the number of neighboring resolution cell pairs.

A Multi-Scale IDM-Feature measurement across the varying distance 'd' and relative orientation 'Φ' is used in the computation of an IDM feature matrix as:

$$F = \begin{pmatrix} f_{11} & f_{12} & f_{13} & f_{14} \\ f_{21} & f_{22} & f_{23} & f_{24} \\ f_{31} & f_{32} & f_{33} & f_{34} \\ f_{41} & f_{42} & f_{43} & f_{44} \end{pmatrix} \tag{3.23}$$

where $f_{ij} = IDM_{d_i,\Phi_j}$ with orientations $(\Phi_j)_{i=1,\ldots,4}$, such that $\Phi_1 = 0^o$, $\Phi_2 = 45^o$, $\Phi_3 = 90^o$ and $\Phi_4 = 135^o$, with distances $(d_i)_{i=1,\ldots,4}$. Since the width of retinal vessels can vary from very large (15 pixels) to very small (3 pixels)[47], the multi-scale approach adopted investigates the distances $(d_i)_{i=1,\ldots,4}$ across the four orientations as it covers adequate spectrum of vessel texture information ($4 \times 4 = 16$) to compute the global

threshold. The range measure of F is given below as:

$$R_\Phi = \max_{1\leq j\leq 4}(f_{ij}) - \min_{1\leq j\leq 4}(f_{ij}) \tag{3.24}$$

where $1 \leq i \leq 4$ and R_Φ is a row vector containing the range of each column of matrix (F).
The threshold value that will be used for the binarisation of the output image from the phase congruence and average filter is computed as:

$$T_h = max(R_\Phi) + mean(R_\Phi) \tag{3.25}$$

Figures 3.9 and 3.10 show the segmented vessels obtained from phase congruence and IDM-based global thresholding after post-processing on DRIVE and STARE databases respectively.

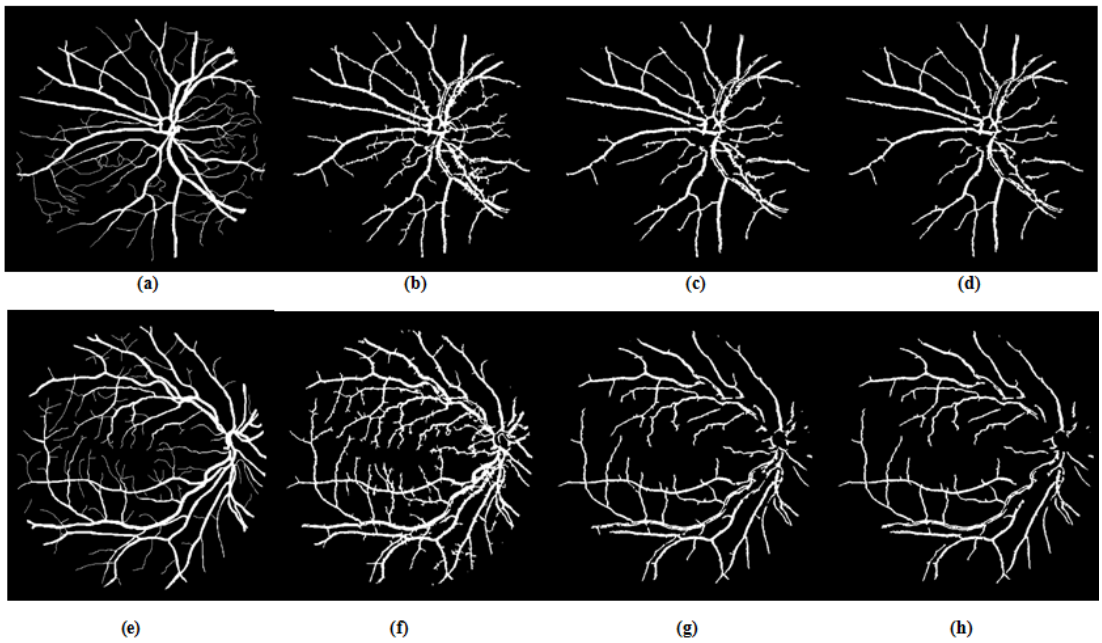

Figure 3.9: Retinal images and the segmented vessels obtained through phase congruence using different global-based thresholding techniques. Images (a) and (e) are DRIVE database gold standards. Images (b) and (f) are images segmented using IDM-based threshold values while images (c) and (g) are images segmented using ISODATA threshold values. Images (d) and (h) are images segmented using Otsu threshold values.

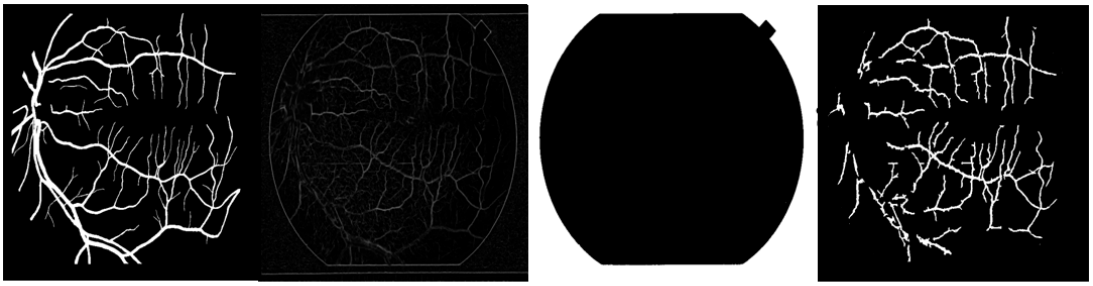

Figure 3.10: (a) STARE database ground truth. (b) Pre-processed image using Phase Congruence. (c) Retinal Image Mask (d) Segmented vessel network using Phase Congruence-Based global thresholding approach.

3.4.2.4 Sum Entropy-Based Thresholding

Entropy has been one of the few major Haralick features that has often been used for unsupervised segmentation. Different entropy based thresholding such as global, local, joint and relative entropy have been proposed in [171], [172], [173] and [174]. The unsupervised segmentation approach applied in this research is different from the previously proposed methods [171], [172], [173] and [174] in that a multi-scale approach is applied in this thesis to compute a global threshold based on sum entropy information to segment the vessel network. A grey-level threshold value based on GLCM sum entropy feature information is computed for the segmentation of the retinal vasculature from the background using the image output from phase congruence technique. The GLCM for the retinal fundus image is computed as described in equation (3.20). The sum entropy feature across the varying distances, 'd', and relative orientation, 'Φ', is defined as

$$Entr^{+}_{(d,\Phi)} = -\sum_{i=2}^{2N_g} \mathrm{P}_{x+y}(k) log\{\mathrm{P}_{x+y}(k)\} \tag{3.26}$$

where $p_{x+y}(k) = \sum_{i=1}^{N_g} \sum_{\substack{j=1 \\ (i+j=k)}}^{N_g} p(i,j)$ and *p(i,j)* is the normalised matrix.

A multi-scale feature measurement of the sum entropy across the varying distance 'd' and relative orientation 'Φ' to manage the variation in the widths of the vessels [47] is applied in the computation of a feature matrix as:

$$E = (e_{ij}), 1 \leq i, j \leq 4 \tag{3.27}$$

where

$$e_{ij} = Entr^{+}_{(d_i,\Phi_j)}, 1 \leq i,j \leq 4 \tag{3.28}$$

Such that Φ_1= 0^o, Φ_2= 45^o, Φ_3= 90^o and Φ_4 = 135^o, with distances $(d_i)_{i=1,...,4}$.

Distances $(d_i)_{i=1,...,4}$ across the four orientations are considered as adequate spectrum of vessel texture information ($4 \times 4 = 16$) is also covered to compute the global threshold based on sum entropy.

The threshold value used for the segmentation of the vessels using the output image from the phase congruence and a mean filter is computed as

$$T_h = \max_{1\leq i\leq 4} \parallel \max_{1\leq j\leq 4}(e_{ij}) - \min_{1\leq j\leq 4}(e_{ij}) \parallel \tag{3.29}$$

Hence, the segmented image is given as

$$S_{im} = \begin{cases} 0, & \text{if } F(x,y) \leq T_h \\ 1, & \text{otherwise} \end{cases} \tag{3.30}$$

where F(x,y) is the output image of the pre-processing phase.

Figures 3.11 and 3.12 show the segmented vessels obtained from phase congruence and sum entropy-based thresholding technique after post-processing on DRIVE and STARE databases respectively.

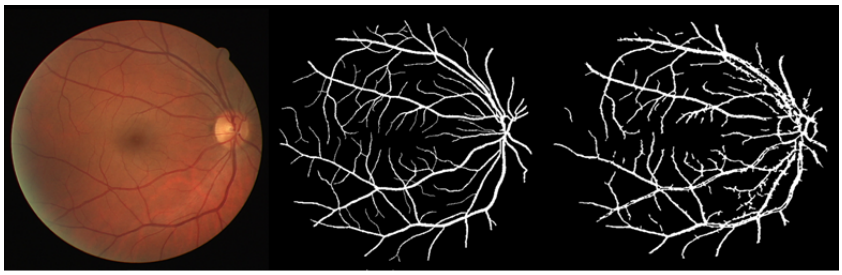

Figure 3.11: (a) Coloured Retinal Image (b) Drive Gold Standard (c) Segmented Vessels Using GLCM Sum-Entropy Threshold Combined with Phase Congruence

3.4.3 Post-Processing Phase

The combination of median filter and morphological opening are used for the post-processing phase to remove noisy pixels and restore the connectivity of several vessel

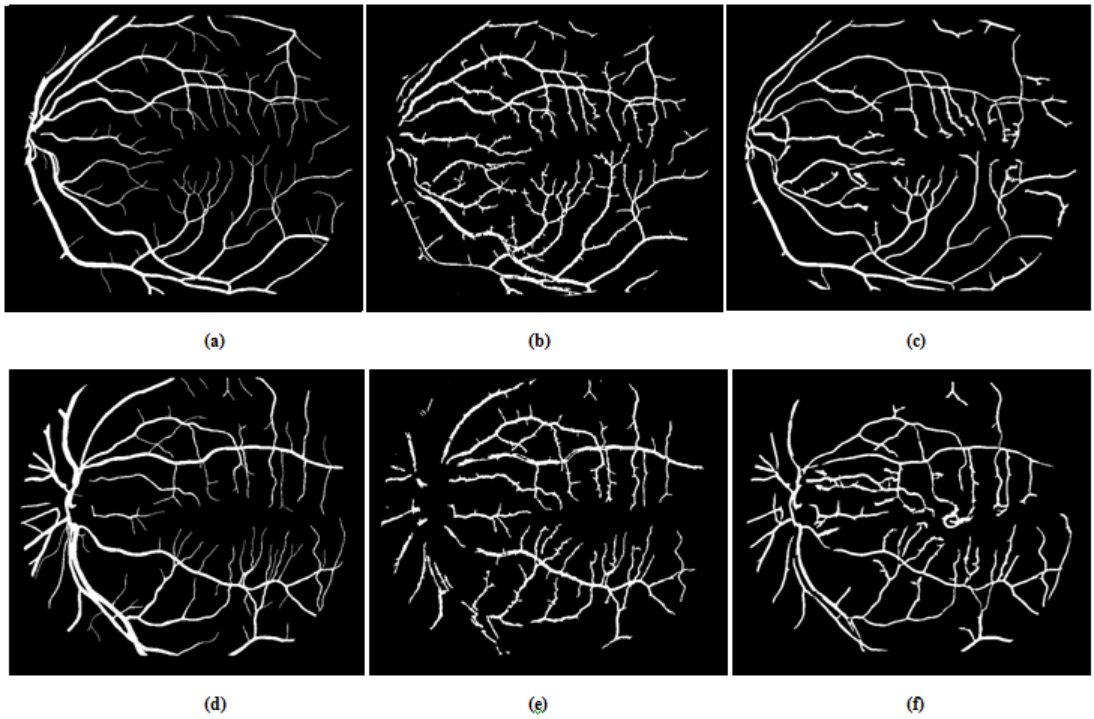

Figure 3.12: (a) & (d) STARE Database Ground Truth. (b) & (e) Segmented Vessels Using GLCM Sum-Entropy Threshold Combined with Phase Congruence. (c) & (f) Segmented Vessels Presented by Hoover et al. [21].

lines by revealing some hidden pixels that belong to vessel lines. Median filtering is a non-linear smoothing operation often used in image processing to reduce noise and preserve edges at the same time. In this research, the median filtering is performed by moving a 2×2 sliding-window through all the pixels of the binarised retinal image containing detected vessels. Since this noisy pixels are isolated from the vessels and surrounded by a wider space of non-vessel background, a 2×2 median filter is applied. This is followed by morphological opening. In the application of morphological opening to the filtered image, erosion is applied to remove the remaining noisy pixels and dilation is subsequently applied for the restoration of the connectivity of several vessel lines. Given that the filtered segmented image is $S_{im}^{filtered}$, the final output image after the application of morphological opening is computed as:

$$\gamma(S_{im}^{filtered}) = \delta(\varepsilon(S_{im}^{filtered})) \tag{3.31}$$

where $\gamma(S_{im}^{filtered})$ is the final segmented vessel network after post-processing and $\varepsilon(S_{im})$ describes the application of erosion and $\delta(S_{im}^{filtered})$, the application of dilation.

3.5 Local Adaptive Thresholding Techniques

The segmentation of retinal vessels are challenging problems due to the noise from nonhomogeneous illumination as well as complexities such as varying width of retinal vessels from very large to very small, and low contrast of thin vessels with respect to background [1], [47]. Since efficient vessel network detection is a very important step needed in ophthalmology for reliable retinal vessel characterisation, an efficient segmentation technique that will perform the detection of large and thin vessels in a timely efficient manner is highly needed. Local adaptive thresholding technique is a very good choice of segmentation when the background of an image is uneven as a result of poor or non-homogeneous illumination conditions. Although some adaptive thresholding techniques [38], [110], [137] have been implemented for the segmentation of retinal vessels, their inability to efficiently detect some large vessels [38] as well as thin vessels [38], [110], [137] and vessel connectivity loss remain unresolved [38] as shown in Figure 3.13. Such inabilities to detect large vessels and thin vessels as well as the problem of vessel disconnection will make the analysis of retinal vascular for retinopathy disease detection very difficult as the detailed vessel information required for vessel morphological analysis and disease diagnosis is not available.

Due to the non-homogeneous illumination, low contrast of thin vessels and large variation in the widths of the retinal vessels [47], this section investigates the use of two new local adaptive thresholding techniques for the segmentation of large and thin retinal vessels based on two different Haralick [168] texture features namely local homogeneity and energy. Although these two texture features have been applied for supervised image segmentation in the literature [168], their novelty in this thesis lie in that they are applied using an unsupervised image segmentation approach. Rather than adopting a global approach, each of these local adaptive thresholding techniques locally applies a multi-scale approach on the different texture information considering the pixel of interest in relationship with its spacial neighbourhood to compute the local adaptive threshold. The multi-scale thresholding approach handles the challenge of vessel width variation. Figure 3.14 presents the flowchart of the adaptive thresholding methods investigated in this research. An unsharp filter is used to sharpen the image. This is followed by the smoothing of the image through an average filter and the enhancement of the image contrast to improve the contrast of thin vessels. Each pixel of the enhanced image in relation to a local neighbourhood is convolved through a median filter of local

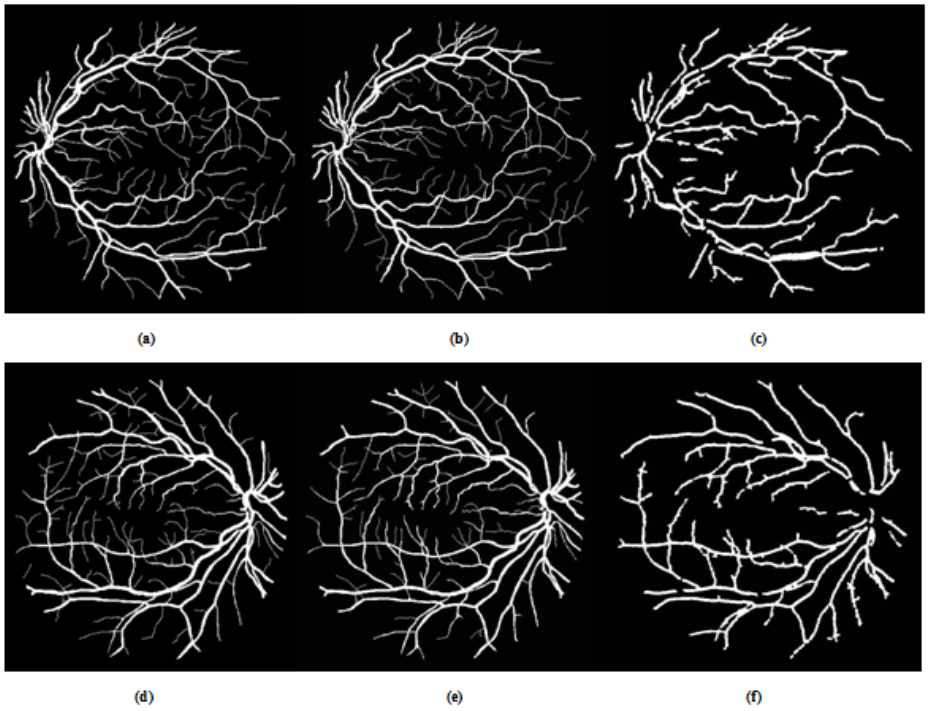

Figure 3.13: (a) & (d) DRIVE Database Ground Truth. (b) & (e) Second Human observer on DRIVE Database (c) & (f) Segmented Vessels Presented by the adaptive thresholding Presented by Jiang and Mojon [38].

window size $w*w$ as

$$U(i,j) = H(x,y) * V^1_{w*w}(x,y) \tag{3.32}$$

where *U(i,j)* is the convolved retinal image, $V^1(x,y)$ is the result obtained in *(1)* and the convolution mask *H(x,y)* is a local median filter. The enhanced image is subtracted from the convolved image to balance the illumination of the retinal image. The difference image *D(x,y)* with the balanced illumination is computed as

$$D(x,y) = U(i,j) - V^1(x,y) \tag{3.33}$$

This is followed by the computation of the adaptive thresholds based on the two texture information namely local homogeneity and energy which are further discussed

in sections 3.5.1 and 3.5.2 respectively. The segmented image is

$$S_{image}(x,y) = \begin{cases} 0, & \text{if } D(x,y) \leq T(x,y) \\ 1, & \text{otherwise} \end{cases} \tag{3.34}$$

where T(x, y) is the computed adaptive threshold. The post-processing phase described in section 3.4.3 is applied to S_{image} obtained from the adaptive thresholding techniques to remove the falsely detected vessel pixels to obtain the vessel network.

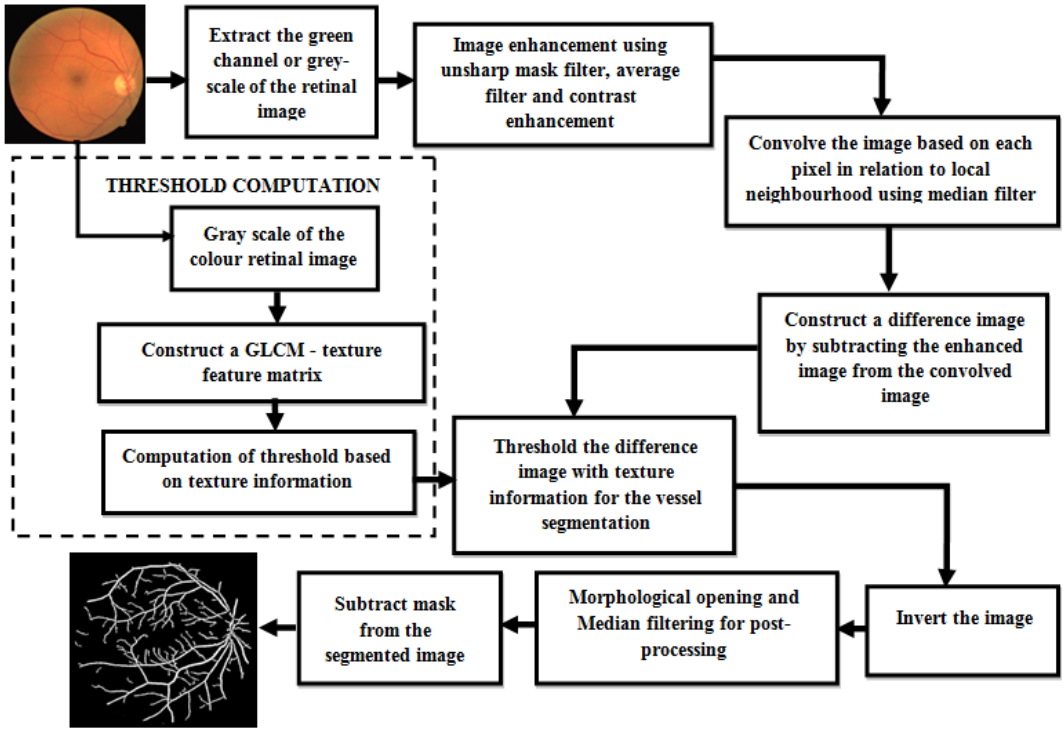

Figure 3.14: Flowchart of the Investigated Adaptive Thresholding Approach

3.5.1 Adaptive Thresholding Based on Local Homogeneity Information

Information based on inverse difference moment (that is local homogeneity) texture feature from GLCM is utilised in this adaptive thresholding technique. Inverse difference moment (IDM) is a local feature that reflects the homogeneity of a pixel in relationship with the pair pixel within distance d and relative orientation Φ. Since the width of retinal vessels can vary from very large (15 pixels) to very small (3 pixels)[47],

the multi-scale approach applied investigates the distances $(d_i)_{i=1,...,4}$ across the four orientations as it covers adequate spectrum of vessel texture information ($4 \times 4 = 16$) to compute the local threshold for each pixel of interest. The GLCM for the retinal fundus image is first computed as described in equation (3.20). The IDM feature across the varying distances, d, and relative orientation, Φ, is computed as

$$IDM = \sum_i \sum_j p_{(i,j)}/(1 + (i-j)^2) \tag{3.35}$$

where $p_{(i,j)}$ is the $(i,j)^{th}$ entry in a normalised grey scale spatial dependence matrix $C_{(i,j)}/R$, with $1/R$ the normalising factor.

3.5.1.1 Multi-Scale IDM-Feature Measurement

As the distance 'd' in a given orientation increases, there is a higher likelihood to have variation of local homogeneity measure due to the variation in the spatial relationship among neighbouring pixels. The variation of local homogeneity information within the varying distance 'd' and relative orientation 'Φ' is potentially useful in the design of an adaptive thresholding technique for image segmentation. An IDM feature matrix across different orientation and distances is formed. The IDM feature matrix, F, is defined as

$$F = \begin{pmatrix} f_{11} & f_{12} & f_{13} & f_{14} \\ f_{21} & f_{22} & f_{23} & f_{24} \\ f_{31} & f_{32} & f_{33} & f_{34} \\ f_{41} & f_{42} & f_{43} & f_{44} \end{pmatrix} \tag{3.36}$$

where $f_{ij} = IDM_{d_i,\Phi_j}$ with orientations $(\Phi_j)_{i=1,...,4}$, such that $\Phi_1 = 0^o$, $\Phi_2 = 45^o$, $\Phi_3 = 90^o$ and $\Phi_4 = 135^o$, with distances $(d_i)_{i=1,...,4}$. The range measure of F is given below as

$$Range_\Phi = Range(F) \tag{3.37}$$

such that $Range_\Phi$ is a row vector containing the range of each column of F, while the inter-quartile range is given as

$$IQR_\Phi = IQR(F) \tag{3.38}$$

such that IQR_Φ is a row vector containing the inter-quartile range of each column of matrix F. Three different threshold values are computed from each of the row vectors

above. The thresholds for the range measure are:

$$IDM_{thresh1} = 0.5(MIN(Range_{\Phi})) \tag{3.39}$$

$$IDM_{thresh2} = 0.5(MAX(Range_{\Phi})) \tag{3.40}$$

$$IDM_{thresh3} = 0.5(MEAN(Range_{\Phi})) \tag{3.41}$$

While the thresholds for the inter-quartile range measure are:

$$IDM_{thresh4} = MIN(IQR_{\Phi}) \tag{3.42}$$

$$IDM_{thresh5} = MAX(IQR_{\Phi}) \tag{3.43}$$

$$IDM_{thresh6} = MEAN(IQR_{\Phi}) \tag{3.44}$$

Figure 3.16 and Figure 3.17 show the segmented vessels obtained from the investigated local adaptive thresholding technique based on IDM information.

3.5.2 Adaptive Thresholding Based on Energy Information

Energy, which is also called angular second moment (ASM) or uniformity, is a Haralick feature that measures the textural uniformity of an image. A multi-scale approach is also applied to investigate the distances $(d_i)_{i=1,\ldots,4}$ across the four orientations as it covers adequate spectrum of vessel texture information ($4 \times 4 = 16$) to compute the local threshold for each pixel of interest. Having computed the GLCM as described in equation (3.20), the ASM feature across the varying distances, d, and relative orientation, Φ, is computed as

$$ASM = \sum_{i} \sum_{j} h(i,j)^2 \tag{3.45}$$

where $h(i,j)$ is the $(i,j)^{th}$ entry in a normalised grey-tone spatial dependence matrix $C_{(i,j)}/R$, with $1/R$ the normalising factor.

The visibility of vessels in a coloured fundus retinal image with its grey-scale intensity image and the green channel of the retinal image was previously shown in Figure

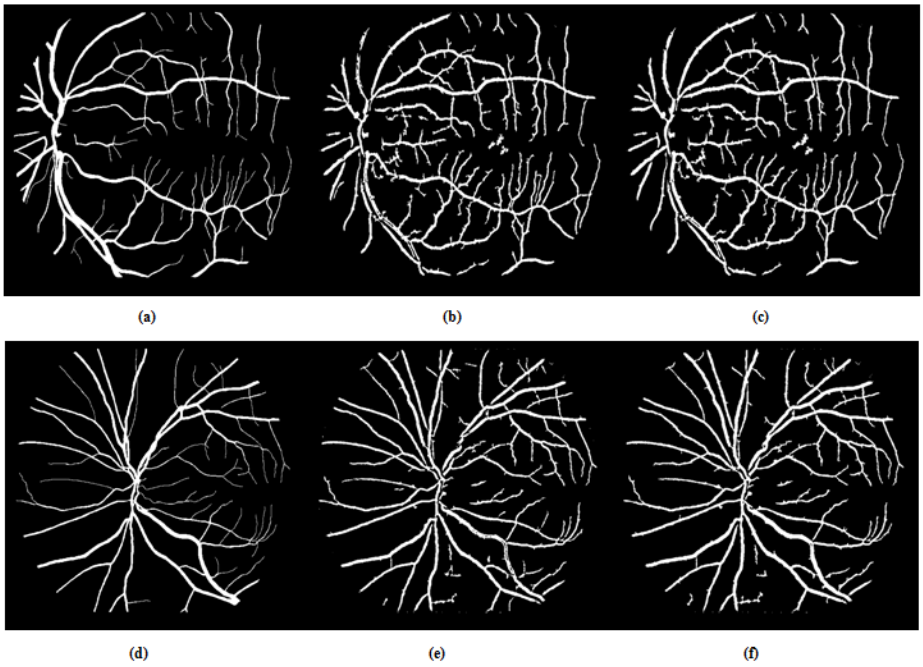

Figure 3.15: (a) & (d) STARE Database Ground Truth. (b) & (e) Segmented Vessels Using Adaptive Thresholding Technique based on ASM. (c) & (f) Segmented Vessels Using Adaptive Thresholding Technique based on IDM.

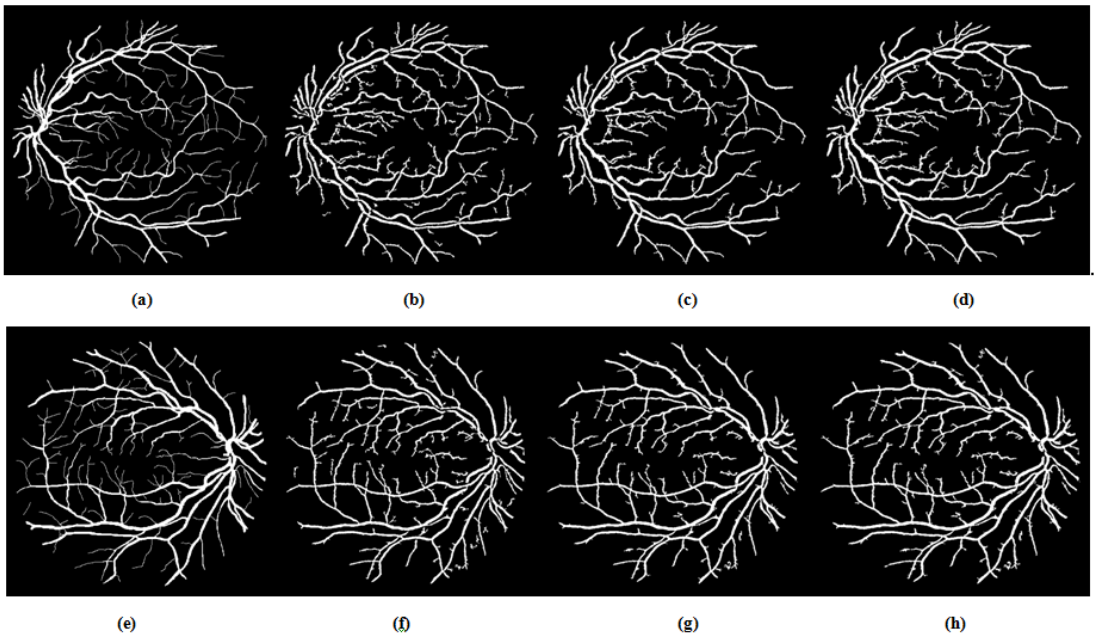

Figure 3.16: Retinal images and the segmented vessels obtained through adaptive thresholding using different IDM Interquartile range Information. Images (a) and (e) are DRIVE database gold standards. Images (b) and (f) are images segmented through adaptive thresholding using minimum IDM Interquartile range value. Images (c) and (g) are images segmented through adaptive thresholding using maximum IDM Interquartile range value. Images (d) and (h) are images segmented through adaptive thresholding using mean IDM Interquartile range value.

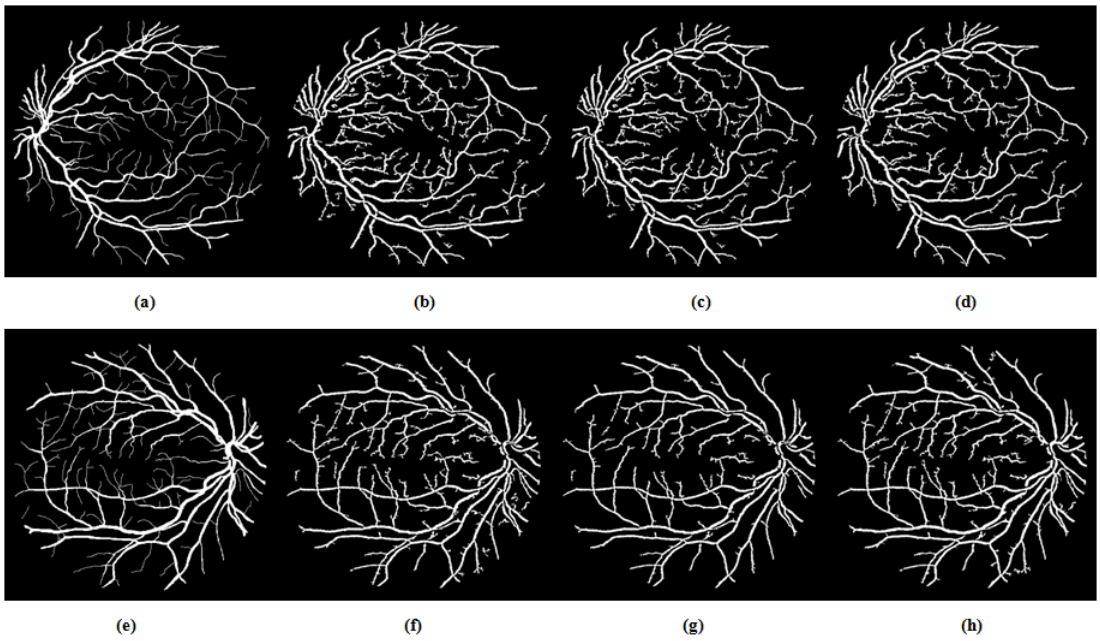

Figure 3.17: Segmented vessels obtained through adaptive thresholding using different IDM range Information. Images (a) and (e) are DRIVE database gold standards. Images (b) and (f) are images segmented through adaptive thresholding using minimum IDM range values. Images (c) and (g) are images segmented through adaptive thresholding using maximum IDM range values. Images (d) and (h) are images segmented through adaptive thresholding using mean IDM range values.

3.5. The grey level intensity and green channel of the retinal image are further investigated for the segmentation of the retinal vessels using the local adaptive thresholding technique based on ASM information investigated in this research.

3.5.2.1 Multi-Scale ASM-Feature Measurement

The variation of energy information within the varying distance 'd' and relative orientation 'Φ' is useful in the design of an adaptive thresholding technique for the vessel segmentation due to its multi-scale approach. An ASM feature matrix across different orientations and distances is computed and defined as

$$A = (a_{ij}), 1 \leq i, j \leq 4 \tag{3.46}$$

where

$$a_{ij} = ASM_{(d_i, \Phi_j)}, 1 \leq i, j \leq 4 \tag{3.47}$$

Such that $\Phi_1 = 0^o$, $\Phi_2 = 45^o$, $\Phi_3 = 90^o$ and $\Phi_4 = 135^o$, with distances $(d_i)_{i=1,\ldots,4}$. The range measure of A is given below as

$$Range_{\Phi} = Range(A) \tag{3.48}$$

Such that $Range_{\Phi}$ is a row vector containing the range of each column of A. Three different threshold values are computed from each row vector to segment the retinal vessels. The thresholds from the range measure are:

$$ASM_{thresh1} = 0.5(MIN(Range_{\Phi})) \tag{3.49}$$

$$ASM_{thresh2} = 0.5(MAX(Range_{\Phi})) \tag{3.50}$$

$$ASM_{thresh3} = 0.5(MEAN(Range_{\Phi})) \tag{3.51}$$

Figure 3.18 and Figure 3.19 show the different segmented vessels obtained from the grey-scale intensity image and the green channel of the coloured fundus image using ASM-based local adaptive thresholding technique. Figure 3.15 also visually compares the segmented vessels obtained from the two adaptive thresholding techniques investigated in this research with the ground truth on STARE database.

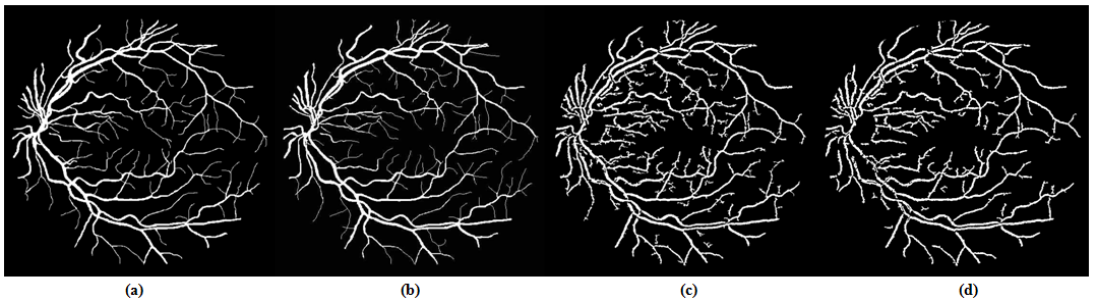

Figure 3.18: (a) DRIVE Database Gold Standard (b) Manually Segmented Vessel by the Second Human Observer on DRIVE Database (c) Segmented Vessel of the Green Channel Using ASM Range Information-Based threshold value (d) Segmented Vessel of the Grey-Scale Intensity Image Using ASM Range Information-Based threshold value.

3.6 Clustering-Based Techniques

Clustering is an unsupervised learning approach in pattern recognition that attempts to determine which pixels of image data naturally belong to the same group according to the properties of each image pixel [178]. Like other unsupervised segmentation methods, clustering techniques are not dependent on the labelled training sample. Clustering techniques are also less dependent of rigid threshold values [179]. The use of clustering techniques for the detection of vessels in retinal images without pre-processing is challenging because retinal fundus images are characterised by noise due to illumination and contrast variation. Hence, this section combines phase congruence pre-processing technique with fuzzy c-means for vessel network detection in retinal images. The combination of difference image and k-means clustering for retinal vessel network segmentation is also investigated in this section.

3.6.1 Fuzzy C-Means Combined with Phase Congruence

Fuzzy C-Means (FCM) is a soft computing-based clustering method introduced by Dunn [180]. FCM algorithm requires no hand-labeled ground truth images for training, but examines and utilises underlying patterns to classify image pixels into appropriate groups. The FCM algorithm is applied on the output image obtained from the phase congruence. The n sample of the image input data points is expressed as X = $\{x_1, x_2, ..., x_n\}$ while the corresponding cluster centres of the image data points is expressed as V = $\{v_1, v_2, ..., v_c\}$, where c is the number of clusters. μ_{ij} is the membership degree of the image data point x_i to the cluster centre v_j Fuzzy clustering computes the optimum partition based on the minimisation of the objective function given that

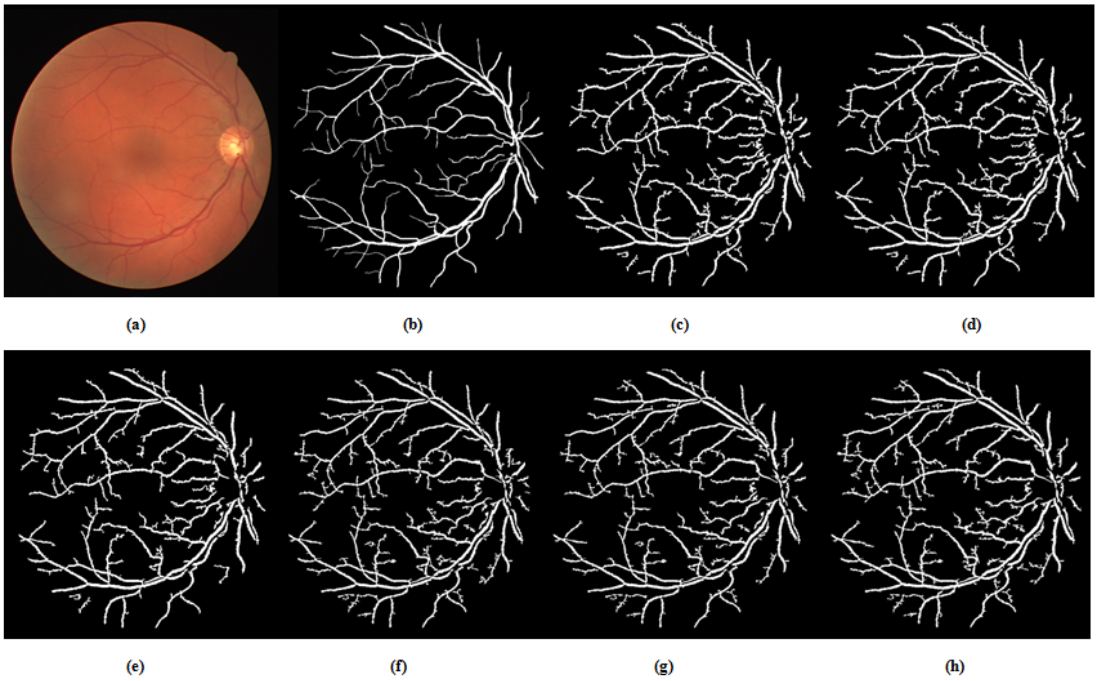

Figure 3.19: Adaptive Thresholding Using Different ASM Range Information on DRIVE database. (a) DRIVE database coloured retinal image (b) DRIVE Database Gold Standard. (c) Segmented vessel through adaptive thresholding using minimum ASM mid-range threshold value for the grey-scale intensity image. (d) Segmented vessel through adaptive thresholding using maximum ASM mid-range threshold value for the grey-scale intensity image. (e) Segmented vessel through adaptive thresholding using mean ASM mid-range threshold value for the grey-scale intensity image (f) Segmented vessel through adaptive thresholding using minimum ASM mid-range threshold value for the green channel. (g) Segmented vessel through adaptive thresholding using maximum ASM mid-range threshold value for the green channel. (h) Segmented vessel through adaptive thresholding using mean ASM mid-range threshold value for the green channel.

μ_{ij} satisfies

$$\sum_{i=1}^{n} \mu_{ij} = 1, 1 \leq j \leq n. \tag{3.52}$$

The cluster centre (i.e centroid) v_j is computed as:

$$v_j = \frac{\sum_{i=1}^{n} \mu_{ij}^m x_i}{\sum_{i=1}^{n} \mu_{ij}^m} \tag{3.53}$$

where m is the fuzziness index parameter and $m \in [1, \infty)$.
Given that:

$$d_{ij} = \| x_i - v_j \| \tag{3.54}$$

The dissimilarity between the centroids v_j and the data points x_i is computed as:

$$J_m = \sum_{i=1}^{n} \sum_{j=1}^{c} (\mu_{ij})^m d_{ij} \tag{3.55}$$

Such that d_{ij} is the Euclidean distance between the i_{th} data point and the j_{th} centroid while $\mu_{ij} \in [0, 1]$ and the fuzziness index parameter $m \in [1, \infty)$

The new membership value is further computed as:

$$\mu_{ij} = \frac{1}{\sum_{k=1}^{c} [\frac{d_{ij}}{d_{ik}}]^{\frac{2}{m-1}}} \tag{3.56}$$

This is iteratively computed until

$$\| \mu_{ij}^{(k+1)} - \mu_{ij}^{(k)} \| < \lambda \tag{3.57}$$

where k is the iteration step and $\lambda \in [0, 1]$ is the criterion for terminating the iteration.

Figure 3.20 and Figure 3.21 show the segmented vessels obtained from fuzzy c-means combined with phase congruence on DRIVE and STARE databases respectively.

3.6.2 K-Means Clustering Combined With Difference Image

K-means clustering is an unsupervised clustering technique used in defining the natural group of pixels in an image. This is achieved by classifying input image data points into different classes through a set of distances computed using the image data points and centroids. Retinal fundus images are often characterized by noise due to illumina-

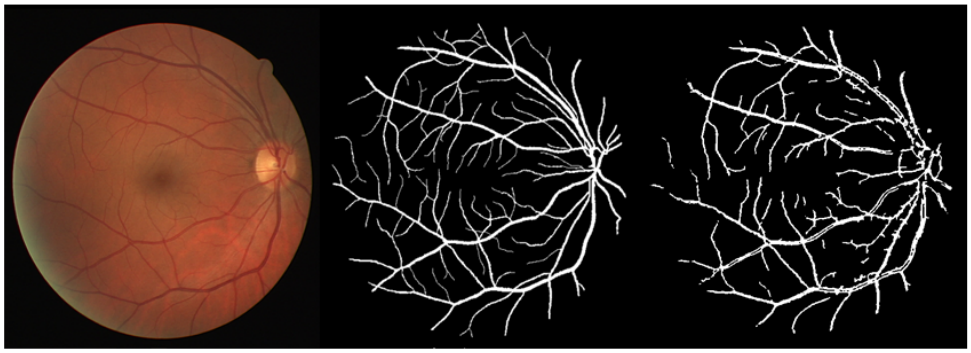

(a) (b) (c)

Figure 3.20: (a) Coloured Retinal Image (b) Drive Gold Standard (c) Fuzzy C-Means Combined with Phase Congruence

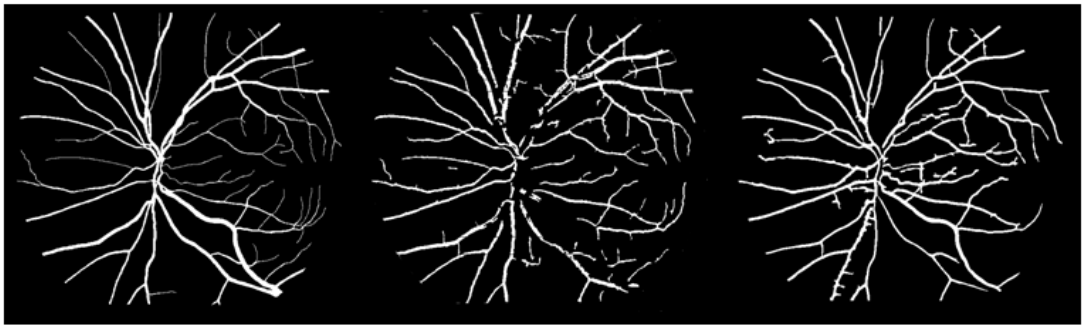

(a) (b) (c)

Figure 3.21: (a) STARE Database Ground Truth. (b) Segmented Vessels Using Fuzzy C-Means Combined with Phase Congruence. (c) Segmented Vessels Presented by Hoover et al. [21].

tion and contrast variation. Due to this, the use of k-means clustering technique for the detection of vessels in these noisy retinal images becomes challenging. In order to solve this problem, the green channel of the coloured fundus image is extracted and convolved using different filtering techniques. A difference image is generated to minimize the effect of illumination variation. The retinal vessels are then segmented by applying k-means clustering technique on the difference image. A post-processing phase that combines median filter and morphological opening is applied to remove the few remaining misclassification. A detailed discussion on the vessel segmentation method investigated in this section is further discussed in the following sections 3.6.2.1, 3.6.2.2, 3.6.2.3 and 3.6.3.

3.6.2.1 Filtering Techniques

The green channel of the retinal image is enhanced using different filtering techniques. Linear filters such as mean filter and Gaussian filter are used for smoothing images. Although these filters reduce image noise, they are weak at preserving edges in an image. Non-linear filter, particularly the median filter, is efficient at removing image noise as well as preserving edge information in images. It is, however, worth noting that the selected filter window sizes should not be too large in order to efficiently manage the noise due to illumination variation conditions of the retinal image. It is also important to carefully select the window sizes that have sufficient data points for good enhancement. For the purpose of investigation, mean, Gaussian and median filters are considered for the enhancement of the retinal image. The convolution of the retinal image is described as

$$U = H \bigotimes V \tag{3.58}$$

hence

$$U(x,y) = \sum_{(a,b)\epsilon H(x-a,y-b)\epsilon V} H(a,b)\ V(x-a,y-b) \tag{3.59}$$

where U is the convolved retinal image, V is the green channel of the retinal image and the convolution mask H is any of the filtering technique under investigation.

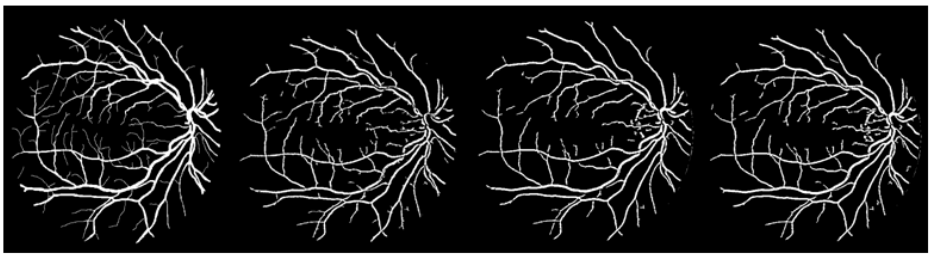

Figure 3.22: (a) DRIVE Database Gold Standard. (b) Segmented Vessels Using K-Means With DIMDF. (c) Segmented Vessels Using K-Means With DIMNF. (d) Segmented Vessels Using K-Means With DIGF.

3.6.2.2 Difference Image

A difference image is generated by subtracting the green channel of the coloured retinal image from the convolved retinal image. The difference image *D(x,y)* is given below as:

$$D(x,y) = U(x,y) - V(x,y) \tag{3.60}$$

such that D(x,y)= $\{D_\varrho(x,y), D_\upsilon(x,y), D_\sigma(x,y)\}$, where $D_\varrho(x,y)$ is the difference image based on median filter (DIMDF), $D_\upsilon(x,y)$ is the difference image based on mean filter (DIMNF) and $D_\sigma(x,y)$ is the difference image based on Gaussian filter (DIGF). A model that combines two possible difference images was also investigated. The combinations obtained are:

$$D_\upsilon^\varrho = D_\varrho(x,y) + D_\upsilon(x,y) \tag{3.61}$$

$$D_\sigma^\varrho = D_\varrho(x,y) + D_\sigma(x,y) \tag{3.62}$$

$$D_\sigma^\upsilon = D_\upsilon(x,y) + D_\sigma(x,y) \tag{3.63}$$

where D_υ^ϱ is the combination of median filter and mean filter based difference images (DIMDMNF), D_σ^ϱ is the combination of median filter and Gaussian filter based difference images (DIMDGF) and D_σ^υ is the combination of mean filter and Gaussian filter based difference images (DIMNGF). The results obtained in equations (3.60) to (3.63) are normalised to the interval [0, 255].

3.6.2.3 K-Means Clustering

K-means clustering technique is used for n sample input data points of X = $\{x_1, x_2, ..., x_n\}$ into a group of k clusters. This is achieved by considering the similarities among the input points within the same cluster as well as the differences among the different clusters. Sum of squared errors is a very useful criterion measure for clustering. Given k clusters, the sum of squared errors is computed as:

$$V = \sum_{i=1}^{k} \sum_{x_j \in S_i} ||x_j - c_i||^2 \tag{3.64}$$

such that c_i is the centroid of the i^{th} cluster S_i, for i = 1, 2, ... k.

Each of the image data points is assigned to one of the k clusters using the minimum distance principle, that is

$$d_i = \min_j ||x^{(i)} - c_i|| \tag{3.65}$$

A new centroid is computed for each cluster

$$c_i = 1/m \sum_{j=1}^{m} x_j \tag{3.66}$$

Given that $1 \leq m \leq k$.

Equations 3.65 and 3.66 are continually executed until the centroids stop changing. In such a situation, the clustering criterion $\sum_{i=1}^{k} \sum_{j=1}^{m} ||x_j - c_i||^2$ will converge.

The K-means clustering technique described in Algorithm 1 is used to segment the vessel network from the background tissue in the retinal images using the results generated from equations (3.60) to (3.63).

3.6.3 Post-Processing Phase

A combination of median filter and morphological opening as discussed in section 3.4.3 is applied for the post-processing phase.

Figure 3.22 and Figure 3.23 shows the segmented vessels obtained from k-means combined with various difference images on DRIVE database. Figure 3.24 compares the segmented vessels obtained from k-means combined with DIMDF and k-means combined with DIMDMNF with the ground truth on STARE database. Figure 3.25 compares the segmented vessels obtained from k-means combined with DIGF,DIMNF and DIMNGF on STARE database. Figure 3.26 compares the segmented vessels presented by Hoover et al. [21] and STARE database ground truth with k-means combined

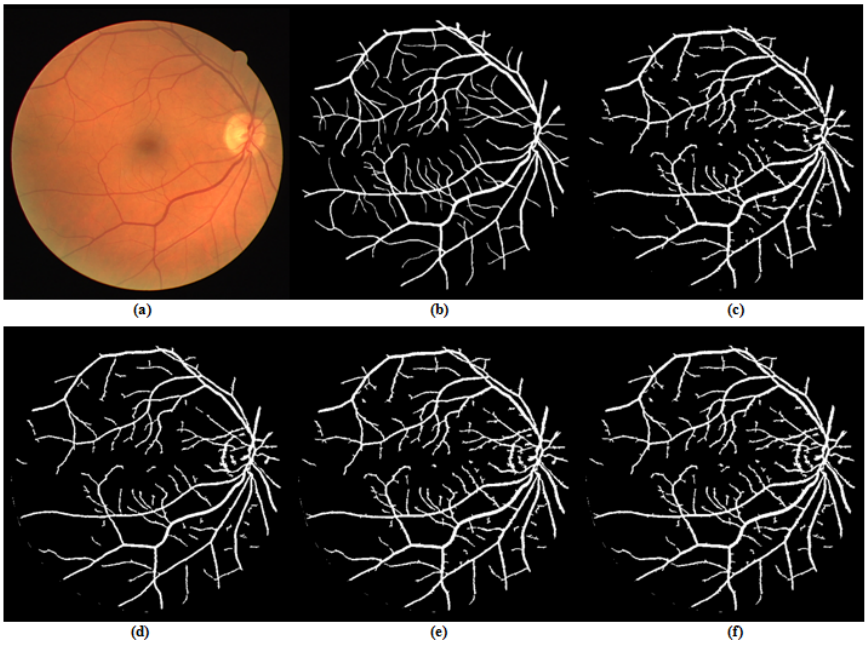

Figure 3.23: (a) DRIVE Database Coloured Fundus Image (b) DRIVE Database Gold Standard (c) Segmented Vessels Using K-Means With DIMDF (d) Segmented Vessels Using K-Means With DIMNGF (e) Segmented Vessels Using K-Means With DIMDGF (f) Segmented Vessels Using K-Means With DIMDMNF.

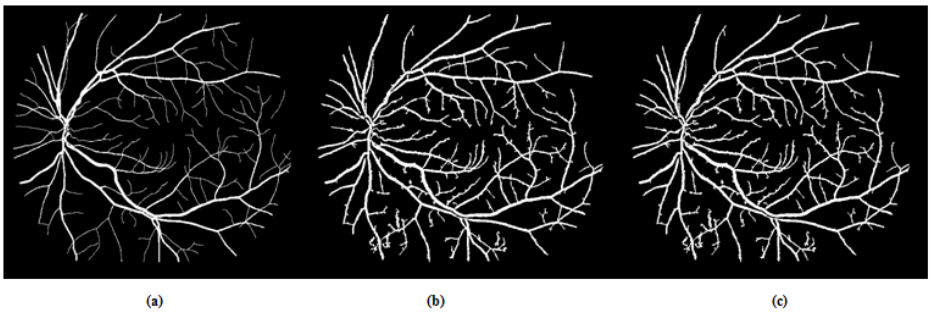

Figure 3.24: (a) STARE Database Ground Truth. (b) Segmented Vessels Using K-Means With DIMDF. (c) Segmented Vessels Using K-Means With DIMDMNF.

Algorithm 1: K-Means Algorithm

Input: Image data points of $X = \{x_1, x_2, \ldots, x_n\}$, and Number of clusters k, Limit of iterations MaxIter = 120.

Output: Segmented Image of Vessels Y = $\{y_1, y_2, \ldots, y_n\}$, where

$$l(y_i) = \begin{cases} 1, & \text{if } x_i \in V \\ 0, & \text{if } x_i \in B \end{cases}$$

for i = 1, 2, . . . , n and l(y) is the label of the pixel y, V is the set of vessel pixels and B is the set background pixels.

1 Initialize the centroids C = $\{c_1, c_2, \ldots, c_k\}$ to chosen pixels from X (It is randomly selected in our case.)
2 $iter \leftarrow 0$
3 **repeat**
  `/* Update the cluster by saving the old centroids for convergence test. */`
4 $OldCentroid \leftarrow C$
  `/* Assign labels to each datapoint based on centroids. */`
5 **for** $x_i \in X$ **do**
6 $l(x_i) \leftarrow argminDistance(x_i, c_j)\ j \in \{1.....k\}$
7 end
  `/* Assign centroids based on datapoint labels */`
8 **for** *i = 1 to k* **do**
9 c_i = Centroid(L, X, i)
10 end
11 iter ++
12 **until** *OldCentroid = C OR iter = MaxIter*

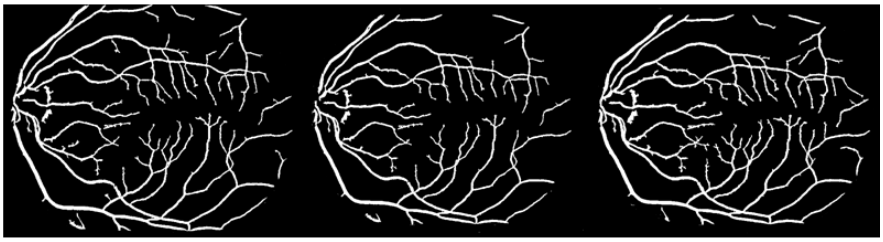

Figure 3.25: (a) Segmented Vessels Using K-Means With DIGF. (b) Segmented Vessels Using K-Means With DIMNF (c) Segmented Vessels Using K-Means With DIMNGF.

with DIMDF.

3.7 Vessel Tortousity Measurement

Retinal vessel network tortuosity is the measure of twists and curvature of a vessel [50], [59], [61],[162]. Several clinical studies have described the relation between vessel tortuosity and retinopathies such as diabetic retinopathy (DR) [156], [157], [158], [159] and retinopathy of prematurity (ROP) [49], [51], [60]. Figure 3.27 shows the variation in the directional changes, frequency of twists and the differences in the vessel lengths of the different vessels a, b, c, d, e, f and g.

3.7.1 Description of Tortuosity

With the help of ophthalmologic rules and clinical definition, metric that provides numeric index for vessel tortuosity measurement is utilised [68], [85]. Although chain code has been used for vessel tortuosity measurement in [60], it is not always accurate in areas of high curvature and may also lead to unacceptable error in the regions of low curvature [86]. Rather than inflection points alone which cannot sufficiently describe all the twists [85], this research considers the stationary points of the vessel to be very important for computing the tortuosity measure. The detection of the stationary point does not only help at checking the change of direction and twists in the vessels but also helps at detecting the straightness and non-straightness of the vessels.

The combination of arc-chord ratio [53], [54], [56], [57] with the total number of twists is used to compute tortuosity index in this research using the local tortuosity measurement approach.

The tortuosity measure applied in this research utilises the chord length, arc length and the frequency of vessel twists using the stationary points. The blood vessel is

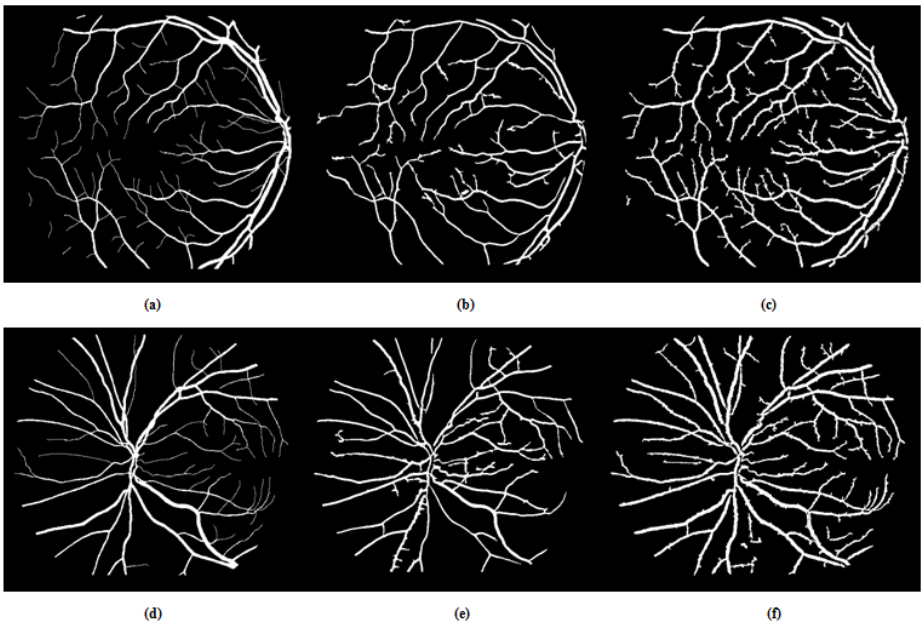

Figure 3.26: (a) & (d) STARE Database Ground Truth. (b) & (e) Segmented Vessels Presented by Hoover et al. [21]. (c) & (f) Segmented Vessels Using K-Means With DIMDGF.

skeletonised to extract the center line of the vessel.

The chord length L_{chord} of the skeletonised blood vessel is defined as

$$L_{chord} = \sqrt{(x_n - x_1)^2 + (y_n - y_1)^2} \tag{3.67}$$

where L_{chord} is the straightline connecting two points of the skeletonised blood vessel.

The arc length L_{arc} of the skeletonised blood vessel is defined as

$$L_{arc} = \sum_{i=1}^{n-1} \sqrt{(x_{i+1} - x_i)^2 + (y_{i+1} - y_i)^2} \tag{3.68}$$

where L_{arc} is the actual length of the skeletonised blood vessel.

The pixel locations of skeletonised blood vessels are extracted to plot a vessel description graph. The stationary points of the vessel description graph are computed using the gradients of the vessel description graph. The stationary points are points on the vessel description graph where the gradient is zero. There are however three major types of stationary points: minimums, maximums and inflection points as illustrated

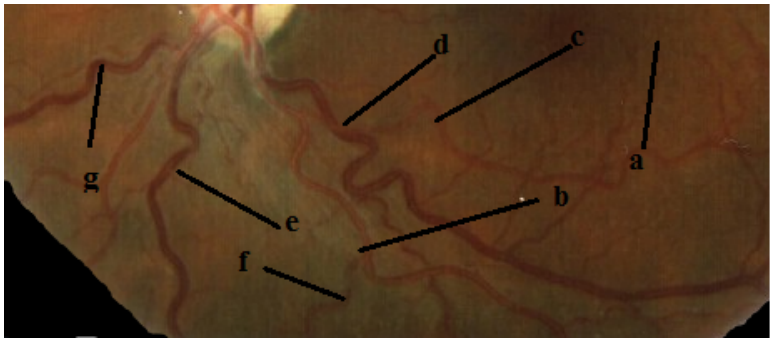

Figure 3.27: Retinal Vessels With Different Twists

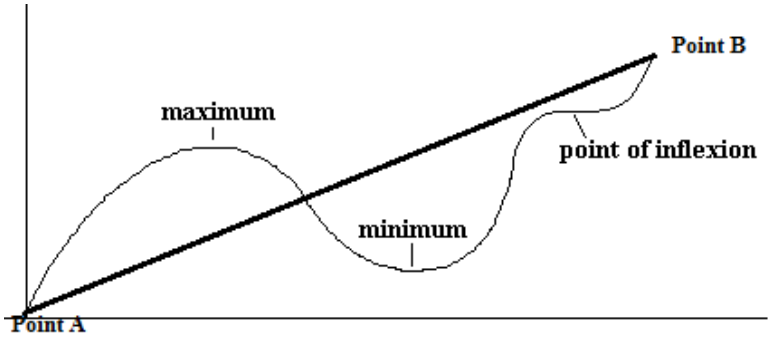

Figure 3.28: Graph Describing Different Stationary Points Between Point A & Point B .

in Figure 3.29. The detection of the stationary point does not only help in checking the change of direction and twists in the vessels but also helps in detecting the straightness and non-straightness of the vessels.

Given the skeletonised blood vessel T with vessel coordinates X and Y, the gradients of the vessel description graph are computed as:

$$G = \frac{dY}{dX} \tag{3.69}$$

such that X= $\{x_1,\ x_2,\ \ldots,\ x_n\}$, Y= $\{y_1,\ y_2,\ \ldots,\ y_n\}$, G = $\{g_1,\ g_2,\ \ldots,\ g_n\}$ and $-1 \leq G \leq 1$ where $G \epsilon \mathbb{I}$.

The nature of each type of the stationary points is shown in Figure 3.29 and Table 3.1:

The stationary points in the vessel description graph are computed using the vector of gradient obtained from equation (3.69) and the nature table in Table 3.1 as described in Algorithm 2.

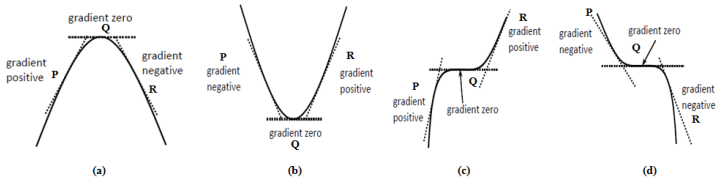

Figure 3.29: (a) Maximal Point (b) Minimal Point (c) & (d) Points of Inflection .

Table 3.1: Stationary Points Nature Table

Sign of $\frac{dy}{dx}$ at P	**Sign of $\frac{dy}{dx}$ at R**	**Graphical Behavior**	**Inference**
+	-	Figure 3.29(a)	The stationary point is a turning point corresponding to maximum (S1)
-	+	Figure 3.29(b)	The stationary point is a turning point corresponding to minimum (S2)
+	+	Figure 3.29(c)	S3: The stationary point is an inflection point (S3)
-	-	Figure 3.29(d)	S4: The stationary point is an inflection point (S4)

We investigate a normalised TI metric TI_{freq1} that combines distance metric and the vessel twist frequency obtained using the stationary points. This is computed as:

$$TI_{freq1} = \frac{SPC_{count}}{L_{chord}}((L_{arc} - L_{chord})/L_{chord}) \tag{3.70}$$

where SPC_{count} is the twist frequency of the vessel curves.

Although the previously presented distance metric [53], [54], [56], [57] divided the arc length by the chord length, a different distance metric that divides the chord length by the arc length is used for the non-normalised TI. The non-normalised TI is computed as

$$TI_{freq2} = SPC_{count}(L_{chord}/L_{arc}) \tag{3.71}$$

Algorithm 2: Vessel Twist Detection Based on Stationary Points Algorithm

Input: S1, S2, S3, S4 are the sets of stationary point detectors. T is the thinned segmented vessel.

Output: SPC_{count} is total number of vessel twists, D_i is the set of gradient pattern obtained from the detectors and E_j is the set of gradient pattern obtained from the thinned segmented vessel

```
for i ≤ 4 do
    while s ϵ S_i do
        D_i = diff(s)              // diff computes the gradient patterns
        /* Updates the computed gradient patterns of the detectors
           based on stationary points.                                  */
        UpdateDetectorPattern(D_i)
    end
end
counter ← 0          // Initialize the vessel twist counter to zero.
while t ϵ T do
    E_j = diff(t)
    /* Updates the computed gradient patterns of the segmented
       vessel.                                                          */
    UpdateRealVesselPattern(E_j) for i ≤ 4 do
        if Matches (E_j, D_i) then
            counter++          // Increments the vessel twist counter.
        end
    end
end
SPC_count ← counter
return SPC_count
```

3.8 Summary

Different segmentation approaches based on global thresholding approach, local thresholding approach and clustering have been investigated in this chapter. The segmented vessels obtained from these investigated segmentation techniques were also shown. The segmented vessels obtained from the different investigated segmentation techniques visually show that ASM-based local adaptive thresholding technique, IDM-based local adaptive thresholding technique and k-means combined with DIMDF detected more large and thin vessels while compared to the global thresholding approaches and fuzzy c-means methods.

This research investigates the use of stationary points to detect vessel twists on

vessel lines. The combination of vessel twist frequency, chord length and arc length for the computation of normalised and non-normalised tortuosity index (TI) measure is also formulated to measure the vessel tortuosity.

The next chapter shall give a detailed experimental results and discussion on the different vessel segmentation techniques and formulated TI measures investigated. Furthermore, the performances of the various methods investigated shall be compared to state of the art in the next chapter.

Chapter 4

Experimental Results and Discussions

4.1 Introduction

This chapter presents the experimental setup, results and discussions of the vessel segmentation techniques and tortuosity-measure indexes investigated in this research. A detailed discussion is done on the performance comparison of the investigated techniques with the results achieved in the literature.

4.2 Experimental Setup

The description of the system development environment and the performance evaluation measures used in the experiments are presented in this section.

4.2.1 System Development Environment

The algorithms for the vessel segmentation techniques and the vessel tortuosity measurement were implemented using MATLAB $2010a^{TM}$ on an Intel Core i5 2410M CPU (2.30 GHz, 4GB RAM).

4.2.2 Performance Evaluation Measures

The performance measures used are sensitivity, specificity and accuracy rates. The measures are described in the equations (4.1) to (4.3) below as:

$$Sensitivity = TP/(TP + FN) \tag{4.1}$$

$$Specificity = TN/(TN + FP) \tag{4.2}$$

$$Accuracy = (TP + TN)/(TP + TN + FP + FN) \tag{4.3}$$

where TP = True Positive, TN = True Negative, FP = False Positive and FN = False Negative.

An instance is said to be TP when a pixel is rightly segmented as a vessel and TN when correctly segmented as background. In related development, an instance is said to be FN if a vessel-pixel is segmented to be a background, and FP when a background pixel is segmented as a pixel in the vessel. A sensitivity measure indicates the ability of a segmentation technique to detect the pixels belonging to the vessel while a specificity measure indicates the ability of a segmentation technique to detect background pixels. The accuracy measure indicates the degree of conformity of the segmented retinal image to the ground truth.

A receiver operating characteristic (ROC) curve is a plot of the rightly classified pixels, referred to as the true positive rate (TPR) versus the fraction of the wrongly classified pixels as vessels referred to as a false positive rate (FPR). The area under the curve (AUC) is a performance measure extracted from the ROC curve.

4.2.3 Performance Assessment and Comparison

The differences between the various results achieved by the methods investigated in this thesis are assessed by means of z-test statistics [181]. The sensitivity is the proportion of the rightly detected vessel pixel while the accuracy rate is the proportion of the rightly detected pixel in the retinal image. To evaluate the variability of the performance of the different methods on the same dataset, we used the same set of data point samples. The significant difference in average sensitivity rate indicates the significant difference in the detection rate of the vessels and the significant difference in accuracy rate indicates the significant difference in the accuracy rate of the retinal vessel segmentation. Both measures are very important as good vessel segmentation

method for efficient vessel analysis in ophthalmology requires that sensitivity and accuracy rates of the segmentation be good [69]. The statistical significance of a difference between two proportions is evaluated as

$$z = \frac{\mid p_1 - p_0 \mid}{\sqrt{\bar{p}(1 - \bar{p}(\frac{1}{n_1} + \frac{1}{n_0})}} \tag{4.4}$$

where $\bar{p} = \frac{x_1+x_0}{n_1+n_0}$ with x_0 and x_1 representing the number of cases of the rightly detected pixel in the classifications of sample data-points of size n_0 and n_1 respectively. The statistically difference is computed at an asymptotic confidence level of 95% ($\alpha = 0.05$).

4.3 Experimental Results and Discussions

The results obtained from the unsupervised segmentation methods investigated in this research and the discussions of the results are presented in this section. Tables 4.2 and 4.3 show the performance of the different segmentation techniques using DRIVE and STARE databases. The computational time of the different segmentation techniques investigated in this research in comparison with the ones in the literature are shown in Table 4.1. The average time taken to process each image on DRIVE and STARE databases by ASM-based local adaptive thresholding technique and IDM-based local adaptive thresholding technique ranged from 1.9 to 3.9 seconds. K-means combined with DIMDF takes 3.4 to 4.0 to process each image on DRIVE and STARE databases. Phase congruence combined with IDM global threshold and phase congruence combined with sum entropy global threshold require 10.3 seconds to segment each image. Phase congruence combined with fuzzy C-means is the slowest of all the investigated techniques in this research with an average time of 27 seconds.

4.3.1 Global Thresholding Methods

The optimal values of the parameters used in CLAHE global thresholding were empirically selected. These parameters and their values are shown in Table 4.4.

CLAHE based global thresholding approaches on the other hand maintained high average accuracy and specificity rates across DRIVE and STARE databases. This is due to the fact that the with of segmented vessels by the approaches were highly accurate when compared with the ground truth. Although good accuracy and specificity rates were achieved, their sensitivity rates ranging from 0.6027 to 0.6729 and 0.6099 to 0.6258

Table 4.1: List of the Running Time of the Investigated Segmentation Techniques and Techniques in the Literature

Serial No.	**Technique**	**Running Time Per Image (Seconds)**	**Hardware**	**Software**
1.	Human observer [131]	7200	N/A	N/A
2.	Staal et al. [22]	900	Pentium III CPU (1.0 GHz)	Matlab
3.	Soares et al. [23]	190 (9 hours training)	P III (1.5 GHz) (512 MB RAM)	Matlab
4.	Marin et al. [28]	90	Intel Core II Duo CPU (2.13 GHz) (2 GB RAM)	Matlab
5.	Lupascu et al. [32]	125	Intel Core II Duo CPU (3.16 GHz) (3 GB RAM)	Matlab
6.	Zhang et al. [33]	10	N/A	N/A
7.	Jiang and Mojon [38]	10	Pentium III (600MHz) (3 GB RAM)	N/A
8.	Wang et al. [43]	210	Core 2 Duo (3.16 GHz) (2.0 GB RAM)	Matlab
9.	Fraz et al. [34]	37.4	N/A	Matlab
10.	Chakraborti et al [39]	8	Intel i3-2350M (2.3 GHz)	Matlab
11.	Saffarzadeh et al. [42]	7.6	Core 2 Duo (2.24 GHz) (2.0 GB RAM)	Matlab
12.	Li et al. [47]	8 & 30	N/A	N/A
13.	Amin and Yan [48]	10	Intel Pentium (2.66 GHz) (512 MB RAM)	Matlab
14.	Cinsdikici and Aydin [82]	35	N/A	N/A
15.	Yin et al. [87]	378	N/A	N/A
16.	Mendonca and Campilho [84]	150	Pentium IV (3.2 GHz) (960 MB Memory)	Matlab
17.	Miri and Mahloojifar [88]	50	N/A	N/A
18.	Xiao et al. [83]	81	N/A	N/A
19.	Otsu Thresholding Combined with CLAHE	1.8	Core i5 2410M (2.30 GHz) (4GB RAM)	Matlab
20.	ISODATA Thresholding Combined with CLAHE	1.8	””	””
21.	GLCM Sum Entropy Combined with Phase Congruence	10.3	””	””
22.	IDM thresholding Combined with Phase Congruence	10.3	””	””
23.	Adaptive Thresholding Technique Based on IDM	1.9 to 3.9	””	””
24.	Adaptive Thresholding Technique Based on ASM	1.9 to 3.9	””	””
25.	Fuzzy C-Means Combined with Phase Congruence	27.1	””	””
26.	K-means Clustering Combined with Difference Image	3.4 to 4.0	””	””

Table 4.2: Performance of Different Segmentation methods on DRIVE Database

Method	**Average Accuracy**	**Average Sensitivity**	**Average Specificity**
Human observer [131]	0.9473	0.7761	0.9725
Staal et al. [22]	0.9442	0.7345	0.9773
Niemeijer et al. [35]	0.9416	0.7145	0.9801
Zana and Klein [40]	0.9377	0.6971	0.9769
Jiang and Mojon [38]	0.9212	0.6399	0.9625
Vlachos and Dermatas [41]	0.9285	0.7468	0.9551
Wang et al. [43]	0.9461	N/A	N/A
Martinez-Perez et al [135]	0.9181	0.6389	0.9496
Szpak and Tapamo [138]	0.9299	N/A	N/A
Chaudhuri [26]	0.8773	0.3357	0.9794
Soares et al.[23]	0.9466	N/A	N/A
Akram and Khan [46]	0.9469	N/A	N/A
Mendonca et al. [84]	0.9463	0.7315	N/A
Marin et al. [28]	0.9452	N/A	N/A
Ricci and Perfetti [20]	0.9595	N/A	N/A
Xiao et al. [83]	0.9529	0.7513	0.9792
Yin et al. [87]	0.9267	0.6522	0.9710
Our Investigated CLAHE-Based Global Thresholding Techniques			
With Average Filter using Otsu	**0.9494**	**0.6535**	**0.9780**
With Gaussian Filter using Otsu	**0.9498**	**0.6729**	**0.9765**
With Average & Gaussian Filters using Otsu	**0.9427**	**0.6416**	**0.9717**
With Adaptive Filter using Otsu	**0.9368**	**0.6160**	**0.9677**
With Average Filter using ISODATA	**0.9516**	**0.6163**	**0.9780**
With Gaussian Filter using ISODATA	**0.9500**	**0.6701**	**0.9770**
With Average & Gaussian Filter using ISODATA	**0.9510**	**0.6027**	**0.9846**
With Adaptive Filter using ISODATA	**0.9521**	**0.6435**	**0.9819**
Our Investigated Phase Congruence-Based Global Thresholding Techniques			
With IDM-Based Threshold	**0.9430**	**0.7152**	**0.9650**
With GLCM Sum-Entropy	**0.9416**	**0.7026**	**0.9646**
Our Investigated Adaptive Thresholding Based on IDM			
$IDM_{thresh1}$ = **0.5**(MIN_{Range})	**0.9468**	**0.7644**	**0.9645**
$IDM_{thresh2}$ = **0.5**(MAX_{Range})	**0.9502**	**0.7612**	**0.9686**
$IDM_{thresh3}$ = **0.5**($MEAN_{Range}$)	**0.9506**	**0.7390**	**0.9711**
$IDM_{thresh4}$ = MIN_{IQR})	**0.9511**	**0.7509**	**0.9706**
$IDM_{thresh5}$ = MAX_{IQR})	**0.9532**	**0.7327**	**0.9746**
$IDM_{thresh6}$ = $MEAN_{IQR}$)	**0.9521**	**0.7454**	**0.9722**
Our Investigated Adaptive Thresholding Based on ASM			
$ASM_{thresh1}$ = **0.5**(MIN_{Range})**(Grey Intensity)**	**0.9488**	**0.7397**	**0.9691**
$ASM_{thresh2}$ = **0.5**(MAX_{Range})**(Grey Intensity)**	**0.9511**	**0.7313**	**0.9724**
$ASM_{thresh3}$ = **0.5**($MEAN_{Range}$)**(Grey Intensity)**	**0.9503**	**0.7375**	**0.9709**
$ASM_{thresh1}$ = **0.5**(MIN_{Range})**(Green Channel)**	**0.9449**	**0.7650**	**0.9623**
$ASM_{thresh2}$ = **0.5**(MAX_{Range})**(Green Channel)**	**0.9477**	**0.7560**	**0.9663**
$ASM_{thresh3}$ = **0.5**($MEAN_{Range}$)**(Green Channel)**	**0.9461**	**0.7632**	**0.9634**
Our Investigated Clustering Techniques			
With Fuzzy C-Means	**0.9431**	**0.6725**	**0.9693**
K-Means With DIMDF	**0.9556**	**0.7399**	**0.9766**
K-Means With DIMNF	**0.9555**	**0.6459**	**0.9855**
K-Means With DIGF	**0.9555**	**0.6315**	**0.9869**
K-Means With DIMDMNF	**0.9516**	**0.7581**	**0.9703**
K-Means With DIMDGF	**0.9531**	**0.7518**	**0.9726**
K-Means With DIMNGF	**0.9523**	**0.7079**	**0.9759**

Table 4.3: Performance of Different Segmentation methods on STARE Database.

Method	**Average Accuracy**	**Average Sensitivity**	**Average Specificity**
Human observer [132]	0.9354	0.8949	N/A
Hoover et al. [21]	0.9275	0.6751	0.9567
Staal [22]	0.9516	0.6970	N/A
Jiang and Mojon [38]	0.9009	N/A	N/A
Marin et al. [28]	0.9526	N/A	N/A
Ricci and Perfetti [20]	0.9584	N/A	N/A
Soares et al.[23]	0.9480	N/A	N/A
Akram and Khan [46]	0.9502	N/A	N/A
Wang et al. [43]	0.9521	N/A	N/A
Mendonca et al. [84]	0.9479	0.7123	N/A
Xiao et al. [83]	0.9476	0.7147	0.9735
Yin et al. [87]	0.9412	0.7248	0.9666
Our Investigated CLAHE-Based Global Thresholding Techniques			
With Average Filter using Otsu	**0.9409**	**0.6258**	**0.9662**
With Gaussian Filter using Otsu	**0.9435**	**0.6138**	**0.9698**
With Average & Gaussian Filters using Otsu	**0.9468**	**0.6144**	**0.9735**
With Adaptive Filter using Otsu	**0.9456**	**0.6135**	**0.9722**
With Average Filter using ISODATA	**0.9421**	**0.6238**	**0.9676**
With Gaussian Filter using ISODATA	**0.9442**	**0.6099**	**0.9709**
With Average & Gaussian Filter using ISODATA	**0.9471**	**0.6127**	**0.9740**
With Adaptive Filter using ISODATA	**0.9458**	**0.6115**	**0.9726**
Our Investigated Phase Congruence-Based Global Thresholding Techniques			
With IDM-Based Threshold	**0.9340**	**0.5202**	**0.9682**
With GLCM Sum-Entropy	**0.9318**	**0.5846**	**0.9595**
Our Investigated Adaptive Thresholding Based on IDM			
$IDM_{thresh1}$ = **0.5**(MIN_{Range})	**0.9546**	**0.7530**	**0.9710**
$IDM_{thresh2}$ = **0.5**(MAX_{Range})	**0.9550**	**0.7661**	**0.9702**
$IDM_{thresh3}$ = **0.5**($MEAN_{Range}$)	**0.9529**	**0.7613**	**0.9684**
$IDM_{thresh4}$ = MIN_{IQR})	**0.9492**	**0.7662**	**0.9642**
$IDM_{thresh5}$ = MAX_{IQR})	**0.9526**	**0.7506**	**0.9690**
$IDM_{thresh6}$ = $MEAN_{IQR}$)	**0.9511**	**0.7501**	**0.9676**
Our Investigated Adaptive Thresholding Based on ASM			
$ASM_{thresh1}$ = **0.5**(MIN_{Range})**(Grey Intensity)**	**0.9485**	**0.7458**	**0.9649**
$ASM_{thresh2}$ = **0.5**(MAX_{Range})**(Grey Intensity)**	**0.9500**	**0.7428**	**0.9668**
$ASM_{thresh3}$ = **0.5**($MEAN_{Range}$)**(Grey Intensity)**	**0.9504**	**0.7427**	**0.9672**
$ASM_{thresh1}$ = **0.5**(MIN_{Range})**(Green Channel)**	**0.9457**	**0.7542**	**0.9612**
$ASM_{thresh2}$ = **0.5**(MAX_{Range})**(Green Channel)**	**0.9500**	**0.7641**	**0.9651**
$ASM_{thresh3}$ = **0.5**($MEAN_{Range}$)**(Green Channel)**	**0.9510**	**0.7626**	**0.9657**
Our Investigated Clustering Techniques			
With Fuzzy C-Means	**0.9346**	**0.4886**	**0.9711**
K-Means With DIMDF	**0.9509**	**0.7372**	**0.9681**
K-Means With DIMNF	**0.9312**	**0.6516**	**0.9535**
K-Means With DIGF	**0.9344**	**0.6567**	**0.9564**
K-Means With DIMDMNF	**0.9492**	**0.7752**	**0.9633**
K-Means With DIMDGF	**0.9500**	**0.7666**	**0.9648**
K-Means With DIMNGF	**0.9340**	**0.6979**	**0.9526**

Table 4.4: Parameter Values For CLAHE Global Thresholding Approaches

Filtering Technique	**Filter Window size**	**CLAHE Clip-Limits**	**CLAHE Number of Tiles**
Adaptive Filter	4×4	0.05	75×75
Average Filter	3×3	0.05	75×75
Gaussian Filter (Sigma = 0.5)	3×3	0.04	75×75

on DRIVE and STARE respectively show that histogram-based global thresholding approaches are still limited to efficiently segmenting the thin vessels. They detected the large retinal vessels but failed to segment the thin vessels because the thin vessels have very low contrast and are difficult to distinguish from the background tissues using the histogram of the retinal images.

Different optimal values were empirically selected for the parameters used in phase congruency. Table 4.5 gives an overview of the parameter description and optimum parameter values of the phase congruence technique.

Table 4.5: Phase Congruence Parameter Description and Parameter Values

Parameter Description	**Parameter Symbol**	**Parameter Value (DRIVE)**	**Parameter Value (STARE)**
Number of wavelet scales.	nscale	4	3
Number of filter orientations.	norient	6	5
Wavelength of smallest scale filter.	minWaveLength	3	2.5
Scaling factor between successive filters.	mult	2.1	2.9
Ratio of the standard deviation of the Gaussian describing the log Gabor filter's transfer function in the frequency domain to the filter centre frequency.	sigmaOnf	0.55	1.5
Ratio of angular interval between filter orientations and the standard deviation of the angular Gaussian function used to construct filters in the frequency plane.	dThetaOnSigma	1.2	1.7
No of standard deviations of the noise energy beyond the mean at which we set the noise threshold point.	k	2.3	3
The fractional measure of frequency spread below which phase congruency values get penalised.	cutOff	0.5	0.5
Controls the sharpness of the transition in the sigmoid function used to weight phase congruency for frequency spread.	g	10	14

This research shows that the combination of phase congruence with IDM-based global thresholding achieved an average accuracy rate of 0.9430 and sensitivity rate of 0.7152 while phase congruence combined with GLCM sum entropy global thresholding achieved an average accuracy rate of 0.9416 and sensitivity rate of 0.7026 on DRIVE

database. Both phase congruence-based global thresholding techniques were at their best on DRIVE database. Phase congruence combined with IDM-based thresholding achieved an average accuracy rate of 0.9340 and sensitivity rate of 0.5202 while phase congruence combined with GLCM sum entropy with average accuracy rate of 0.9318 and sensitivity rate of 0.5846 on STARE database. Although the investigated inverse difference moment and sum-entropy combined with phase congruence pre-processing with average sensitivity rates 0.7152, 0.7026 and average accuracy rates 0.9416, 0.9430 improved the detection of vessels when compared with CLAHE based global thresholding with the maximum average sensitivity rate of 0.6729 and an average accuracy rate 0.9498, their lower performances on STARE are due to some undetected thin vessels and the fact that the widths of detected vessel are smaller when compared with the widths of the vessels in the ground truth. This however resulted in low sensitivity rates but relatively good accuracy rates are still maintained.

4.3.2 Local Adaptive Thresholding Methods

Different experimental study showed that the two novel local adaptive thresholding techniques based on two different Haralick texture features namely local homogeneity and energy detected both large and thin vessels. The multi-scale approach applied locally using the different texture information considering the pixel of interest in relationship with its spacial neighbourhood to compute the local adaptive threshold achieved a good vessel segmentation performance.

The use of IDM Interquartile range Information for adaptive thresholding effectively detected the majority of large and thin vessels, while a very few thinner vessels remained undetected. The false detection and other artifacts around the border of the optic disc were also reduced. Majority of the large and thin vessels are detected while a very few thinner vessels also remain undetected. The false detection around the border of the optic disc are also reduced by this technique. Adaptive thresholding technique based on IDM information was applied to vessel segmentation in [1]. Different morphological openings with line structuring elements orientated in five different directions namely 0^o, 30^o, 60^o, 120^o, 150^o and morphological reconstruction were used for the post-processing phase in [1]. Although the results presented by the adaptive thresholding technique in [1] segmented both large and thin vessels, three of the six average sensitivities and five of the six average accuracies presented in this thesis using the post-processing technique described in section 3.4.3 improved with significant differences when compared with the technique in [1].

Although all the threshold values of the adaptive thresholding technique based on IDM information in this thesis achieved good results, the results obtained shows that adaptive thresholding using maximum IDM range information achieved higher average sensitivity rates of 0.7612 and 0.7661 while maintaining high average accuracy rates of 0.9502 and 0.9550 on DRIVE and STARE databases respectively. When compared with the average sensitivity rates of the other adaptive thresholding using IDM information, adaptive thresholding using maximum IDM range information improved with significant differences on DRIVE and STARE databases. Minimum average accuracy rates of 0.9468 and 0.9492 with minimum average sensitivity rates of 0.7327 and 0.7501 were achieved by the adaptive thresholding technique based on IDM information on DRIVE and STARE respectively. The time required to segment each retinal image using this technique ranged from 1.9 to 3.9 seconds.

The AUC value of 0.9722 achieved by adaptive thresholding technique based on maximum IDM range information is significantly higher when compared with the AUC rates 0.9682, 0.9699, 0.9705, 0.9707 and 0.9713 of the other adaptive thresholding techniques based IDM information on DRIVE database. The maximum AUC value 0.9824 of the adaptive thresholding technique based on minimum IDM range information is higher when compared with the AUC values 0.9642, 0.9705, 0.9741 of the three adaptive thresholding techniques based on IDM IQR information with significant differences on STARE database. The maximum AUC value 0.9824 of the adaptive thresholding technique based on minimum IDM range information when compared with the AUC rates 0.9818 and 0.9819 of the other IDM range information-based thresholding techniques achieved slight significant differences.

Different segmentation results were obtained through adaptive thresholding using different GLCM-energy (ASM) range information for both the green channel of the coloured retinal image and the grey-scale of the coloured retinal image. The use of ASM Information for adaptive thresholding effectively detected majority of the large and thin vessels, while a very few thinner vessels remained undetected. The false detection and other artefact around the border of the optic disc were also reduced.

The results obtained showed that adaptive thresholding based on ASM range information using the green channel achieved the highest average sensitivity rates of 0.7632 and 0.7641 with improved significant differences when compared with the other adaptive thresholding based on ASM information using the grey-scale of the retinal images on DRIVE and STARE databases respectively. The average accuracy rate 0.9510 achieved by the average sensitivity rate 0.7641 is significantly higher when compared with the average accuracy rates of four adaptive thresholding based on ASM informa-

tion on STARE database. The average accuracy rate 0.9461 achieved by the average sensitivity rate 0.7632 is however not higher when compared with the average accuracy rates of the other adaptive thresholding based on ASM information on DRIVE database. A minimum average sensitivity rates of 0.7313 and 0.7427 were achieved by the adaptive thresholding technique based on ASM information using grey-scale on DRIVE and STARE respectively. The time taken to segment each retinal image using this technique ranged from 1.9 to 3.9 seconds.

A maximum AUC value of 0.9711 achieved by the adaptive thresholding technique based on maximum ASM range information of grey level intensity image is higher when compared with all the AUC rates 0.9656, 0.9698, 0.9634, 0.9680 and 0.9658 of the other adaptive thresholding technique based on ASM information with significant differences on DRIVE database. The maximum AUC value of 0.9782 achieved on STARE database by the adaptive thresholding technique based on maximum ASM range information on green channel of the retinal image is significantly higher when compared with four AUC rates 0.9671, 0.9681, 0.9695 and 0.9745 of the other adaptive thresholding technique based on ASM information on STARE database.

Empirically, we established that window sizes ranging from (11×11) to (17×17) covered adequate spectrum that effectively minimised illumination variation while using the adaptive thresholding techniques for the segmentation of the retinal vessels. There was however a higher amount of noise and an increase in the computational time when the the window size was too large (that is, larger than 17×17). In such a situation, the further post processing for removal of noise led to the removal of the thin vessels as well as some large vessels. In a related development, there is a possibility of insufficient data when the window size is too small (that is, lesser than 11×11). This leads to the loss of some large and thin vessels during segmentation.

4.3.3 Clustering Methods

Phase congruence combined with fuzzy c-mean was the slowest of all the investigated techniques in this research with an average time of 27.1 seconds. The computational complexity of this technique was due to the iterative nature of fuzzy c-means. Keeping the number of data points for each retinal image constant to n = 226907 image pixels for DRIVE database and 357500 image pixels for STARE database, the number of cluster c was set to 2, and the maximum number of iterations i was set to 120. The value of the criterion for terminating the iteration was set to $\lambda = 0.0001$. Although phase congruence combined with fuzzy c-means was at its best on DRIVE database

with an average accuracy rate of 0.9431 and an average sensitivity rate of 0.6725, its performance on STARE database showed a lower average accuracy rate of 0.9346 and an average sensitivity rate of 0.4886. Just like the other phase congruence based techniques previously discussed, the lower average sensitivity and average accurate rates achieved by phase congruence combined with fuzzy c-mean were also due to the reduced-vessel width detection and some undetected thin vessels. This segmentation technique may, however, be unsuitable for situations where vessel width measurement and thinner vessels in retinal images are of great importance. Another limitation of phase congruence based techniques investigated in this research was the false vessel detection and other artefact around the border of the optic disc.

Different low pass filters such as median, mean and Gaussian filters were applied to smoothen and compute various difference images. This research established that in order to achieve a good vessel segmentation using difference images combined with k-means clustering technique, a difference image where the vessel details of the retinal image were preserved was required. Experimental study showed that median filter yields the best difference image that preserves the vessel details. K-means clustering technique combined with DIMDF achieved average accuracy rates of 0.9556 and 0.9509 and average sensitivity rates of 0.7399 and 0.7372 on DRIVE and STARE respectively. K-means with DIMNF achieved average accuracy rates of 0.9555 and 0.9312 and average sensitivity rates of 0.6459 and 0.6516 on DRIVE and STARE respectively. There are significant improvements in the average sensitivity rates obtained from k-means with DIMDF when compared with the average sensitivity rates of k-means with DIMNF on both DRIVE and STARE databases. On STARE database, there is a significant improvement in the accuracy rate obtained from k-means with DIMDF when compared with k-means with DIMNF. K-means with DIGF also achieved a lower segmentation performance with average accuracy rates of 0.9555 and 0.9344 and average sensitivity rates of 0.6315 and 0.6567 when compared with k-means combined with DIMDF. The average sensitivity rates obtained from k-means with DIMDF significantly improved when compared with the average the sensitivity rates of k-means with DIGF on both DRIVE and STARE databases. The average accuracy rate obtained from k-means with DIMDF also improved significantly when compared with k-means with DIGF on STARE database.

DIMDF combined with k-means clustering detected majority of the large and thin vessels, while a very few thinner vessels remained undetected. The false detection around the border of the optic disc while applying DIMDF combined with k-means clustering were fewer when compared with DIMNF and DIGF combined with k-means

clustering. This is due to the fact that the median filter preserved edge information of the vessels and effectively minimized the image noise during the enhancement of the retinal image.

K-means combined with DIMDF achieved significantly higher AUC of 0.9735 and 0.9756 when compared with k-means combined with DIMNF (0.9615, 0.9426) and k-means combined with DIGF (0.9610, 0.9454) on DRIVE and STARE respectively. Furthermore, experimental study showed that the linear combination of the median filter based difference images with Gaussian and mean filter based difference images respectively while combined with k-means clustering technique led to the detection of more thinner vessels. The results obtained from vessels segmented using DIMDF DIMDMNF, DIMDGF and DIMNGF while combined with k-means clustering technique showed that majority of large and thin vessels were detected while a very few thinner vessels still remained undetected. The results obtained by the combination of DIMDMNF, DIMDGF and DIMNGF with k-means clustering produced a higher false detection around the border of the optic disc when compared with the results obtained from the combination of k-means and DIMDF. The average sensitivity rates of 0.7581 and 0.7752 were achieved by DIMDMNF combined with k-means clustering while DIMDGF combined with k-means clustering achieved average sensitivity rates of 0.7518 and 0.7666 on DRIVE and STARE databases respectively. When compared with each other, the average sensitivities of DIMDMNF combined with k-means clustering slightly improved when compared with DIMDGF combined with k-means on DRIVE and STARE databases with significant differences. The average sensitivities of DIMDMNF combined with k-means clustering (0.7581, 0.7752) and DIMDGF combined with k-means (0.7518, 0.7666) improved when compared with average sensitivities of DIMDF combined with k-means (0.7399, 0.7372) on both DRIVE and STARE databases with significant differences. These improved significant differences in the segmentation performances are due the linear combination with DIMDF. The time required to segment each retinal image using this technique ranged from 3.4 to 4.0 seconds on DRIVE and STARE databases.

K-means combined with DIMDGF achieved AUC rates 0.9758 and 0.9734 while k-means combined with DIMDMNF achieved AUC rates of 0.9749 and 0.9728, and k-means combined with DIMNGF achieved AUC rates of 0.9719 and 0.9734 on DRIVE and STARE respectively. A higher AUC rate 0.9758 obtained from DIMDGF combined with k-means showed improvement in the detection of vessels when compared with the AUC rates 0.9749, 0.9735 and 0.9719 of DIMDMNF, DIMDF and DIMNGF respectively combined with k-means clustering on DRIVE database with significant differences.

The higher AUC rate 0.9756 obtained from DIMDF combined with k-means showed improvement in the detection of vessels when compared with the AUC rates 0.9734, 0.9728 and 0.9463 of DIMDGF, DIMDMNF and DIMNGF combined with k-means clustering respectively on STARE database with significant differences.

4.3.4 Proposed Vessel Segmentation Methods

K-means clustering combined with difference image based on median filtering achieved average sensitivity rates of 0.7399, 0.7518 and 0.7581 on DRIVE and average sensitivity rates of 0.7372, 0.7666 and 0.7752 on STARE and average accuracy rates of 0.9556, 0.9531 and 0.9516 on DRIVE and average accuracy rates of 0.9509, 0.9500 and 0.9492 on STARE. The two local adaptive thresholding techniques achieved minimum average sensitivity rate of 0.7313 with maximum average sensitivity rate of 0.7650 on DRIVE and minimum average sensitivity rate of 0.7427 with maximum average sensitivity rate of 0.7661 on STARE. The two local adaptive thresholding techniques achieved a minimum average accuracy rate of 0.9449 and a maximum average accuracy rate of 0.9532 on DRIVE database. The two local adaptive thresholding techniques also achieved a minimum average accuracy rate of 0.9457 and a maximum average accuracy rate of 0.9550 on STARE database. The global thresholding techniques and fuzzy c-means achieved average sensitivity rates ranging from 0.6027 to 0.7152 on DRIVE with 0.4886 to 0.6258 on STARE and average accuracy rates ranging from 0.9368 to 0.9521 on DRIVE with 0.9318 to 0.9471 on STARE respectively.

K-means clustering combined with difference image based on median filtering and the two local adaptive thresholding techniques are the best of all the vessel segmentation techniques investigated as they outperformed the global thresholding techniques and fuzzy c-means on DRIVE and STARE databases for the detection of more vessels in the retinal images with significant differences. This was demonstrated as their sensitivity rates indicating the rate of the detection of vessels significant outperformed the sensitivity rates of these global thresholding techniques and fuzzy c-means on DRIVE and STARE databases. Although the accuracy rates of these segmentation techniques were considered, the sensitivity rates were considered first since they (that is, sensitivity rates) indicated the rate of the vessel detection. K-means clustering combined with difference image based on median filtering and the two local adaptive thresholding techniques are computationally fast (1.9 to 4.0 seconds), robust for the segmentation of both large and thin retinal vessels, and also reduce the false detection of vessels around the border of the optic disc. We hereby propose k-means clustering combined

with difference image based on median filtering and the two local adaptive thresholding techniques based on their improved performances as demonstrated by their higher average sensitivity, average accuracy and very good specificity rates when compared with other investigated techniques as shown in Tables 4.2 and 4.3.

4.4 Comparison With Existing Segmentation Methods

The performance measures of the different previously proposed techniques on DRIVE and STARE databases are compared with all the investigated techniques in Tables 4.2 and 4.3. The best performing methods of the proposed methods presented higher average sensitivity rates, average accuracy rates and AUC values when compared with the average sensitivity rates, average accuracy rates and AUC values of the previous techniques in the literature. Although the work of Ricci and Perfetti [20] presented no average sensitivity rate and yielded a higher accuracy rate when compared with the proposed methods, it presented a significantly lower AUC value when compared with the AUC values of the best performing methods of the proposed methods.

Figure 4.1 gives a visual description that compares the results obtained from some vessel segmentation techniques in the literature. The method proposed by Ricci and Perfetti [20] achieved the segmentation of large and part of the thinner vessels but has a very high false detection around the border of the optic disc.

It can be observed that Jiang and Mojon [38] were unable to segment the thin vessel as some large vessels. Although Martinez-Perez et al. [182] had a good segmentation performance, they achieved a very high false detection around the border of the optic disc and failed to segment the thin vessels. In a related development, supervised segmentation techniques by Niemeijer [35], Staal [22] and Soares et al.[23] segmented the large and most of the thinner vessels. The segmented vessels obtained in the two proposed local adaptive thresholding techniques and k-means combined with DIMDF improved by reducing the false detection around the border of the optic disc and also segmented both large and part of the thinner vessels.

4.4.1 Global Thresholding Approaches on DRIVE Database

The global thresholding techniques achieved average sensitivity rates ranging from 0.6027 to 0.7152 with average accuracy rates ranging from 0.9368 to 0.9521 on DRIVE database. The method presented by Chaudhuri et al. [26] achieved a significantly lower average accuracy rate of 0.8773 and a significantly lower average sensitivity rate

Table 4.6: Comparison of Proposed Techniques with Previous Works on DRIVE

Method	**Avg. Sens.**	**Avg. Acc.**	**AUC**
Staal [22]	0.7345	0.9442	0.9520
Niemeijer [35]	0.7145	0.9416	0.9294
Zana and Klein [40]	0.6971	0.9377	0.8984
Jiang and Mojon [38]	0.6399	0.9212	0.9114
Wang et al. [43]	N/A	0.9461	0.9543
Chaudhuri [26]	0.3357	0.8773	0.7878
Soares et al.[23]	N/A	0.9466	0.9614
Akram and Khan [46]	N/A	0.9469	0.963
Marin et al. [28]	N/A	0.9452	0.9588
Ricci and Perfetti [20]	N/A	0.9595	0.9558
Proposed Adaptive Thresholding Based on IDM			
$IDM_{thresh1} = 0.5(MIN_{Range})$	0.7644	0.9468	0.9682
$IDM_{thresh2} = 0.5(MAX_{Range})$	0.7612	0.9502	0.9707
$IDM_{thresh3} = 0.5(MEAN_{Range})$	0.7390	0.9506	0.9699
$IDM_{thresh4} = MIN_{IQR})$	0.7509	0.9511	0.9713
$IDM_{thresh5} = MAX_{IQR})$	0.7327	0.9532	0.9722
$IDM_{thresh6} = MEAN_{IQR})$	0.7454	0.9521	0.9705
Proposed Adaptive Thresholding Based on ASM			
$ASM_{thresh1} = 0.5(MIN_{Range})$(Grey Intensity)	0.7397	0.9488	0.9656
$ASM_{thresh2} = 0.5(MAX_{Range})$(Grey Intensity)	0.7313	0.9511	0.9711
$ASM_{thresh3} = 0.5(MEAN_{Range})$(Grey Intensity)	0.7375	0.9503	0.9698
$ASM_{thresh1} = 0.5(MIN_{Range})$(Green Channel)	0.7650	0.9449	0.9634
$ASM_{thresh2} = 0.5(MAX_{Range})$(Green Channel)	0.7560	0.9477	0.9680
$ASM_{thresh3} = 0.5(MEAN_{Range})$(Green Channel)	0.7632	0.9461	0.9658
Proposed K-Means Clustering Techniques			
K-Means With DIMDF	0.7399	0.9556	0.9735
K-Means With DIMNF	0.6459	0.9555	0.9615
K-Means With DIGF	0.6315	0.9555	0.9610
K-Means With DIMDMNF	0.7581	0.9516	0.9749
K-Means With DIMDGF	0.7518	0.9531	0.9758
K-Means With DIMNGF	0.7079	0.9523	0.9719

Table 4.7: Comparison of Proposed Techniques with Previous Works on STARE

Method	**Avg. Sens.**	**Avg. Acc.**	**AUC**
Staal [22]	0.6970	0.9516	0.9614
Jiang and Mojon [38]	N/A	0.9009	0.929
Wang et al. [43]	N/A	0.9521	0.9682
Soares et al.[23]	N/A	0.9480	0.9671
Akram and Khan [46]	N/A	0.9502	0.970
Marin et al. [28]	N/A	0.9526	0.9769
Ricci and Perfetti [20]	N/A	0.9584	0.9602
Proposed Adaptive Thresholding Based on IDM			
$IDM_{thresh1} = 0.5(MIN_{Range})$	0.7530	0.9546	0.9824
$IDM_{thresh2} = 0.5(MAX_{Range})$	0.7661	0.9550	0.9818
$IDM_{thresh3} = 0.5(MEAN_{Range})$	0.7613	0.9529	0.9819
$IDM_{thresh4} = MIN_{IQR})$	0.7662	0.9492	0.9642
$IDM_{thresh5} = MAX_{IQR})$	0.7506	0.9526	0.9741
$IDM_{thresh6} = MEAN_{IQR})$	0.7501	0.9511	0.9705
Proposed Adaptive Thresholding Based on ASM			
$ASM_{thresh1} = 0.5(MIN_{Range})$(Grey Intensity)	0.7458	0.9485	0.9695
$ASM_{thresh2} = 0.5(MAX_{Range})$(Grey Intensity)	0.7428	0.9500	0.9681
$ASM_{thresh3} = 0.5(MEAN_{Range})$(Grey Intensity)	0.7427	0.9504	0.9745
$ASM_{thresh1} = 0.5(MIN_{Range})$(Green Channel)	0.7542	0.9457	0.9671
$ASM_{thresh2} = 0.5(MAX_{Range})$(Green Channel)	0.7641	0.9500	0.9782
$ASM_{thresh3} = 0.5(MEAN_{Range})$(Green Channel)	0.7626	0.9510	0.9781
Proposed K-Means Clustering Techniques			
K-Means With DIMDF	0.7372	0.9509	0.9756
K-Means With DIMNF	0.6516	0.9312	0.9426
K-Means With DIGF	0.6567	0.9344	0.9454
K-Means With DIMDMNF	0.7752	0.9492	0.9728
K-Means With DIMDGF	0.7666	0.9500	0.9734
K-Means With DIMNGF	0.6979	0.9340	0.9463

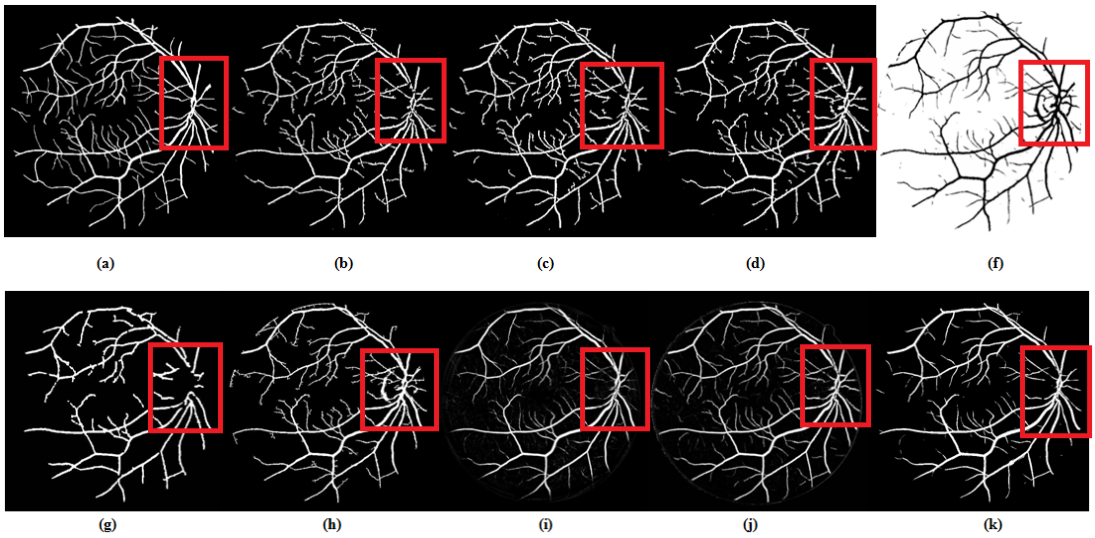

Figure 4.1: (a) DRIVE Gold Standard (b)Local Adaptive Threshold Using Local Homogeneity information (c)Local Adaptive Threshold Using Energy information (d)Result obtained from the proposed K-means combined with DIMDF (e)Result obtained in Ricci and Perfetti [20] (f) Result obtained by Jiang & Mojon [38] (g) Result obtained in Martinez-Perez et al. [182] (h) Result obtained in Niemeijer [35] (i) Result obtained in Staal [22] (j) Result obtained in Soares et al.[23].

of 0.3357 when compared with all the global thresholding methods investigated in this research. The work of Jiang and Mojon [38] also achieved significantly lower average accuracy rates of 0.9212 and 0.9009 when compared with all the different global thresholding-based approaches presented in this thesis. Five of the global thresholding techniques with average sensitivity rates 0.6535, 0.6729, 0.6701, 0.7026 and 0.7152 significantly outperformed the average sensitivity rate of 0.6399 presented by Jiang and Mojon [38] on DRIVE database. Although Niemeijer et al [35] presented a lower average sensitivity rate of 0.7145 and an average accuracy rate of 0.9416 when compared with the maximum average sensitivity rate of 0.7152 and its corresponding average accuracy rate of 0.9430 obtained from the global thresholding approaches presented in this thesis, there was no significant difference. Although seven average sensitivity rates of 0.6416, 0.6435, 0.6535, 0.6701, 0.6729, 0.7026 and 0.7152 with their corresponding average accuracy rates of 0.9427, 0.9521, 0.9494, 0.9500, 0.9498, 0.9416 and 0.9430 respectively achieved by the global thresholding approaches presented higher values when compared with the average sensitivity rate of 0.6389 and 0.9181 achieved by Martinez-Perez et al. [135], only five of the presented approaches improved performances with significant differences. Staal et al. [22] presented a higher average sensitivity rate of

0.7345 when compared with all the average sensitivity rates of the global thresholding approaches. Marin et al. [28] and Soares et al.[23] present a higher average accuracy rates of 0.9452 and 0.9466 respectively when compared with six of the average accuracy rates obtained through the global thresholding approaches presented in this thesis. Two average sensitivity rates of 0.7026 and 0.7152 with their corresponding average accuracy rates of 0.9416 and 0.9430 respectively presented slightly significant improvement in the detection of vessels when compared with the average sensitivity rate of 0.6971 and average accuracy rate of 0.9377 achieved by Zana and Klein [40]. The human observer presented a significantly higher average sensitivity rate of 0.7761 when compared with all the average sensitivity rates of the global thresholding approaches ranging from 0.6027 to 0.7152. The higher detection rate of both large and thin vessels by the human observer [131] resulted in the higher average sensitivity rate achieved by the human observer [131].

4.4.2 Global Thresholding Approaches on STARE Database

The global thresholding techniques achieved average sensitivity rates ranging from 0.5202 to 0.6258 with average accuracy rates ranging from 0.9318 to 0.9471 on STARE database. Hoover et al. [21] presented a lower average accuracy rate of 0.9275 but a higher average sensitivity rate of 0.6751 when compared with all the global thresholding-based approaches investigated in this research. All the global thresholding-based approaches investigated in this thesis achieved significantly higher accuracy rates ranging from 0.9318 to 0.9471 when compared with the work of Jiang and Mojon [38] with average accuracy rate of 0.9009. Staal et al. [22], Mendonca et al. [84] and Xiao et al. [83] presented significantly higher average sensitivity rates of 0.6970, 0.7123, 0.7147 and corresponding average accuracy rates of 0.9516, 0.9479, 0.9476 when compared with all the average sensitivity rates of the global thresholding approaches presented in this thesis ranging from 0.5202 to 0.6258 with average accuracy rates ranging from 0.9318 to 0.9471. Akram and Khan [46], Marin et al. [28], Ricci and Perfetti [20], Soares et al.[23] and Wang et al. [43] presented significantly higher average accuracies rates of 0.9502, 0.9526, 0.9584, 0.9480 and 0.9521 respectively when compared with the average accuracy rates of all the global thresholding-based approaches presented in this thesis. Yin et al. [87] presented a significantly higher average sensitivity rate of 0.7248 when compared with the average sensitivity rates of all the global thresholding approaches presented in this thesis ranging from 0.5202 to 0.6258. The human observer [132] presented a significantly higher average sensitivity rate of 0.8949 when compared with all

the average sensitivities of the global thresholding approaches. The higher detection rate of both large and thin vessels by the human observer [132] resulted in the higher average sensitivity rate achieved by the human observer [132].

Although all the CLAHE-based global thresholding techniques and all the phase congruence-based global thresholding techniques are computationally faster when compared with the techniques presented in [22], [23], [28], [43], [83], [84], the computing environment are different. All the CLAHE-based global thresholding techniques and the phase congruence-based global thresholding techniques are computationally faster when compared with the human observer [131] 4000 times and 699.03 times respectively.

4.4.3 Adaptive Thresholding Techniques on DRIVE Database

The adaptive thresholding using different IDM information techniques investigated achieved average sensitivity rates of 0.7327, 0.7390, 0.7454, 0.7509, 0.7612 and 0.7644 with corresponding average accuracy rates of 0.9532, 0.9506, 0.9521, 0.9511, 0.9502 and 0.9468 respectively on DRIVE database. All the adaptive thresholding using different IDM information techniques presented significantly higher average sensitivity rates of 0.7327, 0.7390, 0.7454, 0.7509, 0.7612 and 0.7644 with significantly higher average accuracy rates of 0.9532, 0.9506, 0.9521, 0.9511, 0.9502 and 0.9468 when compared with Chaudhuri et al. [26], Jiang and Mojon [38], Zana and Klein [40], Martinez-Perez et al. [135], Niemeijer et al [35] and Yin et al. [87] with average sensitivity rates of 0.3357, 0.6399, 0.6971, 0.6389, 0.7145 and 0.6522 with their corresponding average accuracy rates of 0.8773, 0.9212, 0.9377, 0.9181, 0.9416 and 0.9267 respectively.

Five of the six adaptive thresholding techniques using different IDM information presented significantly higher average accuracy rates of 0.9532, 0.9506, 0.9521, 0.9511 and 0.9502 when compared with average accuracy rates of 0.9469, 0.9452, 0.9466, 0.9299 and 0.9461 achieved by Akram and Khan [46], Marin et al. [28], Soares et al.[23], Szpak and Tapamo [138] and Wang et al. [43] respectively. Three of the six adaptive thresholding techniques using different IDM information presented significantly higher average sensitivity rates of 0.7509, 0.7612 and 0.7644 when compared with the average sensitivity rate of 0.7468 achieved by Vlachos and Dermatas [41]. All the adaptive thresholding techniques using different IDM information presented significantly higher average accuracy rates of 0.9532, 0.9506, 0.9521, 0.9511, 0.9502 and 0.9468 when compared with the average accuracy rate of 0.9285 achieved by Vlachos and Dermatas [41]. Four of the six adaptive thresholding techniques using different IDM information presented significantly higher average sensitivity rates of 0.7454, 0.7509, 0.7612 and 0.7644

when compared with Mendonca et al. [84] and Staal et al. [22] with average sensitivity rates of 0.7315 and 0.7345. Five of the six adaptive thresholding techniques using different IDM information presented significantly higher average accuracy rates of 0.9532, 0.9506, 0.9521, 0.9511 and 0.9502 when compared with Mendonca et al. [84] and Staal et al. [22] with average accuracy rates of 0.9463 and 0.9442. Ricci and Perfetti [20] presented no average sensitivity but a higher average accuracy rate of 0.9595 when compared with the average accuracy rates of all the adaptive thresholding techniques based on IDM information ranging from 0.9468 to 0.9532. Although Xiao et al. [83] presented a higher average accuracy rate of 0.9529 when compared with five of the six investigated adaptive thresholding techniques based on IDM information, there were only significant differences when compared with three average accuracy rates. Two of the six adaptive thresholding using different IDM information techniques presented significantly higher average sensitivity rates of 0.7612 and 0.7644 when compared with the average sensitivity rate of 0.7513 achieved by Xiao et al. [83]. The human observer presented a significantly higher average sensitivity rate of 0.7761 when compared with all the average sensitivity rates of 0.7327, 0.7390, 0.7454, 0.7509, 0.7612 and 0.7644 achieved by the adaptive thresholding techniques based on IDM information. The higher detection rate of both large and thin vessels by the human observer [131] resulted in the higher average sensitivity rate achieved by the human observer [131]. Five of the six adaptive thresholding techniques based on IDM information present higher average accuracy rates of 0.9532, 0.9506, 0.9521, 0.9511 and 0.9502 when compared with the average accuracy of 0.9473 achieved by the human observer with significant differences.

The adaptive thresholding using different ASM range information techniques investigated achieved average sensitivity rates of 0.7313, 0.7375, 0.7397, 0.7560, 0.7632 and 0.7650 with corresponding average accuracy rates of 0.9511, 0.9503, 0.9488, 0.9477, 0.9461 and 0.9449 respectively on DRIVE database. All the adaptive thresholding using different ASM range information techniques presented significantly higher average sensitivity rates of 0.7313, 0.7375, 0.7397, 0.7560, 0.7632 and 0.7650 with significantly higher average accuracy rates of 0.9511, 0.9503, 0.9488, 0.9477, 0.9461 and 0.9449 when compared with average sensitivity rates of 0.3357, 0.6399, 0.6971, 0.6389, 0.7145 and 0.6522 with their corresponding average accuracy rates of 0.8773, 0.9212, 0.9377, 0.9181, 0.9416 and 0.9267 achieved by Chaudhuri et al. [26], Jiang and Mojon [38], Zana and Klein [40], Martinez-Perez et al. [135], Niemeijer et al [35] and Yin et al. [87] respectively. Three of the six adaptive thresholding techniques using different ASM information presented significantly higher average sensitivity rates of 0.7560, 0.7632 and

0.7650 when compared with the average sensitivity rate of 0.7468 achieved by Vlachos and Dermatas [41]. All the adaptive thresholding techniques using different ASM information presented significantly higher average accuracy rates 0.9511, 0.9503, 0.9488, 0.9477, 0.9461 and 0.9449 when compared with the average accuracy rate of 0.9285 achieved by Vlachos and Dermatas [41].

Szpak and Tapamo [138] presented no average sensitivity but a significantly lower average accuracy rate of 0.9299 when compared with all the average accuracy rates of 0.9511, 0.9503, 0.9488, 0.9477, 0.9461 and 0.9449 achieved by adaptive thresholding using different ASM range information. Four of the six adaptive thresholding using different ASM range information techniques presented higher average accuracy rates of 0.9511, 0.9503, 0.9488 and 0.9477 when compared with an average accuracy rate of 0.9452 achieved by Marin et al. [28] with significant differences. Three of the six adaptive thresholding using different ASM range information techniques presented higher average accuracy rates of 0.9511, 0.9503 and 0.9488 when compared with the average accuracy rate of 0.9469 achieved by Akram and Khan [46] with significant differences. Mendonca et al. [84] presented a lower average sensitivity rate of 0.7315 when compared with five of the six average sensitivity rates of 0.7375, 0.7397, 0.7560, 0.7632 and 0.7650 achieved by proposed adaptive thresholding techniques based on ASM information with significant differences. Four of the six proposed adaptive thresholding techniques based on ASM information presented higher average accuracy rates of 0.9511, 0.9503, 0.9488 and 0.9477 when compared with average accuracy rates of 0.9466 and 0.9463 presented in [23] and [84] with significant differences.

Staal et al. [22] presented a lower average sensitivity rate of 0.7345 when compared with five average sensitivity rates 0.7375, 0.7397, 0.7560, 0.7632 and 0.7650 achieved by proposed adaptive thresholding techniques based on ASM information with significant differences. A lower average accuracy rate of 0.9442 was also presented in [22] when compared with five average accuracy rates of 0.9511, 0.9503, 0.9488, 0.9477, and 0.9461 achieved by the adaptive thresholding techniques based on ASM information with significant differences. Wang et al. [43] presented no average sensitivity but a lower average accuracy rate of 0.9461 when compared with four average accuracy rates 0.9511, 0.9503, 0.9488 and 0.9477 achieved by adaptive thresholding techniques based on ASM information with significant differences. Ricci and Perfetti [20] presented no average sensitivity but a higher average accuracy rate of 0.9595 when compared with all the average accuracy rates of the adaptive thresholding techniques based on ASM information. Xiao et al. [83] presented a higher average accuracy rate of 0.9529 when compared with all the average accuracy rates of the adaptive thresholding techniques

based on ASM information but a lower average sensitivity rate of 0.7513 when compared with three average sensitivity rates 0.7560, 0.7632 and 0.7650 of the six proposed adaptive thresholding techniques based on ASM information with significant differences. The human observer presented a significantly higher average sensitivity rate of 0.7761 when compared with all the average sensitivity rates of 0.7313, 0.7375, 0.7397, 0.7560, 0.7632 and 0.7650 achieved by the adaptive thresholding techniques based on ASM information. Three of the proposed adaptive thresholding techniques based on ASM information presented higher average accuracy rates of 0.9511, 0.9503 and 0.9488 when compared with the average accuracy rate of 0.9473 achieved by the human observer with significant differences.

4.4.4 Adaptive Thresholding Techniques on STARE Database

The adaptive thresholding using different IDM information techniques investigated achieved average sensitivity rates of 0.7501, 0.7506, 0.7530, 0.7613, 0.7661 and 0.7662 with corresponding average accuracy rates of 0.9511, 0.9526, 0.9546, 0.9529, 0.9550 and 0.9492 respectively on STARE database. Hoover et al. [21] presented a significantly lower average sensitivity rate of 0.6751 and average accuracy rate of 0.9275 when compared with all the average sensitivity rates of 0.7501, 0.7506, 0.7530, 0.7613, 0.7661 and 0.7662 with corresponding average accuracy rates of 0.9511, 0.9526, 0.9546, 0.9529, 0.9550 and 0.9492 respectively achieved by the adaptive thresholding techniques based on different local homogeneity information. The work of Jiang and Mojon [38] achieved a significant lower average accuracy rate of 0.9009 when compared with all the average accuracy rates of 0.9511, 0.9526, 0.9546, 0.9529, 0.9550 and 0.9492 achieved by the adaptive thresholding using different local homogeneity information. Staal et al. [22] presented a lower average accuracy rate of 0.9516 when compared with four average accuracy rates of 0.9526, 0.9529, 0.9546 and 0.9550 achieved by the adaptive thresholding techniques based on local homogeneity information with significant differences. Staal et al. [22] also presented a significantly lower average sensitivity rate 0.6970 when compared with all the average sensitivity rates of 0.7501, 0.7506, 0.7530, 0.7613, 0.7661 and 0.7662 achieved by the adaptive thresholding techniques based on local homogeneity information. Mendonca et al. [84], Xiao et al. [83] and Yin et al. [87] presented lower average sensitivity rates of 0.7123, 0.7147 and 0.7248 with corresponding lower average accuracy rates of 0.9479, 0.9476 and 0.9412 when compared with all the average sensitivity rates of 0.7501, 0.7506, 0.7530, 0.7613, 0.7661 and 0.7662 with corresponding average accuracy rates of 0.9511, 0.9526, 0.9546, 0.9529, 0.9550 and 0.9492

respectively achieved by the adaptive thresholding techniques based on different local homogeneity information with significant differences. Marin et al. [28] presented no sensitivity rate but a lower average accuracy rate of 0.9526 when compared with three average accuracy rates 0.9529, 0.9546 and 0.9550 obtained using adaptive thresholding techniques based on local homogeneity information. Two of the three average accuracy rates achieved significant improvements when compared with the average accuracy rate of 0.9526 presented by Marin et al. [28]. Wang et al. [43] presented no sensitivity rate but a lower average accuracy rate of 0.9521 when compared with four average accuracy rates 0.9526, 0.9529, 0.9546 and 0.9550 obtained using adaptive thresholding techniques based on local homogeneity information. Two of the four average accuracy rates achieved significant improvements when compared with the average accuracy rate of 0.9521 presented by Wang et al. [43]. Akram and Khan [46] presented no sensitivity rate but a lower average accuracy rate of 0.9502 when compared with five average accuracy rates 0.9526, 0.9546, 0.9529 and 0.9550 obtained using adaptive thresholding techniques based on local homogeneity information with slight significant differences. Soares et al. [23] also presented a lower average accuracy rate of 0.9480 when compared with all the average accuracy rates 0.9492, 0.9511, 0.9526, 0.9529, 0.9546 and 0.9550 obtained using adaptive thresholding techniques based on local homogeneity information with significant differences. Ricci and Perfetti [20] presented no sensitivity rate but a higher average accuracy rate of 0.9584 when compared with all the average accuracy rates 0.9511, 0.9526, 0.9546, 0.9529, 0.9550 and 0.9492 obtained using adaptive thresholding techniques based on local homogeneity information. The human observer [132] presented a significantly higher average sensitivity rate of 0.88949 when compared with all the average sensitivity rates of 0.7501, 0.7506, 0.7530, 0.7613, 0.7661 and 0.7662 achieved by the adaptive thresholding techniques based on local homogeneity information. The higher detection rate of both large and thin vessels by the human observer [132] resulted in the higher average sensitivity rate achieved by the human observer [132]. The human observer [132] presented a significantly lower average accuracy rate of 0.9354 when compared with all the average accuracy rates 0.9492, 0.9511, 0.9526, 0.9529, 0.9546 and 0.9550 achieved by the adaptive thresholding techniques based on local homogeneity information.

All the proposed adaptive thresholding using different local homogeneity information presented higher AUC rates 0.9682, 0.9707, 0.9699, 0.9713, 0.9722 and 0.9705 (see Table 4.6) when compared with the AUC rates 0.9520, 0.9294, 0.8984, 0.9194, 0.9543, 0.7878, 0.9614, 0.963, 0.9588 and 0.9558 achieved by the previously proposed techniques on DRIVE database with significant differences.

All the proposed adaptive thresholding using different local homogeneity information presented higher AUC rates 0.9642, 0.9705, 0.9741, 0.9818, 0.9819 and 0.9824 when compared with the AUC rates 0.9602, 0.9614 and 0.929 achieved by Ricci and Perfetti [20], Staal et al. [22] and Jiang and Mojon [38] respectively with significant differences on STARE database. Five AUC rates 0.9705, 0.9741, 0.9818, 0.9819 and 0.9824 obtained by the proposed adaptive thresholding using different local homogeneity information are significantly higher than the AUC rates 0.9671 and 0.9682 achieved by Soares et al. [23] and Wang et al. [43] respectively on STARE database. Four AUC rates 0.9741, 0.9818, 0.9819 and 0.9824 obtained by the proposed adaptive thresholding using different local homogeneity information are significantly higher than the AUC rate 0.970 achieved by Akram and Khan [46] on STARE database. Three AUC rates 0.9818, 0.9819 and 0.9824 obtained by the proposed adaptive thresholding using different local homogeneity information are significantly higher than the AUC rate 0.9769 achieved by Marin et al. [28] on STARE database.

The adaptive thresholding using different ASM range information techniques investigated achieved average sensitivity rates of 0.7427, 0.7428, 0.7458, 0.7542, 0.7626 and 0.7641 with corresponding average accuracy rates of 0.9504, 0.9500, 0.9485, 0.9457, 0.9510 and 0.9500 respectively on STARE database. All the adaptive thresholding techniques based on different ASM range information achieved significantly higher average sensitivity rates of 0.7427, 0.7428, 0.7458, 0.7542, 0.7626 and 0.7641 with significantly higher average accuracy rates of 0.9504, 0.9500, 0.9485, 0.9457, 0.9510 and 0.9500 when compared with the average sensitivity rate of 0.6751 and average accuracy rate of 0.9275 achieved by Hoover et al. [21]. All the adaptive thresholding techniques based on different ASM range information achieved significantly higher average accuracy rates of 0.9504, 0.9500, 0.9485, 0.9457, 0.9510 and 0.9500 when compared with the average accuracy rate 0.9009 achieved by Jiang and Mojon [38]. Staal et al. [22] presented a higher average accuracy rate of 0.9516 when compared with all the average accuracy rates of 0.9504, 0.9500, 0.9485, 0.9457, 0.9510 and 0.9500 achieved by the adaptive thresholding techniques based on ASM range information. Staal et al. [22], however, presented a significantly lower average sensitivity rate of 0.6970 when compared with all the average sensitivity rates of 0.7427, 0.7428, 0.7458, 0.7542, 0.7626 and 0.7641 achieved by the adaptive thresholding techniques based on ASM range information. Mendonca et al. [84], Xiao et al. [83] and Yin et al. [87] presented significantly lower average sensitivity rates of 0.7123, 0.7147 and 0.7248 when compared with all the average sensitivity rates 0.7427, 0.7428, 0.7458, 0.7542, 0.7626 and 0.7641 achieved by the adaptive thresholding techniques based on different ASM range information. Yin

et al [87] presented a lower average accuracy rate of 0.9412 when compared with all the average accuracy rates 0.9504, 0.9500, 0.9485, 0.9457, 0.9510 and 0.9500 obtained using adaptive thresholding techniques based on ASM information with significant differences. Mendonca et al. [84] presented a lower average accuracy rate of 0.9479 when compared with five average accuracy rates 0.9485, 0.9500, 0.9500 0.9504 and 0.9510 obtained using adaptive thresholding techniques based on ASM information. Four of the five average accuracy rates achieved significant improvements when compared with the average accuracy rate of 0.9479 achieved by Mendonca et al. [84]. Xiao et al. [83] presented a significantly lower average accuracy rate of 0.9476 when compared with five average accuracy rates 0.9485, 0.9500, 0.9500 0.9504 and 0.9510 obtained using adaptive thresholding techniques based on ASM information. Marin et al. [28], Ricci and Perfetti [20] and Wang et al. [43] presented no sensitivity rate but higher average accuracy rates 0.9526, 0.9584 and 0.9521 when compared with all the average accuracy rates 0.9504, 0.9500, 0.9485, 0.9457, 0.9510 and 0.9500 obtained using adaptive thresholding techniques based on ASM information. Akram and Khan [46] presented no sensitivity rate but a lower average accuracy rate of 0.9502 when compared with two average accuracy rates 0.9504 and 0.9510 obtained using adaptive thresholding techniques based on ASM information. The difference between the average accuracy rate achieved in [46] and the two average accuracy rates obtained by adaptive thresholding techniques based on ASM information is not significant. Soares et al. [23] presented a lower average accuracy rate of 0.9480 when compared with five average accuracy rates 0.9504 and 0.9510 obtained using adaptive thresholding techniques based on ASM information. Four of the five average accuracy rates achieved significant improvements when compared with the average accuracy rate of 0.9480 achieved by Soares et al. [23]. The human observer [132] presented a significantly higher average sensitivity rate of 0.88949 when compared with all the average sensitivity rates of 0.7427, 0.7428, 0.7458, 0.7542, 0.7626 and 0.7641 achieved by the adaptive thresholding techniques based on ASM information. The higher detection rate of both large and thin vessels by the human observer [132] resulted in the higher average sensitivity rate achieved by the human observer [132]. The human observer [132] presented a significantly lower average accuracy rate of 0.9354 when compared with all the average accuracy rates 0.9504, 0.9500, 0.9485, 0.9457, 0.9510 and 0.9500 achieved by the adaptive thresholding techniques based on ASM information.

All the proposed adaptive thresholding methods based on different ASM information achieved higher AUC rates 0.9656, 0.9711, 0.9698, 0.9734, 0.9680 and 0.9658 when compared with the AUC rates 0.9520, 0.9294, 0.8984, 0.9194, 0.9543, 0.7878, 0.9614,

0.963, 0.9588 and 0.9558 achieved by the previously proposed techniques on DRIVE database with significant differences.

All the proposed adaptive thresholding methods based on different ASM information presented higher AUC rates 0.9671, 0.9681, 0.9695, 0.9745, 0.9781 and 0.9782when compared with the AUC rates 0.9602, 0.9614 and 0.929 achieved by Ricci and Perfetti [20], Staal et al. [22] and Jiang and Mojon [38] respectively on STARE database with significant differences. Four AUC rates 0.9695, 0.9745, 0.9781 and 0.9782 obtained by the proposed adaptive thresholding using different ASM information are significantly higher than the AUC rates 0.9671 and 0.9682 achieved by Soares et al. [23] and Wang et al. [43] respectively on STARE database. Three AUC rates 0.9745, 0.9781 and 0.9782 obtained by the proposed adaptive thresholding using different ASM information are significantly higher than the AUC rate 0.970 achieved by Akram and Khan [46] on STARE database. Two AUC rates 0.9781 and 0.9782 obtained by the proposed adaptive thresholding using different ASM information are significantly higher than the AUC rate 0.9769 achieved by Marin et al. [28] on STARE database.

While all the adaptive thresholding techniques are computationally faster when compared with the techniques presented in [22], [23], [28], [43], [83], [84], the computing environment are different. All the adaptive thresholding techniques are computationally faster when compared with the human observer [131](1846.15 times).

4.4.5 Clustering-Based Approaches on DRIVE Database

Phase congruence combined with fuzzy c-means achieved an average sensitivity rate of 0.6725 and an average accuracy rate of 0.9431 on DRIVE database. Phase congruence combined with fuzzy c-means presented significantly higher average sensitivity rate of 0.6725 and average accuracy rate of 0.9431 when compared with Chaudhuri et al. [26], Jiang and Mojon [38], Martinez-Perez et al. [135] and Yin et al. [87] with average sensitivity rates of 0.3357, 0.6399, 0.6389, 0.6522 and corresponding average accuracy rates of 0.8773, 0.9212, 0.9181 and 0.9267 respectively. Phase congruence combined with fuzzy c-means achieved a lower average sensitivity rate of 0.6725 but a higher average accuracy rate of 0.9431 when compared with Niemeijer et al [35], Vlachos and Dermatas [41] and Zana and Klein [40] with average sensitivity rates of 0.7145, 0.7468 and 0.6971 with corresponding average accuracy rates of 0.9416, 0.9285 and 0.93377 respectively. Mendonca et al. [84], Staal et al. [22] and Xiao et al. [83] presented higher average sensitivity rates of 0.7315, 0.7345 and 0.7513 with average accuracy rates of 0.9463, 0.9442 and 0.9529 when compared with phase congruence combined with fuzzy

c-means with average sensitivity rate of 0.6725 and average accuracy rate of 0.9431. The higher sensitivity rates achieved in [84], [22], [83] indicated the ability of those techniques to detect more vessels. Akram and Khan [46], Marin et al. [28], Soares et al. [23], Ricci and Perfetti [20], and Wang et al. [43] presented significantly higher average accuracies rates of 0.9502, 0.9526, 0.9584, 0.9480 and 0.9521 respectively when compared with phase congruence combined with fuzzy c-means. Phase congruence combined with fuzzy c-means achieved a significantly higher average accuracy rate of 0.9431 when compared with the average accuracy rate of 0.9299 achieved by Szpak and Tapamo [138]. The average sensitivity rate of 0.6725 and average accuracy rate of 0.9431 achieved by phase congruence combined with fuzzy c-means are significantly lower than the average sensitivity rate of 0.7761 and average accuracy rate of 0.9473 achieved by the second human observer [131]. The higher detection rate of both large and thin vessels by the human observer [131] resulted in the higher average sensitivity rate achieved by the human observer [131].

The k-means clustering techniques investigated achieved average sensitivity rates of 0.6315, 0.6459, 0.7079, 0.7399, 0.7518 and 0.7581 with corresponding average accuracy rates of 0.9555, 0.9555, 0.9523, 0.9556, 0.9531 and 0.9516 respectively on DRIVE database. Four of the techniques that combined difference image with k-means clustering presented significantly higher average sensitivity rates of 0.7079, 0.7399, 0.7518 and 0.7581 with significantly higher average accuracy rates of 0.9523, 0.9556, 0.9531 and 0.9516 when compared with the average sensitivity rates of 0.3357, 0.6399, 0.6971, 0.6389 and 0.6522 with their corresponding average accuracy rates of 0.8773, 0.9212, 0.9377, 0.9181 and 0.9267 achieved by Chaudhuri et al. [26], Jiang and Mojon [38], Zana and Klein [40], Martinez-Perez et al. [135] and Yin et al. [87] respectively. Three of the techniques that combined difference image with k-means clustering presented significantly higher average sensitivity rates of 0.7399, 0.7518 and 0.7581 with significantly higher average accuracy rates of 0.9556, 0.9531 and 0.9516 when compared with the average sensitivity rates of 0.7315, 0.7145 and 0.7345 with their corresponding average accuracy rates of 0.9463, 0.9416 and 0.9442 presented by Mendonca et al. [84], Niemeijer et al [35] and Staal et al. [22] respectively. Two of the techniques that combined difference image with k-means clustering presented significantly higher average sensitivity rates of 0.7518 and 0.7581 with significantly higher average accuracy rates of 0.9531 and 0.9516 when compared with the average sensitivity rate of 0.7468 and average accuracy rate of 0.9285 achieved by Vlachos and Dermatas [41]. Although two of the techniques that combined difference image with k-means clustering presented higher average sensitivity rates of 0.7518 and 0.7581 when compared with Xiao et al.

[83] where an average sensitivity rate of 0.7513 was achieved, one of of the technique presented a significantly higher average sensitivity rate of 0.7581 when compared with the average sensitivity rate 0.7513 achieved by Xiao et al. [83]. All the k-means clustering techniques investigated achieved significantly higher average accuracy rates of 0.9555, 0.9555, 0.9523, 0.9556, 0.9531 and 0.9516 when compared with Akram and Khan [46], Marin et al. [28], Soares et al.[23], Szpak and Tapamo [138] and Wang et al. [43] where no average sensitivity rate was presented but average accuracy rates of 0.9469, 0.9452, 0.9466, 0.9299 and 0.9461 were achieved respectively. All the difference images combined with k-means presented lower average sensitivity rates of 0.6315, 0.6459, 0.7079, 0.7399, 0.7518 and 0.7581 but significantly higher average accuracy rates of 0.9555, 0.9555, 0.9523, 0.9556, 0.9531 and 0.9516 when compared with the second human observer with average sensitivity rate of 0.7761 and average accuracy rate of 0.9473.

4.4.6 Clustering-Based Approaches on STARE Database

Phase congruence combined with fuzzy c-means achieved an average sensitivity rate of 0.4886 and an average accuracy rate of 0.9346 on STARE database. Hoover et al. [21] presented significantly higher average sensitivity rate of 0.6751 and a lower average accuracy rate of 0.9275 when compared with the combination of phase congruence and fuzzy c-means with an average sensitivity rate of 0.4886 and an average accuracy rate of 0.9346. The combination of phase congruence and fuzzy c-means presented a significant higher average accuracy rate of 0.9346 when compared with the work of Jiang and Mojon [38] that achieved an average accuracy rate of 0.9009. Staal et al. [22], Mendonca et al. [84], Xiao et al. [83] and Yin et al. [87] presented significantly higher average sensitivity rates of 0.6970, 0.7123, 0.7147 and 0.7248 with higher average accuracy rates of 0.9516, 0.9479, 0.9476 and 0.9412 respectively when compared with the average sensitivity rate of 0.4886 and the average accuracy rate of 0.9346 achieved by phase congruence combined with fuzzy c-means. Akram and Khan [46], Marin et al. [28], Ricci and Perfetti [20], Soares et al.[23] and Wang et al. [43] presented significantly higher average accuracy rates of 0.9502, 0.9526, 0.9584, 0.9480 and 0.9521 when compared with the average accuracy rate of 0.9346 achieved by phase congruence combined with fuzzy c-means. The human observer achieved significantly higher average sensitivity rate of 0.8949 when compared with the average sensitivity rate of 0.4886 achieved on phase congruence combined with fuzzy c-means. Higher average sensitivity rate was achieved by the human observer reflected the higher detection rate of both large and

thin vessel when compared with phase congruence combined with fuzzy c-means.

While fuzzy c-means combined with phase congruence is computationally faster when compared with the techniques presented in [22], [23], [28], [43], [83], [84], the computing environment are different. Fuzzy c-means combined with phase congruence is computationally faster when compared with human observer [131](265.7 times).

The k-means clustering techniques investigated achieved average sensitivity rates of 0.6516, 0.6567, 0.6979, 0.7372, 0.7666 and 0.7772 with corresponding average accuracy rates of 0.9312, 0.9344, 0.9340, 0.9509, 0.9500 and 0.9492 respectively on STARE database. Four of the techniques that combined difference image with k-means clustering presented significantly higher average sensitivity rates of 0.6979, 0.7372, 0.7666 and 0.7772 with significantly higher average accuracy rates of 0.9340, 0.9509, 0.9500 and 0.9492 when compared with the average sensitivity rate of 0.6751 and average accuracy rate of 0.9275 achieved by Hoover et al. [21]. All the k-means clustering techniques investigated presented significant higher average accuracy rates of 0.9312, 0.9344, 0.9340, 0.9509, 0.9500 and 0.9492 when compared with the work of Jiang and Mojon [38] that achieved an average accuracy rate of 0.9009. Although four of the techniques that combined difference image with k-means clustering presented higher average sensitivity rates of 0.6979, 0.7372, 0.7666 and 0.7772 when compared with the average sensitivity rate of 0.6951 achieved by Staal et al. [22], only three of the average sensitivity have significant differences when compared with Staal et al. [22]. Three of the techniques that combined difference image with k-means clustering presented significantly higher average sensitivity rates of 0.7372, 0.7666, 0.7772 and significantly higher average accuracy rates of 0.9509, 0.9500 0.9492 when compared with the average sensitivity rates of 0.7123, 0.7147 and 0.7248 with corresponding average accuracy rates of 0.9479, 0.9476 and 0.9412 presented by Mendonca et al. [84], Xiao et al. [83] and Yin et al. [87] respectively. Marin et al. [28], Ricci and Perfetti [20] and Wang et al. [43] presented no sensitivity but higher average accuracy rates 0.9526, 0.9584 and 0.9521 when compared with the average accuracy rates of all the k-means clustering segmentation techniques in the range 0.9312 to 0.9509. Akram and Khan [46] presented no sensitivity but a lower average accuracy rate of 0.9502 when compared with average accuracy rate of 0.9509 obtained using one of the k-means clustering segmentation techniques with no significant difference. Soares et al. [23] also presented a lower average accuracy rate of 0.9480 when compared with the average accuracy rates of 0.9509, 0.9500 and 0.9492 obtained from three of the k-means clustering segmentation techniques with significant differences. The human observer [132] presented a higher average sensitivity of 0.88949 when compared with all the average sensitivity rates of k-means clustering

segmentation techniques. The higher average sensitivity rate achieved by the human observer [132] showed the higher detection rate of both large and thin vessels by the human observer in the retinal images. The human observer [132], however, presented a significantly lower average accuracy rate of 0.9354 when compared with the average accuracy rates of 0.9509, 0.9500 and 0.9492 obtained from three of the k-means clustering segmentation techniques.

Four of the proposed k-means clustering techniques (see Table 4.6) presented significantly higher AUC rates of 0.9719, 0.9735, 0.9749 and 0.9758 when compared with the AUC rates 0.9558, 0.9520, 0.9614, 0.7878, 0.9588, 0.9294, 0.9114 0.8984, 0.9543 and 0.963 achieved by the previously proposed techniques by Ricci and Perfetti [20], Staal et al. [22], Soares et al. [23], Chaudhuri et al. [26], Marin et al. [28], Niemeijer et al [35] , Jiang and Mojon [38], Zana and Klein [40], Wang et al. [43] and Akram and Khan [46] on DRIVE.

Three of the proposed k-means clustering techniques on STARE (see Table 4.7) presented significantly higher AUC rates of 0.9728, 0.9734 and 0.9756 when compared with the AUC rates of 0.9602, 0.929, 0.9614, 0.9671, 0.9682 and 0.970 achieved by Ricci and Perfetti [20], Jiang and Mojon [38], Staal et al. [22], Soares et al.[23], Wang et al. [43] and Akram and Khan [46] respectively.

While all the difference image combined with k-means are computationally faster when compared with the techniques presented in [22], [23], [28], [43], [83], [84], the computing environment are different. All the difference image combined with k-means are computationally faster when compared with the human observer [131](1800 times).

4.5 Tortuosity Measures With Ground Truth

The tortuosity measures computed in the previous chapter utilised chord length, arc length and the frequency of twists using the stationary points of the vessel curves. The non-normalised tortuosity index (TI) combined a different distance metric and the vessel twist frequency as described in equation (3.71). The normalised TI as described in equation (3.70), utilised the chord length for the normalisation previously presented distance metric combined with the twist frequency measure. Table 4.8 shows the correlation of the tortuosity measures obtained with the expert ground truth using Spearman's rank correlation coefficient.

The result obtained shows that the non-normalised metric (TI_{freq2}) has a stronger correlation with the expert ground truth with significant differences when compared with the other techniques investigated.

Table 4.8: Correlation of Tortuosity Measures With Expert's Ground Truth

Tortuosity Measure	**Normal TI**	**Tortuous TI**	**Correlation Measure**
L_{curve}/L_{chord}	$0 \leq TI \leq 1$	TI>1	0.73
TI_{freq1}	$0 \leq TI \leq 1$	TI >1	0.73
TI_{freq2}	$0 \leq TI \leq 1$	TI >1	0.80

4.6 Summary

The results obtained from the different investigated segmentation techniques show that the ASM-based local adaptive thresholding technique, IDM-based local adaptive thresholding technique and k-means combined with DIMDF, DIMDMNF, and DIMDGF detect both large and thin vessels in the retinal images.

K-means clustering combined with difference image based on median filtering (DIMDF) as well as the local adaptive thresholding techniques based on local homogeneity information and energy information are computationally efficient, robust for the segmentation of both large and thin retinal vessels, and also reduce the false detection of vessels around the border of the optic disc. These were demonstrated as the proposed adaptive thresholding techniques and k-means clustering presented higher average sensitivity, average accuracy and very good specificity rates when compared with previous works.

The experimental results showed that the proposed TI presented a stronger correlation with the expert's ground truth. The non-normalised tortuosity index that combined the different distance metric and the vessel twist frequency has a stronger correlation with the expert ground truth when compared with the previously presented distance metric measure in [53], [54], [55], [56], [57] and the normalised TI investigated in this thesis. Hence, the non-normalised TI measure that combines vessel twist frequency and distance metric is proposed for the measurement of vessel tortuosity in this thesis.

The next chapter shall give the conclusion of this research and recommendations for future work.

Chapter 5

Conclusion and Recommendations for Future Work

5.1 Summary and Contribution

A detailed survey of the literature on retinal vessel segmentation and vessel tortuosity measurement was carried out in this research. Previously proposed unsupervised segmentation methods in the literature are faced with the inability to detect thin vessels as well as the limitation of connectivity loss of vessel network structures [38], [80]. While some unsupervised techniques have made significant progress at further improving the automatic detection of retinal vessels, the detection of thinner vessels remained a challenge [34], [43]. Although the previously proposed supervised methods achieved higher average accuracy and sensitivity rates when compared with the previously proposed unsupervised methods in the literature, the inability to detect thinner vessels and the high dependence of the supervised methods on training set with the requirement of retraining when vessels segmentation is performed on new datasets remain their major drawbacks [16]. The non-availability of reliable labelled training samples by experts for the supervised segmentation methods which could sometimes be expensive or unavailable and the time complexity of supervised segmentation are their other drawbacks [32], [81]. Furthermore, the reduction of the false positives around the border of the optic disk in the vessel segmentation techniques [20], [42] needs to be improved. Although several vessel tortuosity methods were discussed in the literature, the need for an improved tortuosity method is still required.

The afore-mentioned drawbacks of the previous methods in the literature served as

the motivation of this research to investigate fast unsupervised segmentation model for an automatic detection of large and thin vessels and the characterisation of the detected vessels using tortuosity measure that combines distance metric and vessel twists. In order to address the problems, this research work investigated different unsupervised segmentation approaches such as global thresholding, local adaptive thresholding and clustering methods for the robust detection of large and thin retinal vessels in a timely efficient manner.

Firstly, this research contributes to knowledge by conducting a comparative study on the use of different global thresholding techniques combined with different pre-processing and post-processing techniques [69]. Through the investigation of the phase congruence-based global thresholding approach and Contrast Limited Adaptive Histogram Equalisation (CLAHE)- based global thresholding approach, this research showed that some global thresholding techniques are limited in efficiently segmenting thin vessels in retinal images. While investigating the global thresholding approaches, this research showed that CLAHE based global thresholding techniques based on Otsu and Isodata thresholds detected the large vessels but failed to detect the thin vessels. This was due to the fact that the thin vessels have very low contrast and are difficult to distinguish from the background tissues using these histogram based thresholding techniques. Two new multi-scale approaches of computing global threshold based on the different texture information such as inverse difference moment and sum-entropy combined with phase congruence pre-processing that could help achieve an improved detection of vessels were implemented to extend the technique proposed by Amin and Hong [48] for the detection of retinal blood vessels. When compared with [48], the two multi-scale approaches presented higher average accuracy rates. Phase congruence combined with the multi-scale approaches of computing global threshold segmented large and some thin vessels but achieved lower performances on STARE due to some undetected thin vessels and the reduced width of detected large and thin vessels. Although this resulted in low sensitivity rates, relatively good accuracy rates are still maintained. Another comparative study on the use of fuzzy c-means combined with phase congruence and the GLCM sum entropy combined with phase congruence for vessel segmentation was achieved in this research. The investigation demonstrated the higher average accuracy rate but a longer running time fuzzy c-means combined with phase congruence when compared with the multi-scale based sum entropy thresholding combined with phase congruence. When compared with the literature, both methods achieved considerable faster running time.

Another contribution of this research is the implementation of the two novel local

adaptive thresholding techniques for the segmentation of large and thin retinal vessels based on two different Haralick texture features namely, local homogeneity and energy. Although these two texture features have been applied for supervised image segmentation in the literature, their novelty in this thesis lies in that they are applied using an unsupervised image segmentation approach. Rather than adopting a global approach, each of these local adaptive thresholding techniques locally applied a multi-scale approach on the different texture information considering the pixel of interest and its relationship with the spacial neighbourhood to compute the local adaptive threshold. The multi-scale approach handles the challenge of vessel's width variation. Experiments showed that the two novel local adaptive thresholding techniques achieved a higher reduction of false vessels around the border of the optic disc when compared with some very good previous techniques in the literature. Experimental results showed that the average sensitivity rates, average accuracy rates and AUC values of these local adaptive techniques showed significant improvements when compared with the unsupervised and supervised vessel segmentation methods in the literature. These techniques also achieved a highly improved computational time of 1.9 to 3.9 seconds when compared with state of the art. Hence, the two novel local adaptive thresholding techniques are proposed for the segmentation of vessels in retinal images in this thesis.

Another contribution of this research is the investigation of various difference images combined with k-means clustering technique for the segmentation of large and thin vessels in retinal images. Different low pass filters such as median filter, mean filter and Gaussian filter are applied each to smoothen and compute various difference images. This research established that in order to achieve a good vessel segmentation using difference images combined with k-means clustering technique, a difference image that preserves the vessel details of the retinal image is required. The investigation, however, showed that the median filter yielded the best difference image required by k-means clustering for the segmentation the retinal vessels. Further experiments showed that the linear combination of median filter based difference images with Gaussian and mean filter based difference images respectively when combined with k-means clustering technique led to the detection of more thinner vessels. Experiments showed that the false detection around the border of the optic disc were higher on the segmented vessels obtained by using DIMDMNF, DIMDGF and DIMNGF while combined with k-means clustering but lesser on the segmented vessels obtained while using k-means combined with DIMDF. Experimental results showed that the average sensitivity rates, average accuracy rates and AUC values of these median filter based difference images combined with k-means clustering technique (that is, DIMDF, DIMDMNF and DIMDGF)

achieved significant improvements when compared with the literature. The median filter based difference images combined with k-means clustering technique (that is, DIMDF) also achieved a higher reduction of false vessels around the border of the optic disc when compared with some very good previous techniques in the literature. These methods also achieved a highly improved computational time of 3.4 to 4 seconds when compared with the literature. Hence, median filter based difference images combined with k-means clustering technique (that is, DIMDF, DIMDMNF and DIMDGF) are proposed for the segmentation of vessels in retinal images.

Furthermore, this research contributes to knowledge by utilising stationary points on the vessels to detect vessel twists. The detection of the stationary point did not only help at checking the change of direction and twists in the vessels but also helped at detecting the straightness and non-straightness of the vessels. The combination of vessel twist frequency and distance metric for the computation of normalised and non-normalised tortuosity index (TI)measure was investigated in this research. Experimental results showed that the non-normalised TI measure has a stronger correlation with the expert's ground truth when compared to the distance metric and the normalised TI measures. Hence, the non-normalised TI measure that combined vessel twist frequency and distance metric is proposed for the measurement of vessel tortuosity in this thesis.

5.2 Recommendations for Future Work

Considering the high sensitivity, accuracy, AUC and timely efficient rates of the two proposed local adaptive thresholding techniques and the proposed difference images combined with k-means clustering technique (that is, DIMDF, DIMDMNF and DIMDGF), future work could extend the use of these proposed vessel segmentation techniques to retinal biometric-based systems. The proposed tortuosity measure that combines vessel twist frequency based on stationary points with distance metric could be applied for the progress monitoring of the various retinopathies. The inclusion of retinal images from various African descents over a period of time may possibly provide interesting insights into further use of the proposed vessel tortuosity in the progress monitoring of the retinopathies.

Appendix A

Table A.1: Comparison of the average sensitivity rates of the different adaptive thresholding technique based on IDM information in the thesis and [1] on DRIVE database.

Method I	**Method II**	**Z-Score**	**Significant**
Thesis IDM(MIN_{Range}) 0.7644	IDM(MIN_{Range})[1] 0.7600	5.6	Yes
Thesis IDM(MAX_{Range}) 0.7612	IDM(MAX_{Range})[1] 0.7612	0	No
Thesis IDM($MEAN_{Range}$) 0.7390	IDM($MEAN_{Range}$)[1] 0.7548	19.5	Yes
Thesis IDM(MIN_{IQR}) 0.7509	IDM(MIN_{IQR})[1] 0.7354	19.1	Yes
Thesis IDM(MAX_{IQR}) 0.7324	IDM(MAX_{IQR})[1] 0.7507	22.5	Yes
Thesis IDM($MEAN_{IQR}$) 0.7454	IDM($MEAN_{IQR}$)[1] 0.7243	25.7	Yes

Table A.2: Comparison of the average accuracy rates of the different adaptive thresholding technique based on IDM information in this thesis and [1]on DRIVE database

Method I	**Method II**	**Z-Score**	**Significant**
Thesis IDM(MIN_{Range}) 0.9468	IDM(MIN_{Range})[1] 0.9447	5	Yes
Thesis IDM(MAX_{Range}) 0.9502	IDM(MAX_{Range})[1] 0.9474	6.8	Yes
Thesis IDM($MEAN_{Range}$) 0.9506	IDM($MEAN_{Range}$)[1] 0.9469	9	Yes
Thesis IDM(MIN_{IQR}) 0.9511	IDM(MIN_{IQR})[1] 0.9513	0.5	No
Thesis IDM(MAX_{IQR}) 0.9532	IDM(MAX_{IQR})[1] 0.9483	12.2	Yes
Thesis IDM($MEAN_{IQR}$) 0.9521	IDM($MEAN_{IQR}$)[1] 0.9525	1	No

Table A.3: Comparison of the average sensitivity rate 0.7612 achieved by adaptive thresholding technique based on maximum IDM range information and 0.7644 of minimum IDM range information with the average sensitivity rates of the other adaptive thresholding technique based on IDM information on DRIVE database.

Method I	**Method II**	**Z-Score**	**Significant**
IDM(MAX_{Range}) 0.7612	IDM($MEAN_{Range}$) 0.7390	27.6	Yes
IDM(MAX_{Range}) 0.7612	IDM(MIN_{IQR}) 0.7509	12.9	Yes
IDM(MAX_{Range}) 0.7612	IDM(MAX_{IQR}) 0.7327	35.2	Yes
IDM(MAX_{Range}) 0.7612	IDM($MEAN_{IQR}$) 0.7454	19.7	Yes
IDM(MIN_{Range}) 0.7644	IDM($MEAN_{Range}$) 0.7390	31.6	Yes
IDM(MIN_{Range}) 0.7644	IDM(MIN_{IQR}) 0.7509	16.9	Yes
IDM(MIN_{Range}) 0.7644	IDM(MAX_{IQR}) 0.7327	39.3	Yes
IDM(MIN_{Range}) 0.7644	IDM($MEAN_{IQR}$) 0.7454	23.7	Yes

Table A.4: Comparison of the average accuracy rate 0.9502 achieved by adaptive thresholding technique based on maximum IDM range information with the average sensitivity rates of the other adaptive thresholding technique based on IDM information on DRIVE database.

Method I	**Method II**	**Z-Score**	**Significant**
IDM(MAX_{Range}) 0.9502	IDM(MIN_{Range}) 0.9468	8.3	Yes
IDM(MAX_{Range}) 0.9502	IDM($MEAN_{Range}$) 0.9506	1	No
IDM(MAX_{Range}) 0.9502	IDM(MIN_{IQR}) 0.9511	2.2	Yes
IDM(MAX_{Range}) 0.9502	IDM(MAX_{IQR}) 0.9532	7.5	Yes
IDM(MAX_{Range}) 0.9502	IDM($MEAN_{IQR}$) 0.9521	4.7	Yes

Table A.5: Comparison of the average sensitivity rate 0.7661 achieved by adaptive thresholding technique based on maximum IDM range information with the average sensitivity rates of the other adaptive thresholding technique based on IDM information on STARE database.

Method I	**Method II**	**Z-Score**	**Significant**
IDM(MAX_{Range}) 0.7661	IDM(MIN_{Range}) 0.7530	17.8	Yes
IDM(MAX_{Range}) 0.7661	IDM($MEAN_{Range}$) 0.7613	6.6	Yes
IDM(MAX_{Range}) 0.7661	IDM(MIN_{IQR}) 0.7662	0.1	No
IDM(MAX_{Range}) 0.7661	IDM(MAX_{IQR}) 0.7506	21.1	Yes
IDM(MAX_{Range}) 0.7661	IDM($MEAN_{IQR}$) 0.7501	21.7	Yes

Table A.6: Comparison of the average accuracy rate 0.9550 achieved by adaptive thresholding technique based on maximum IDM range information with the average sensitivity rates of the other adaptive thresholding technique based on IDM information on DRIVE database.

Method I	**Method II**	**Z-Score**	**Significant**
IDM(MAX_{Range}) 0.9550	IDM(MIN_{Range}) 0.9546	0.4	No
IDM(MAX_{Range}) 0.9550	IDM($MEAN_{Range}$) 0.9529	2.2	Yes
IDM(MAX_{Range}) 0.9550	IDM(MIN_{IQR}) 0.9492	6.1	Yes
IDM(MAX_{Range}) 0.9550	IDM(MAX_{IQR}) 0.9526	2.6	Yes
IDM(MAX_{Range}) 0.9550	IDM($MEAN_{IQR}$) 0.9511	4.1	Yes

Table A.7: Comparison of the maximum AUC rate 0.9722 achieved by adaptive thresholding technique based on maximum IDM IQR information with the AUC rates of the other adaptive thresholding technique based on IDM information on DRIVE database.

Method I	**Method II**	**Z-Score**	**Significant**
IDM(MAX_{IQR}) 0.9722	IDM(MIN_{Range}) 0.9682	12.6	Yes
IDM(MAX_{IQR}) 0.9722	IDM(MAX_{Range}) 0.9707	4.8	Yes
IDM(MAX_{IQR}) 0.9722	IDM($MEAN_{RANGE}$) 0.9699	7.4	Yes
IDM(MAX_{IQR}) 0.9722	IDM(MIN_{IQR}) 0.9713	2.9	Yes
IDM(MAX_{IQR}) 0.9722	IDM($MEAN_{IQR}$) 0.9705	5.5	Yes

Table A.8: Comparison of the maximum AUC rate 0.9824 achieved by adaptive thresholding technique based on minimum IDM range information with the AUC rates of the other adaptive thresholding technique based on IDM information on STARE database.

Method I	**Method II**	**Z-Score**	**Significant**
IDM(MIN_{RANGE}) 0.9824	IDM(MAX_{Range}) 0.9818	2.6	Yes
IDM(MIN_{RANGE}) 0.9824	IDM($MEAN_{Range}$) 0.9819	2.2	Yes
IDM(MIN_{RANGE}) 0.9824	IDM(MIN_{IQR}) 0.9642	65.6	Yes
IDM(MIN_{RANGE}) 0.9824	IDM(MAX_{IQR}) 0.9741	33.1	Yes
IDM(MIN_{RANGE}) 0.9824	IDM($MEAN_{IQR}$) 0.9705	17.5	Yes

Table A.9: Comparison of the maximum average sensitivity rate 0.7632 achieved by adaptive thresholding technique based on maximum ASM range information using green channel with the average sensitivity rates of the other adaptive thresholding technique based on ASM range information on DRIVE database.

Method I	**Method II**	**Z-Score**	**Significant**
ASM($MEAN_{Range}$) (Green Channel)) 0.7632	ASM(MIN_{Range}) (Grey Intensity) 0.7397	29.2	Yes
ASM($MEAN_{Range}$) (Green Channel)) 0.7632	ASM(MAX_{Range}) (Grey Intensity) 0.7313	39.4	Yes
ASM($MEAN_{Range}$) (Green Channel)) 0.7632	ASM($MEAN_{Range}$) (Grey Intensity) 0.7375	31.9	Yes
ASM($MEAN_{Range}$) (Green Channel)) 0.7632	ASM(MIN_{Range}) (Green Channel) 0.7650	2.3	Yes
ASM($MEAN_{Range}$) (Green Channel)) 0.7632	ASM(MAX_{Range}) (Green Channel) 0.7560	9.1	Yes

Table A.10: Comparison of the average accuracy rate 0.9461 (of the maximum average sensitivity rate) achieved by adaptive thresholding technique based on maximum ASM range information using green channel with the average accuracy rates of the other adaptive thresholding technique based on ASM range information on DRIVE database.

Method I	**Method II**	**Z-Score**	**Significant**
ASM($MEAN_{Range}$) (Green Channel)) 0.9461	ASM(MIN_{Range}) (Grey Intensity) 0.9488	6.5	Yes
ASM($MEAN_{Range}$) (Green Channel)) 0.9461	ASM(MAX_{Range}) (Grey Intensity) 0.9511	12.2	Yes
ASM($MEAN_{Range}$) (Green Channel)) 0.9461	ASM($MEAN_{Range}$) (Grey Intensity) 0.9503	10.2	Yes
ASM($MEAN_{Range}$) (Green Channel)) 0.9461	ASM(MIN_{Range}) (Green Channel) 0.9499	9.2	Yes
ASM($MEAN_{Range}$) (Green Channel)) 0.9461	ASM(MAX_{Range}) (Green Channel) 0.9477	3.8	No

Table A.11: Comparison of the maximum average sensitivity rate 0.7641 achieved by adaptive thresholding technique based on maximum ASM range information using green channel with the average sensitivity rates of the other adaptive thresholding technique based on ASM range information on STARE database.

Method I	**Method II**	**Z-Score**	**Significant**
ASM(MAX_{Range}) (Green Channel)) 0.7641	ASM(MIN_{Range}) (Grey Intensity) 0.7458	24.7	Yes
ASM(MAX_{Range}) (Green Channel)) 0.7641	ASM(MAX_{Range}) (Grey Intensity) 0.7428	28.7	Yes
ASM(MAX_{Range}) (Green Channel)) 0.7641	ASM($MEAN_{Range}$) (Grey Intensity) 0.7427	28.9	Yes
ASM(MAX_{Range}) (Green Channel)) 0.7641	ASM(MIN_{Range}) (Green Channel) 0.7542	13.5	Yes
ASM(MAX_{Range}) (Green Channel)) 0.7641	ASM($MEAN_{Range}$) (Green Channel) 0.7626	2.1	Yes

Table A.12: Comparison of the maximum average accuracy rate 0.9510 achieved by adaptive thresholding technique based on mean ASM range information using green channel with the average accuracy rates of the other adaptive thresholding technique based on ASM range information on DRIVE database.

Method I	**Method II**	**Z-Score**	**Significant**
ASM($MEAN_{Range}$) (Green Channel)) 0.9510	ASM(MIN_{Range}) (Grey Intensity) 0.9485	6.2	Yes
ASM($MEAN_{Range}$) (Green Channel)) 0.9510	ASM(MAX_{Range}) (Grey Intensity) 0.9500	2.5	Yes
ASM($MEAN_{Range}$) (Green Channel)) 0.9510	ASM($MEAN_{Range}$) (Grey Intensity) 0.9504	1.5	No
ASM($MEAN_{Range}$) (Green Channel)) 0.9510	ASM(MIN_{Range}) (Green Channel) 0.9457	12.9	Yes
ASM($MEAN_{Range}$) (Green Channel)) 0.9510	ASM(MAX_{Range}) (Green Channel) 0.9500	2.5	Yes

Table A.13: Comparison of the maximum AUC rate 0.9711 achieved by adaptive thresholding technique based on maximum ASM range information of grey intensity image with the AUC rates of the other adaptive thresholding technique based on ASM information on DRIVE database.

Method I	**Method II**	**Z-Score**	**Significant**
ASM(MAX_{Grey}) 0.9711	ASM(MIN_{Grey}) 0.9656	16.9	Yes
ASM(MAX_{Grey}) 0.9711	ASM($MEAN_{Grey}$) 0.9698	4.1	Yes
ASM(MAX_{Grey}) 0.9711	ASM(MIN_{Green}) 0.9634	23.3	Yes
ASM(MAX_{Grey}) 0.9711	ASM(MAX_{Green}) 0.9680	9.7	Yes
ASM(MAX_{Grey}) 0.9711	ASM($MEAN_{Green}$) 0.9658	16.3	Yes

Table A.14: Comparison of the average sensitivity rates of K-Means With DIMDMNF, K-Means With DIMDGF and K-Means combined with other Median Based Difference Images on DRIVE database.

Method I	**Method II**	**Z-Score**	**Significant**
K-Means With DIMDMNF 0.7581	K-Means With DIMDF 0.7399	22.6	Yes
K-Means With DIMDMNF 0.7581	K-Means With DIMDGF 0.7518	7.9	Yes
K-Means With DIMDGF 0.7518	K-Means With DIMDF 0.7399	14.7	Yes

Table A.15: Comparison of the average sensitivity rates of K-Means With DIMDMNF, K-Means With DIMDGF and K-Means combined with other Median Based Difference Images on STARE database.

Method I	**Method II**	**Z-Score**	**Significant**
K-Means & DIMDMNF 0.7752	K-Means & DIMDF 0.7372	51.5	Yes
K-Means & DIMDMNF 0.7752	K-Means & DIMDGF 0.7666	11.9	Yes
K-Means & DIMDGF 0.7666	K-Means & DIMDF 0.7372	39.6	Yes

Table A.16: Comparison of the AUC rates of K-Means With DIMDMNF, K-Means With DIMDGF and K-Means combined with other Median Based Difference Images on DRIVE database.

Method I	**Method II**	**Z-Score**	**Significant**
K-Means & DIMDGF 0.9758	K-Means & DIMDMNF 0.9749	3.1	Yes
K-Means & DIMDGF 0.9758	K-Means & DIMDF 0.9735	7.9	Yes
K-Means & DIMDGF 0.9758	K-Means & DIMNGF 0.9719	13.1	Yes

Table A.17: Comparison of the AUC rates of K-Means With DIMDMNF, K-Means With DIMDGF and K-Means combined with other Median Based Difference Images on STARE database.

Method I	**Method II**	**Z-Score**	**Significant**
K-Means & DIMDGF 0.9734	K-Means & DIMDMNF 0.9728	2.2	Yes
K-Means & DIMDF 0.9756	K-Means & DIMDGF 0.9734	8.1	Yes
K-Means & DIMDF 0.9756	K-Means & DIMDMNF 0.9728	10.3	Yes
K-Means & DIMDF 0.9756	K-Means & DIMNGF 0.9463	87.9	Yes

Table A.18: Comparison of the average sensitivity rates 0.7327, 0.7390, 0.7454, 0.7509, 0.7612 and 0.7644 achieved by adaptive thresholding technique based IDM information using green channel with the other techniques in the literature on DRIVE database.

Method I	**Method II**	**Z-Score**	**Significant**
Least of the Six Avg. Sens. rates of Local IDM Info. 0.7327	Chaudhuri et al. [26] 0.3357	427.7	Yes
„„	Jiang and Mojon [38] 0.6399	107.5	Yes
„„	Zana and Klein [40] 0.6971	42.4	Yes
„„	Martinez-Perez et al. [135] 0.6389	108.6	Yes
„„	Niemeijer et al [35] 0.7145	21.9	Yes
„„	Yin et al. [87] 0.6522	93.7	Yes
Local IDM info. rate 0.7509	Vlachos and Dermatas [41] 0.7468	5.1	Yes
Local IDM info. rate 0.7612	Vlachos and Dermatas [41] 0.7468	18	Yes
Local IDM info. rate 0.7644	Vlachos and Dermatas [41] 0.7468	22	Yes
Local IDM info. rate 0.7454	Mendonca et al. [84] 0.7315	17	Yes
Local IDM info. rate 0.7509	Mendonca et al. [84] 0.7315	23.8	Yes
Local IDM info. rate 0.7612	Mendonca et al. [84] 0.7315	36.7	Yes
Local IDM info. rate 0.7644	Mendonca et al. [84] 0.7315	40.7	Yes
Local IDM info. rate 0.7454	Staal et al. [22] 0.7345	13.4	Yes
Local IDM info. rate 0.7509	Staal et al. [22] 0.7345	20.2	Yes
Local IDM info. rate 0.7612	Staal et al. [22] 0.7345	33	Yes
Local IDM info. rate 0.7644	Staal et al. [22] 0.7345	37.1	Yes
Local IDM info. rate 0.7612	Xiao et al. [83] 0.7513	12.4	Yes
Local IDM info. rate 0.7644	Xiao et al. [83] 0.7513	16.4	Yes

Table A.19: Comparison of the average sensitivity rates 0.7313, 0.7375, 0.7397, 0.7560, 0.7632 and 0.7650 achieved by adaptive thresholding technique based ASM information using green channel with the other techniques in the literature on DRIVE database.

Method I	**Method II**	**Z-Score**	**Significant**
Least of the Six Avg. Sens. rates of Local ASM Info. 0.7313	Chaudhuri et al. [26] 0.3357	426.2	Yes
„„	Jiang and Mojon [38] 0.6399	105.8	Yes
„„	Zana and Klein [40] 0.6971	40.7	Yes
„„	Martinez-Perez et al. [135] 0.6389	106.9	Yes
„„	Niemeijer et al [35] 0.7145	20.2	Yes
„„	Yin et al. [87] 0.6522	92.1	Yes
Least of the Five Avg. Sens. rates of Local ASM Info. 0.7375	Mendonca et al. [84] 0.7315	7.3	Yes
Least of the Three Avg. Sens. rates of Local ASM Info. 0.7560	Vlachos and Dermatas [41] 0.7468	11.4	Yes
Local ASM info. rate 0.7375	Staal et al. [22] 0.7345	3.7	Yes
Local ASM info. rate 0.7397	Staal et al. [22] 0.7345	6.3	Yes
Local ASM info. rate 0.7560	Staal et al. [22] 0.7345	26.5	Yes
Local ASM info. rate 0.7632	Staal et al. [22] 0.7345	35.6	Yes
Local ASM info. rate 0.7650	Staal et al. [22] 0.7345	37.8	Yes
Local ASM info. rate 0.7560	Xiao et al. [83] 0.7513	5.9	Yes
Local ASM info. rate 0.7632	Xiao et al. [83] 0.7513	14.9	Yes
Local ASM info. rate 0.7650	Xiao et al. [83] 0.7513	17.2	Yes

Table A.20: Comparison of the average sensitivity rates 0.7501, 0.7506, 0.7530, 0.7613, 0.7661 and 0.7662 achieved by adaptive thresholding technique based IDM information using green channel with the other techniques in the literature on STARE database.

Method I	**Method II**	**Z-Score**	**Significant**
Least of the Six Avg. Sens. rates of Local IDM Info. 0.7501	Hoover et al. [21] 0.6751	96.4	Yes
„„	Staal et al. [22] 0.6970	69	Yes
„„	Mendonca et al. [84] 0.7123	49.6	Yes
Local IDM info. rate 0.7612	Xiao et al. [83] 0.7147	46.5	Yes
„„	Yin et al. [87] 0.7248	33.4	Yes

Table A.21: Comparison of the average sensitivity rates 0.7427, 0.7428, 0.7458, 0.7542, 0.7626 and 0.7641 achieved by adaptive thresholding technique based ASM information using green channel with the other techniques in the literature on STARE database.

Method I	**Method II**	**Z-Score**	**Significant**
Least of the Six Avg. Sens. rates of Local IDM Info. 0.7427	Hoover et al. [21] 0.6751	86.5	Yes
„„	Staal et al. [22] 0.6970	59.2	Yes
„„	Mendonca et al. [84] 0.7123	39.7	Yes
„„	Xiao et al. [83] 0.7147	36.6	Yes
„„	Yin et al. [87] 0.7248	23.5	Yes

Table A.22: Comparison of the average accuracy rates 0.9532, 0.9506, 0.9521, 0.9511, 0.9502 and 0.9468 achieved by adaptive thresholding technique based IDM information with the other techniques in the literature on DRIVE database.

Method I	**Method II**	**Z-Score**	**Significant**
Least of the Six Avg. Acc. rates of Local IDM Info. 0.9468	Chaudhuri et al. [26] 0.8773	82.7	Yes
„„	Jiang and Mojon [38] 0.9212	34.7	Yes
„„	Zana and Klein [40] 0.9377	13.1	Yes
„„	Martinez-Perez et al. [135] 0.9181	38.5	Yes
„„	Niemeijer et al [35] 0.9416	7.6	Yes
„„	Yin et al. [87] 0.9267	27.8	Yes
„„	Vlachos and Dermatas [41] 0.9285	25.5	Yes
„„	Szpak and Tapamo [138] 0.9299	23.7	Yes
Least of the Five Avg. Acc. rates of Local IDM Info. 0.9502	Akram and Khan [46] 0.9469	5	Yes
„„	Marin et al. [28] 0.9452	7.6	Yes
„„	Soares et al.[23] 0.9466	5.5	Yes
„„	Wang et al. [43] 0.9461	6.2	Yes
„„	Mendonca et al. [84] 0.9463	5.9	Yes
„„	Staal et al. [22] 0.9442	9	Yes
„„	Human Observer [131] 0.9473	4.4	Yes

Table A.23: Comparison of the average accuracy rates 0.9511, 0.9503, 0.9488, 0.9477, 0.9461 and 0.9449 achieved by adaptive thresholding technique based ASM information with the other techniques in the literature on DRIVE database.

Method I	**Method II**	**Z-Score**	**Significant**
Least of the Six Avg. Acc. rates of Local ASM Info. 0.9449	Chaudhuri et al. [26] 0.8773	80	Yes
„„	Jiang and Mojon [38] 0.9212	31.9	Yes
„„	Zana and Klein [40] 0.9377	10.3	Yes
„„	Martinez-Perez et al. [135] 0.9181	35.7	Yes
„„	Niemeijer et al [35] 0.9416	4.8	Yes
„„	Yin et al. [87] 0.9267	25	Yes
„„	Vlachos and Dermatas [41] 0.9285	22.7	Yes
„„	Szpak and Tapamo [138] 0.9299	20.9	Yes
Least of the Five Avg. Acc. rates of Local ASM Info. 0.9461	Staal et al. [22] 0.9442	2.8	Yes
Least of the Four Avg. Acc. rates of Local ASM Info. 0.9477	Marin et al. [28] 0.9452	3.7	Yes
„„	Soares et al.[23] 0.9466	1.7	Yes
„„	Mendonca et al. [84] 0.9463	2.1	Yes
„„	Wang et al. [43] 0.9461	2.4	Yes
Least of the Three Avg. Acc. rates of Local ASM Info. 0.9488	Akram and Khan [46] 0.9469	2.9	Yes
„„	Human Observer [131] 0.9473	2.3	Yes

Table A.24: Comparison of the average accuracy rates 0.9511, 0.9526, 0.9546, 0.9529, 0.9550 and 0.9492 achieved by adaptive thresholding technique based IDM information with the other techniques in the literature on STARE database.

Method I	**Method II**	**Z-Score**	**Significant**
Least of the Six Avg. Acc. rates of Local ASM Info. 0.9492	Hoover et al. [21] 0.9275	38.1	Yes
„„	Jiang and Mojon [38] 0.9009	77.6	Yes
„„	Mendonca et al. [84] 0.9479	2.5	Yes
„„	Xiao et al. [83] 0.9476	3.1	Yes
„„	Yin et al. [87] 0.9412	14.9	Yes
„„	Soares et al.[23] 0.9480	2.3	Yes
„„	Human Observer [132] 0.9354	25	Yes
Least of the Four Avg. Acc. rates of Local ASM Info. 0.9526	Staal et al. [22] 0.9516	2	Yes
„„	Akram and Khan [46] 0.9502	4.7	Yes
0.9529	Marin et al. [28] 0.9526	0.6	No
0.9546	Marin et al. [28] 0.9526	4	Yes
0.9550	Marin et al. [28] 0.9526	4.8	Yes
0.9526	Wang et al. [43] 0.9521	1	No
0.9529	Wang et al. [43] 0.9521	1.6	No
0.9546	Wang et al. [43] 0.9521	5	Yes
0.9550	Wang et al. [43] 0.9521	5.8	Yes

Table A.25: Comparison of the average accuracy rates 0.9504, 0.9500, 0.9485, 0.9457, 0.9510 and 0.9500 achieved by adaptive thresholding technique based ASM information with the other techniques in the literature on STARE database.

Method I	**Method II**	**Z-Score**	**Significant**
Least of the Six Avg. Acc. rates of Local ASM Info. 0.9457	Hoover et al. [21] 0.9275	31.6	Yes
„„	Jiang and Mojon [38] 0.9009	71.2	Yes
„„	Yin et al. [87] 0.9412	8.2	Yes
„„	Human Observer [132] 0.9354	18.4	Yes
0.9485	Mendonca et al. [84] 0.9479	1.1	No
0.9500	Mendonca et al. [84] 0.9479	4	Yes
0.9500	Mendonca et al. [84] 0.9479	4	Yes
0.9504	Mendonca et al. [84] 0.9479	4.8	Yes
0.9510	Mendonca et al. [84] 0.9479	6	Yes
Least of the Five Avg. Acc. rates of Local ASM Info. 0.9485	Xiao et al. [83] 0.9476	1.7	Yes
0.9485	Soares et al.[23] 0.9480	1	No
0.9500	Soares et al.[23] 0.9480	3.8	Yes
0.9500	Soares et al.[23] 0.9480	3.8	Yes
0.9504	Soares et al.[23] 0.9480	4.6	Yes
0.9510	Soares et al.[23] 0.9480	5.8	Yes
0.9504	Akram and Khan [46] 0.9502	0.4	No
0.9510	Akram and Khan [46] 0.9502	1.6	No

Table A.26: Comparison of the average sensitivity rates 0.6315, 0.6459, 0.7079, 0.7399, 0.7518 and 0.7581 achieved by K-means clustering methods with the other techniques in the literature on DRIVE database.

Method I	**Method II**	**Z-Score**	**Significant**
Least of the Four Avg. Sens. rates K-means clustering 0.7079	Chaudhuri et al. [26] 0.3357	400.4	Yes
„„	Jiang and Mojon [38] 0.6399	78	Yes
„„	Zana and Klein [40] 0.6971	12.7	Yes
„„	Martinez-Perez et al. [135] 0.6389	79.1	Yes
„„	Yin et al. [87] 0.6522	64.2	Yes
Least of the Two Avg. Sens. rates K-means clustering 0.7518	Vlachos and Dermatas [41] 0.7468	6.2	Yes
Least of the Three Avg. Sens. rates K-means clustering 0.7399	Niemeijer et al [35] 0.7145	30.6	Yes
„„	Mendonca et al. [84] 0.7315	10.2	Yes
„„	Staal et al. [22] 0.7345	6.6	Yes
0.7518	Xiao et al. [83] 0.7513	0.6	No
0.7581	Xiao et al. [83] 0.7513	8.5	Yes

Table A.27: Comparison of the average sensitivity rates 0.6516, 0.6567, 0.6979, 0.7372, 0.7666 and 0.7772 achieved by K-means clustering methods with the other techniques in the literature on STARE database.

Method I	**Method II**	**Z-Score**	**Significant**
Least of the Four Avg. Sens. rates K-means clustering 0.6979	Hoover et al. [21] 0.6751	28.6	Yes
0.6979	Staal et al. [22] 0.6970	1.1	No
0.7372	Staal et al. [22] 0.6970	51.9	Yes
0.7666	Staal et al. [22] 0.6970	91.3	Yes
0.7772	Staal et al. [22] 0.6970	105.9	Yes
Least of the Four Avg. Sens. rates K-means clustering 0.7372	Mendonca et al. [84] 0.7123	32.4	Yes
„„	Xiao et al. [83] 0.7147	29.3	Yes
„„	Yin et al. [87] 0.7248	16.3	Yes

Table A.28: Comparison of the average accuracy rates 0.9555, 0.9555, 0.9523, 0.9556, 0.9531 and 0.9516 achieved by K-means clustering methods with the other techniques in the literature on DRIVE database.

Method I	**Method II**	**Z-Score**	**Significant**
Least of the Six Avg. Acc. rates K-means clustering 0.9516	Chaudhuri et al. [26] 0.8773	89.5	Yes
„„	Jiang and Mojon [38] 0.9212	42	Yes
„„	Zana and Klein [40] 0.9377	20.5	Yes
„„	Martinez-Perez et al. [135] 0.9181	45.7	Yes
„„	Niemeijer et al [35] 0.9416	15	Yes
„„	Yin et al. [87] 0.9267	35.1	Yes
„„	Vlachos and Dermatas [41] 0.9285	32.8	Yes
„„	Szpak and Tapamo [138] 0.9299	31	Yes
„„	Akram and Khan [46] 0.9469	7.2	Yes
„„	Marin et al. [28] 0.9452	9.7	Yes
„„	Soares et al.[23] 0.9466	7.7	Yes
„„	Wang et al. [43] 0.9461	8.4	Yes
„„	Mendonca et al. [84] 0.9463	8.1	Yes
„„	Staal et al. [22] 0.9442	11.2	Yes
„„	Human Observer [131] 0.9473	6.6	Yes

Table A.29: Comparison of the average accuracy rates 0.9312, 0.9344, 0.9340, 0.9509, 0.9500 and 0.9492 achieved by K-means clustering methods with the other techniques in the literature on STARE database.

Method I	**Method II**	**Z-Score**	**Significant**
Least of the Six Avg. Acc. rates K-means clustering 0.9312	Hoover et al. [21] 0.9275	6.1	Yes
„„	Jiang and Mojon [38] 0.9009	46.2	Yes
Least of the Three Avg. Acc. rates K-means clustering 0.9492	Mendonca et al. [84] 0.9479	2.5	Yes
„„	Xiao et al. [83] 0.9476	3.1	Yes
„„	Yin et al. [87] 0.9412	14.9	Yes
„„	Soares et al.[23] 0.9480	2.3	Yes
„„	Human Observer [132] 0.9354	25	Yes
0.9509	Akram and Khan [46] 0.9502	1.4	No

Table A.30: Comparison of the AUC rates 0.9682, 0.9707, 0.9699, 0.9713, 0.9722 and 0.9705 achieved by the proposed adaptive thresholding techniques based on different IDM information with the other techniques in the literature on DRIVE database.

Method I	**Method II**	**Z-Score**	**Significant**
Least of the Six AUC rates of Local IDM Info. 0.9682	Chaudhuri et al. [26] 0.7878	296.2	Yes
„„	Jiang and Mojon [38] 0.9114	128.3	Yes
„„	Zana and Klein [40] 0.8984	150.3	Yes
„„	Ricci and Perfetti [20] 0.9558	34.9	Yes
„„	Niemeijer et al [35] 0.9294	94.6	Yes
„„	Staal et al. [22] 0.9520	44.5	Yes
„„	Wang et al. [43] 0.9543	38.7	Yes
„„	Marin et al. [28] 0.9588	26.9	Yes
„„	Akram and Khan [46] 0.963	15.3	Yes
„„	Soares et al. [23] 0.9614	19.8	Yes

Table A.31: Comparison of the AUC rates 0.9642, 0.9705, 0.9741, 0.9818, 0.9819 and 0.9824 achieved by the proposed adaptive thresholding techniques based on different IDM information with the other techniques in the literature on STARE database.

Method I	**Method II**	**Z-Score**	**Significant**
Least of the Six AUC rates of Local IDM Info. 0.9642	Jiang and Mojon [38] 0.929	91	Yes
„„	Ricci and Perfetti [20] 0.9602	12.2	Yes
„„	Staal et al. [22] 0.9614	8.6	Yes
Least of the Five AUC rates of Local IDM Info. 0.9705	Wang et al. [43] 0.9682	7.8	Yes
„„	Soares et al. [23] 0.9671	11.4	Yes
Least of the Four AUC rates of Local IDM Info. 0.9741	Akram and Khan [46] 0.970	14.5	Yes
Least of the Three AUC rates of Local IDM Info. 0.9818	Marin et al. [28] 0.9769	20	Yes

Table A.32: Comparison of the AUC rates 0.9656, 0.9711, 0.9698, 0.9734, 0.9680 and 0.9658 achieved by the proposed adaptive thresholding techniques based on different ASM information with the other techniques in the literature on DRIVE database.

Method I	**Method II**	**Z-Score**	**Significant**
Least of the Six AUC rates of Local ASM Info. 0.9656	Chaudhuri et al. [26] 0.7878	290.6	Yes
„„	Jiang and Mojon [38] 0.9114	121.2	Yes
„„	Zana and Klein [40] 0.8984	143.5	Yes
„„	Ricci and Perfetti [20] 0.9558	27.1	Yes
„„	Niemeijer et al [35] 0.9294	87.2	Yes
„„	Staal et al. [22] 0.9520	36.8	Yes
„„	Wang et al. [43] 0.9543	31	Yes
„„	Marin et al. [28] 0.9588	19.2	Yes
„„	Akram and Khan [46] 0.963	7.5	Yes
„„	Soares et al. [23] 0.9614	12	Yes

Table A.33: Comparison of the AUC rates 0.9671, 0.9681, 0.9695, 0.9745, 0.9781 and 0.9782 achieved by the proposed adaptive thresholding techniques based on different ASM information with the other techniques in the literature on STARE database.

Method I	**Method II**	**Z-Score**	**Significant**
Least of the Six AUC rates of Local ASM Info. 0.9671	Jiang and Mojon [38] 0.929	99.8	Yes
„„	Ricci and Perfetti [20] 0.9602	21.4	Yes
„„	Staal et al. [22] 0.9614	17.8	Yes
Least of the Four AUC rates of Local ASM Info. 0.9695	Wang et al. [43] 0.9682	4.4	Yes
„„	Soares et al. [23] 0.9671	8	Yes
Least of the Three AUC rates of Local ASM Info. 0.9745	Akram and Khan [46] 0.970	15.9	Yes
Least of the Two AUC rates of Local ASM Info. 0.9781	Marin et al. [28] 0.9769	4.7	Yes

Table A.34: Comparison of the AUC rates 0.9735, 0.9749 and 0.9758 achieved K-means clustering methods with the other techniques in the literature on DRIVE database.

Method I	**Method II**	**Z-Score**	**Significant**
Least of the Three AUC rates K-means clustering 0.9719	Chaudhuri et al. [26] 0.7878	304.3	Yes
„„	Jiang and Mojon [38] 0.9114	138.7	Yes
„„	Zana and Klein [40] 0.8984	160.4	Yes
„„	Ricci and Perfetti [20] 0.9558	46.4	Yes
„„	Niemeijer et al [35] 0.9294	105.5	Yes
„„	Staal et al. [22] 0.9520	55.9	Yes
„„	Wang et al. [43] 0.9543	50.2	Yes
„„	Marin et al. [28] 0.9588	38.5	Yes
„„	Akram and Khan [46] 0.963	27	Yes
„„	Soares et al. [23] 0.9614	31.4	Yes

Table A.35: Comparison of the AUC rates 0.9463, 0.9728, 0.9734 and 0.9756 achieved K-means clustering methods with the other techniques in the literature on STARE database.

Method I	**Method II**	**Z-Score**	**Significant**
Least of the Three AUC rates K-means clustering 0.9728	Jiang and Mojon [38] 0.929	117.8	Yes
„„	Ricci and Perfetti [20] 0.9602	40.7	Yes
„„	Staal et al. [22] 0.9614	37.2	Yes
„„	Wang et al. [43] 0.9682	15.8	Yes
„„	Akram and Khan [46] 0.970	9.8	Yes
„„	Soares et al. [23] 0.9671	19.4	Yes

Table A.36: Comparison of the maximum correlation value 0.80 achieved by non-normalised metric (TI_{freq2}) with the normalised metric (TI_{freq1}) and distance metric L_{curve}/L_{chord} of the vessel tortuosity measures.

Method I	**Method II**	**Z-Score**	**Significant**
non-normalised metric (TI_{freq2}) 0.80	distance metric L_{curve}/L_{chord} 0.73	12	Yes
non-normalised metric (TI_{freq2}) 0.80	normalised metric (TI_{freq1}) 0.73	12	Yes

Appendix B

Additional Dataset

MESSIDOR database was established to facilitate studies on computer-assisted diagnoses of diabetic retinopathy. The database is made up of 1200 eye fundus coloured retinal images acquired by 3 ophthalmologic departments using a color video 3CCD camera on a Topcon TRC NW6 non-mydriatic retinograph with a 45 degree field of view. The retinal images were captured using 8 bits per color plane at 1440*960, 2240*1488 or 2304*1536 pixels. Eight hundred images were acquired with pupil dilation (one drop of Tropicamide at 0.5%) and four hundred images without dilation. This database has no ground truth for vessel segmentation but rather provides grading for diabetic retinopathy and risk of macular endema. We randomly selected 261 coloured retinal images from this database and the vessel segmentation techniques proposed in this research are applied on the dataset.

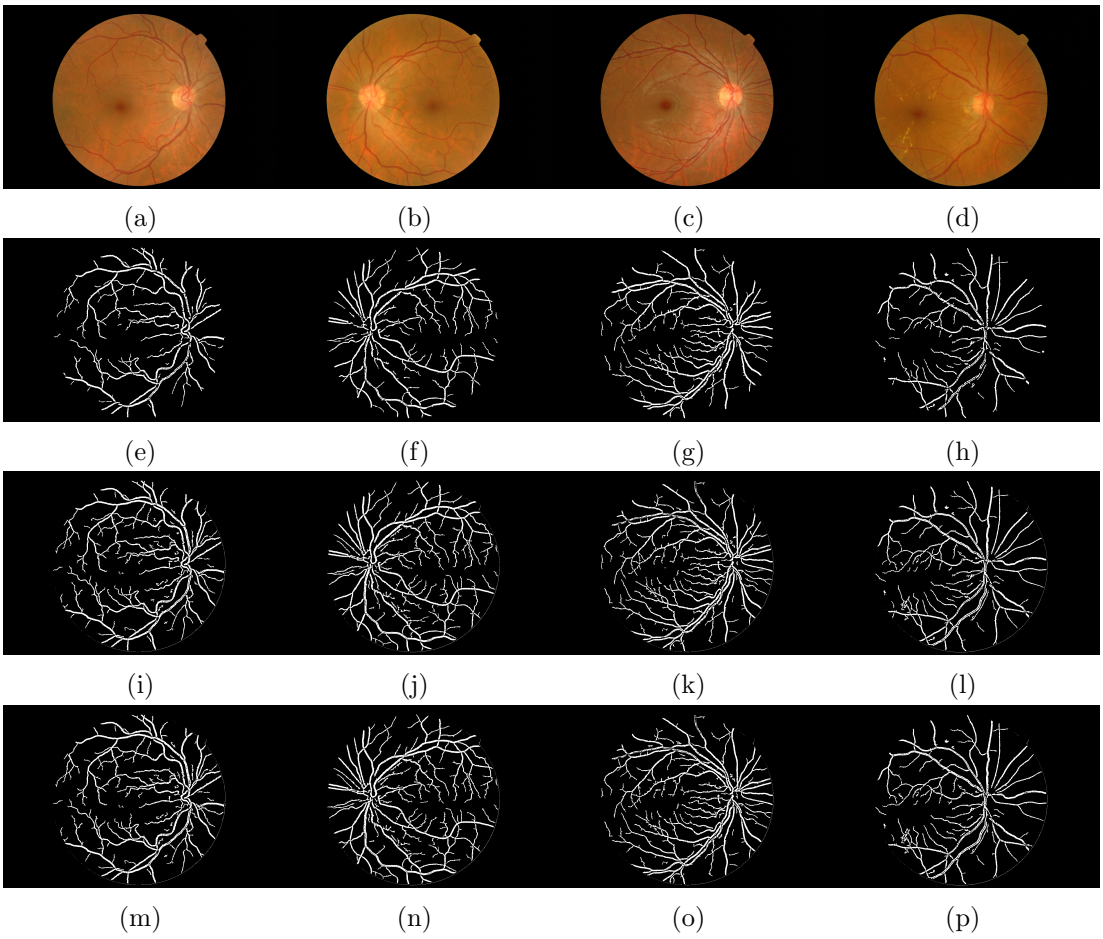

Figure B.1: Difference Images Combined With K-Means Clustering Technique for Vessel Segmentation on Messidor database [183]. (a) to (d) Messidor database Coloured Retinal Images. (e) to (h) Segmented Retinal Vessel Using Difference Image Based on Median Filter Combined With K-Means Clustering Technique. (i) to (l) Segmented Retinal Vessel Using Difference Image Based on Median Filter and Gaussian Filter Combined With K-Means Clustering Technique. (m) to (p) Segmented Retinal Vessel Using Difference Image Based on Median Filter and Mean Filter Combined With K-Means Clustering Technique.

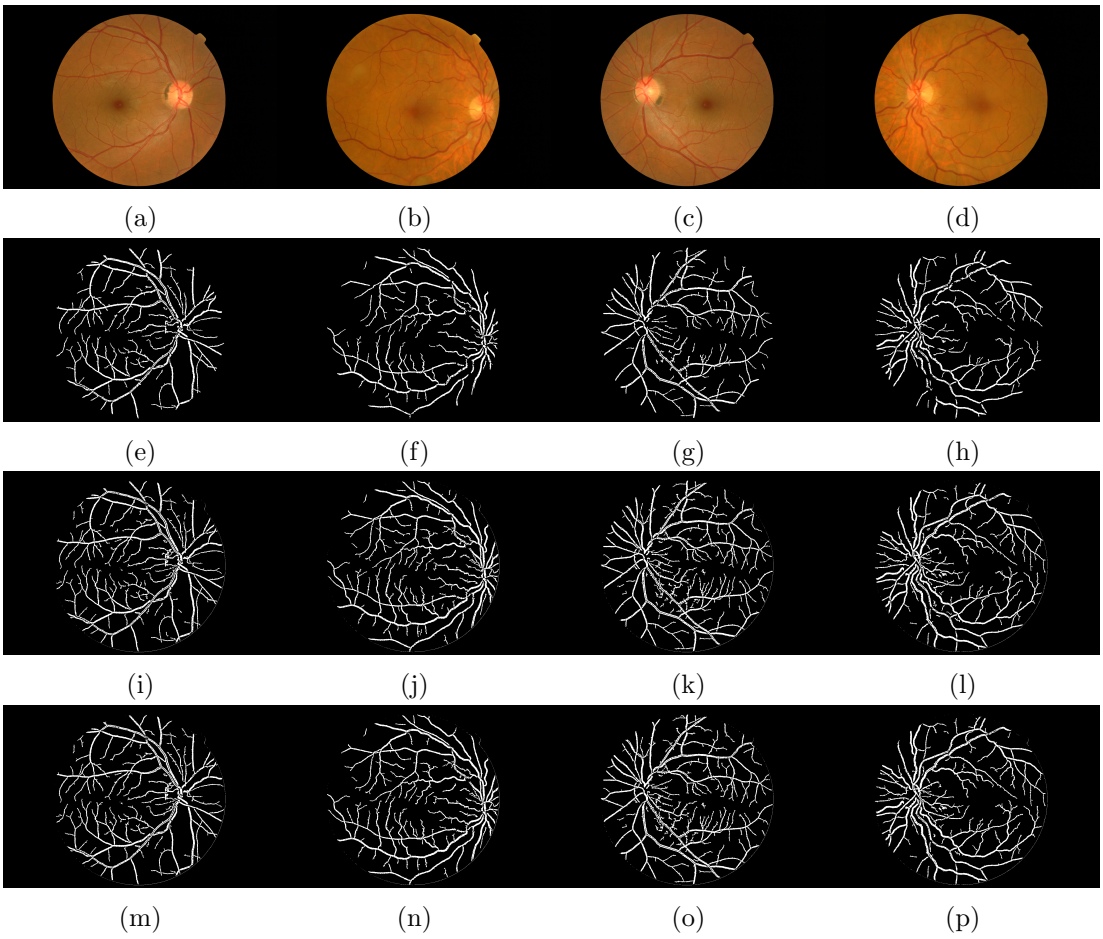

Figure B.2: Difference Images Combined With K-Means Clustering Technique for Vessel Segmentation on Messidor database [183]. (a) to (d) Messidor database Coloured Retinal Images. (e) to (h) Segmented Retinal Vessel Using Difference Image Based on Median Filter Combined With K-Means Clustering Technique. (i) to (l) Segmented Retinal Vessel Using Difference Image Based on Median Filter and Gaussian Filter Combined With K-Means Clustering Technique. (m) to (p) Segmented Retinal Vessel Using Difference Image Based on Median Filter and Mean Filter Combined With K-Means Clustering Technique.

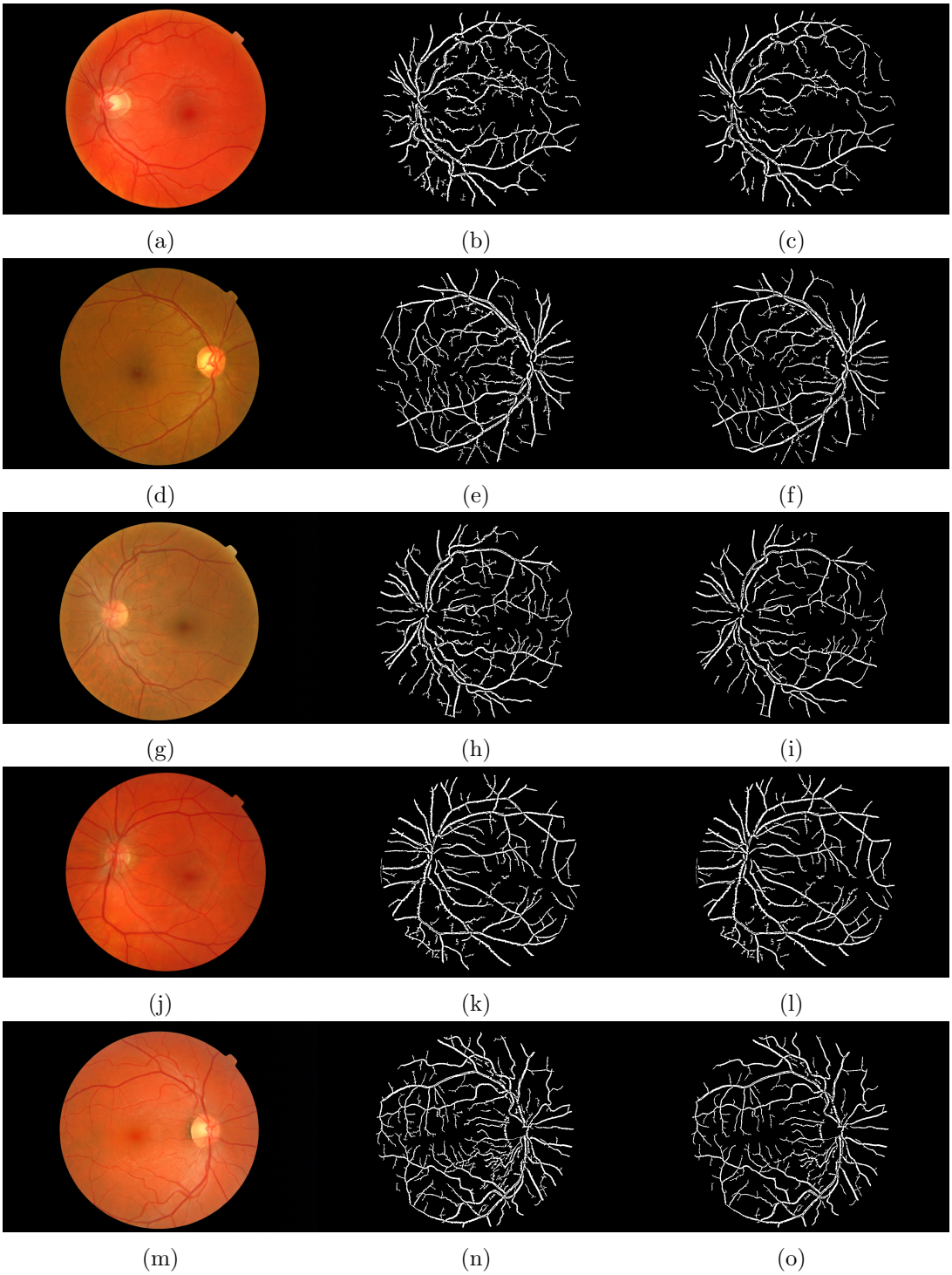

Figure B.3: Adaptive Thresholding Techniques for Vessel Segmentation on Messidor database [183]. (a), (d), (g), (j) & (m) Messidor database Coloured Retinal Images. (b), (e), (h), (k) & (n) Segmented Retinal Vessel Using Adaptive Thresholding Based on Energy Information. (c), (f), (i), (l) & (o) Segmented Retinal Vessel Using Adaptive Thresholding Based on IDM Information.

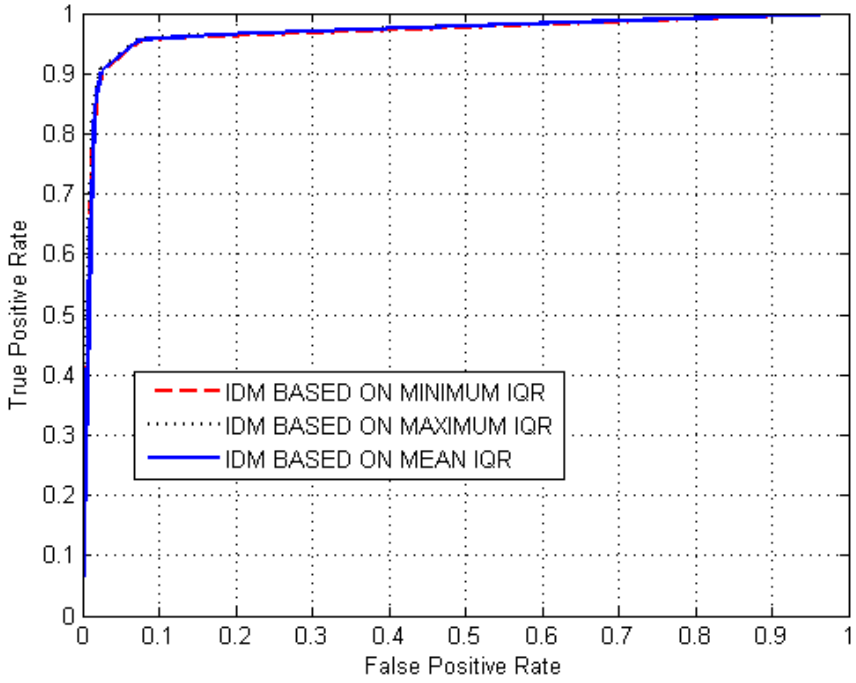

Figure B.4: ROC Curves Showing the Performance of each of the Adaptive Thresholding Based on IDM Inter-Quartile Range Information on DRIVE

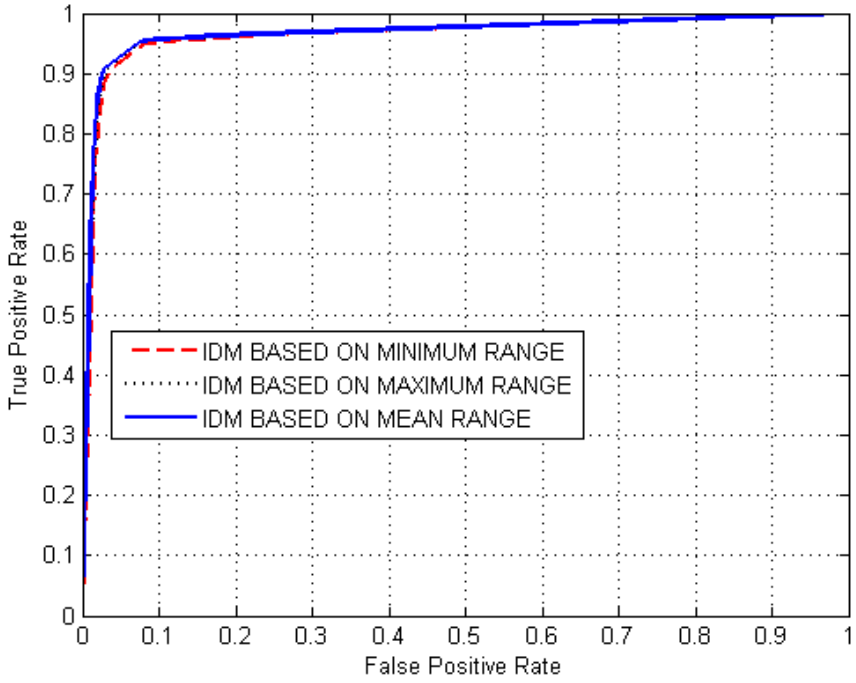

Figure B.5: ROC Curves Showing the Performance of each of the Adaptive Thresholding Based on IDM Range Information on DRIVE

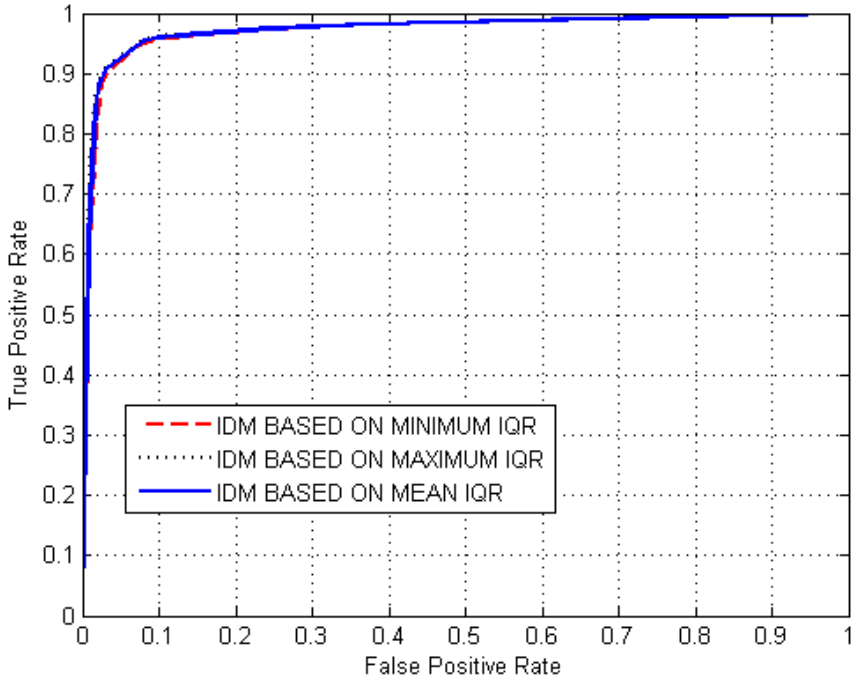

Figure B.6: ROC Curves Showing the Performance of each of the Adaptive Thresholding Based on IDM Inter-Quartile Range Information on STARE

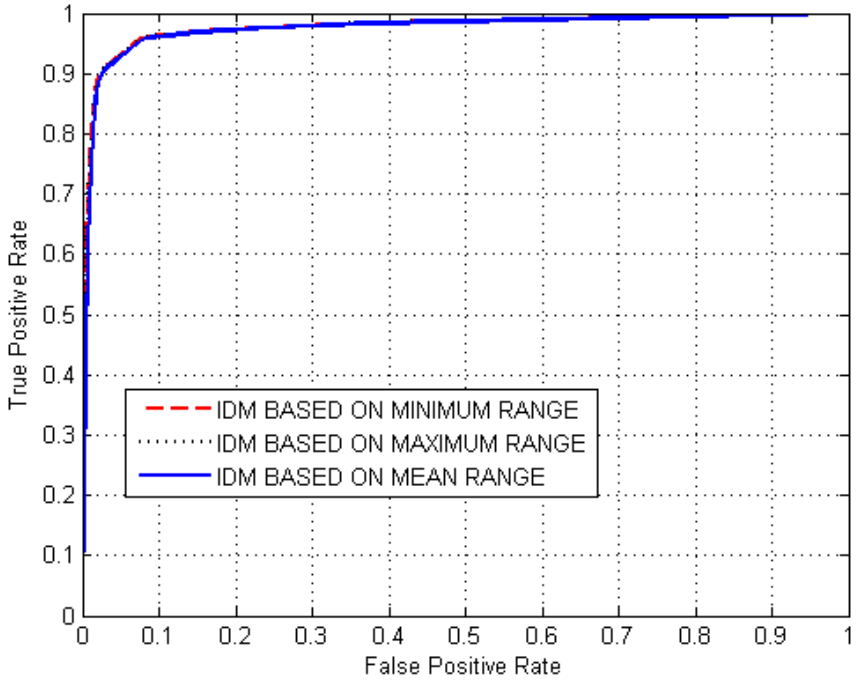

Figure B.7: ROC Curves Showing the Performance of each of the Adaptive Thresholding Based on IDM Range Information on STARE

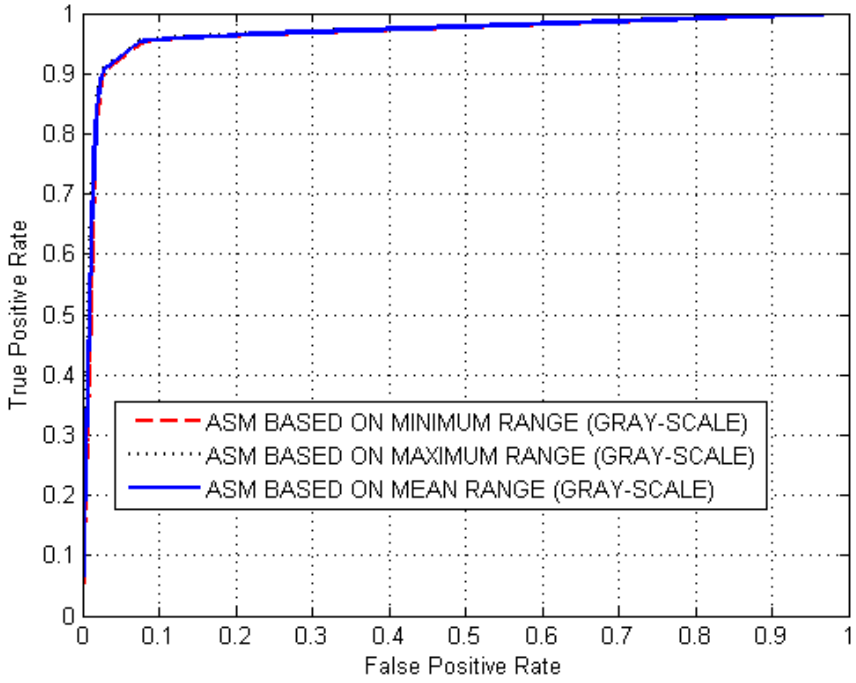

Figure B.8: ROC Curves Showing the Performance of each of the Adaptive Thresholding Based on ASM Using Grey-Scale on DRIVE

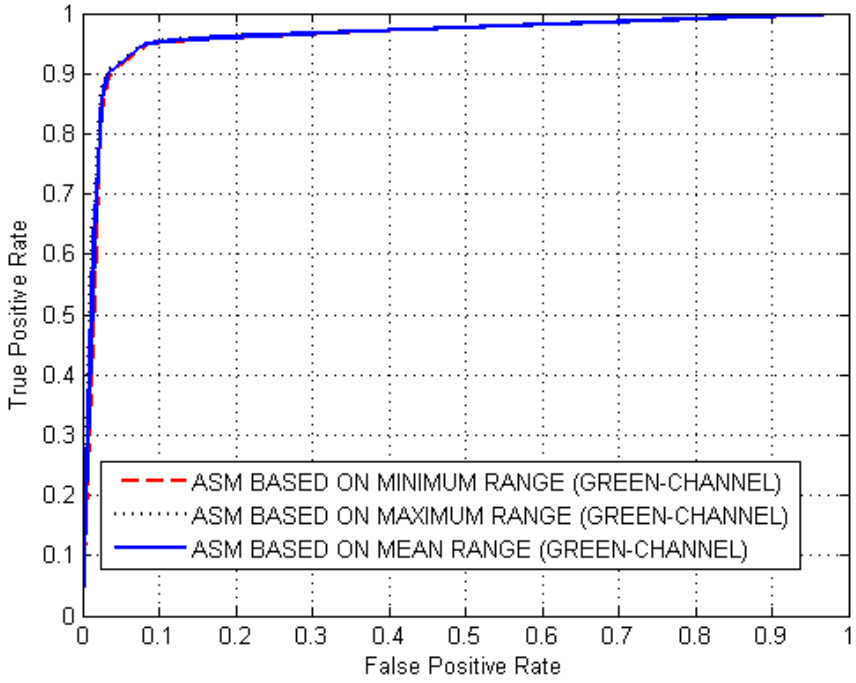

Figure B.9: ROC Curves Showing the Performance of each of the Adaptive Thresholding Based on ASM Using Green-Channel on DRIVE

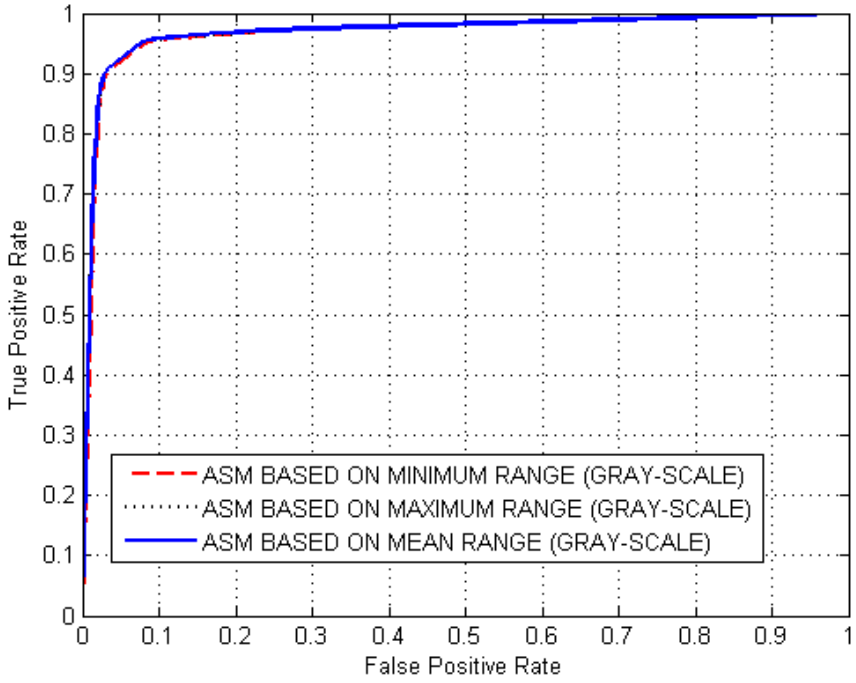

Figure B.10: ROC Curves Showing the Performance of each of the Adaptive Thresholding Based on ASM Using Grey-Scale on STARE

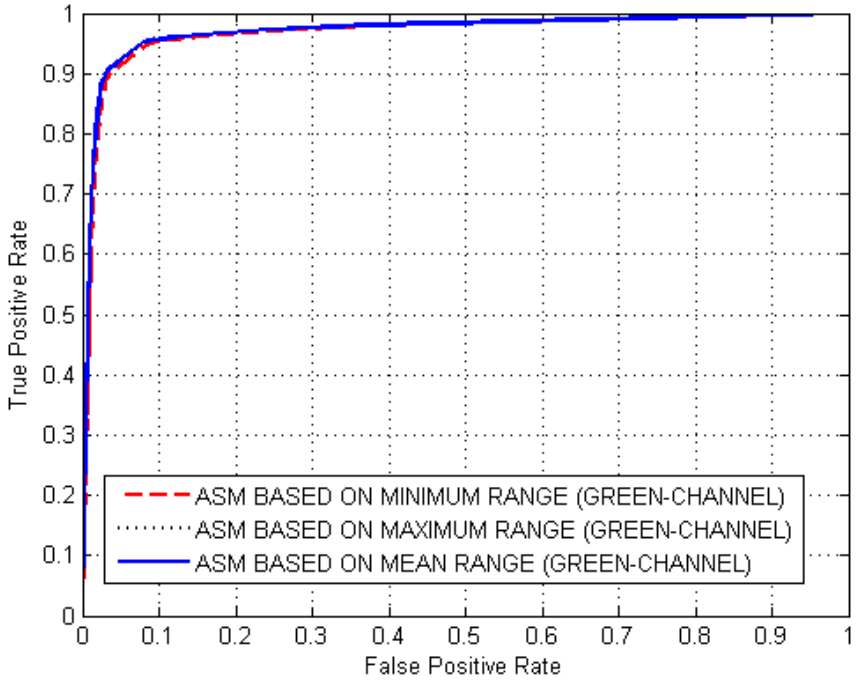

Figure B.11: ROC Curves Showing the Performance of each of the Adaptive Thresholding Based on ASM Using Green-Channel on STARE

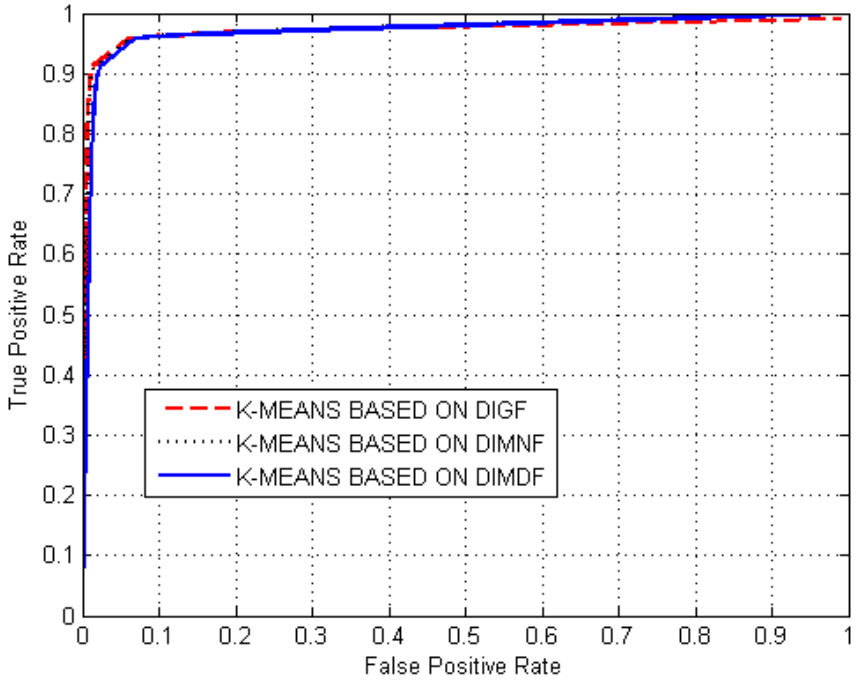

Figure B.12: ROC Curves Showing the Performance of K-Means Clustering Combined with each of the Single Difference Image on DRIVE

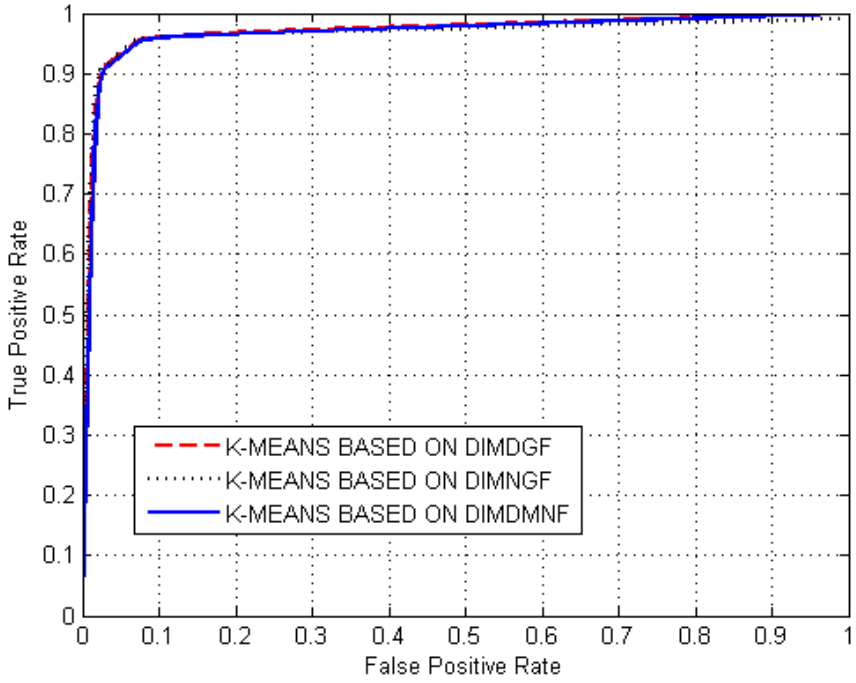

Figure B.13: ROC Curves Showing the Performance of K-Means Clustering Combined with each of the Hybrid Difference Image on DRIVE

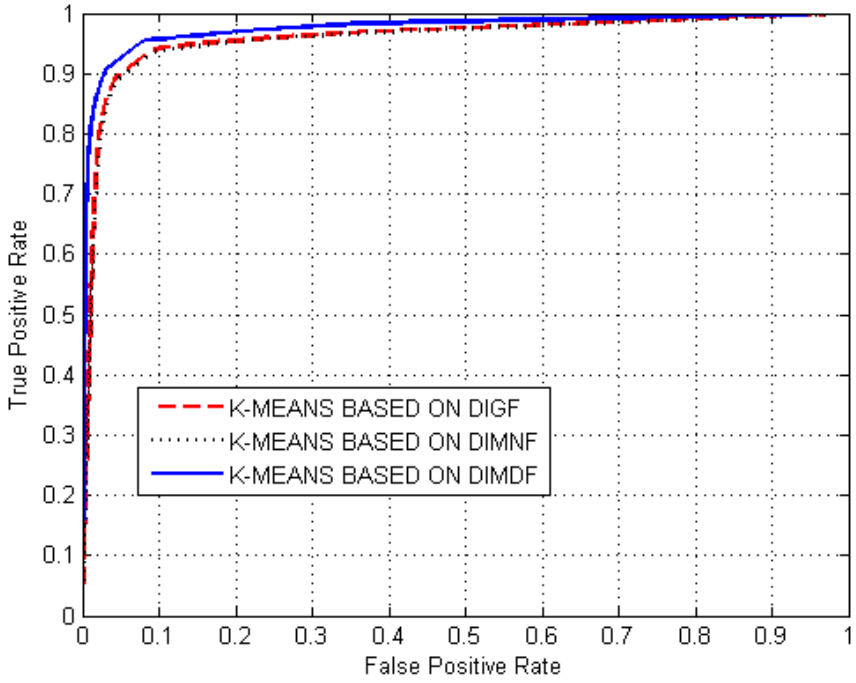

Figure B.14: ROC Curves Showing the Performance of K-Means Clustering Combined with each of the Single Difference Image on STARE

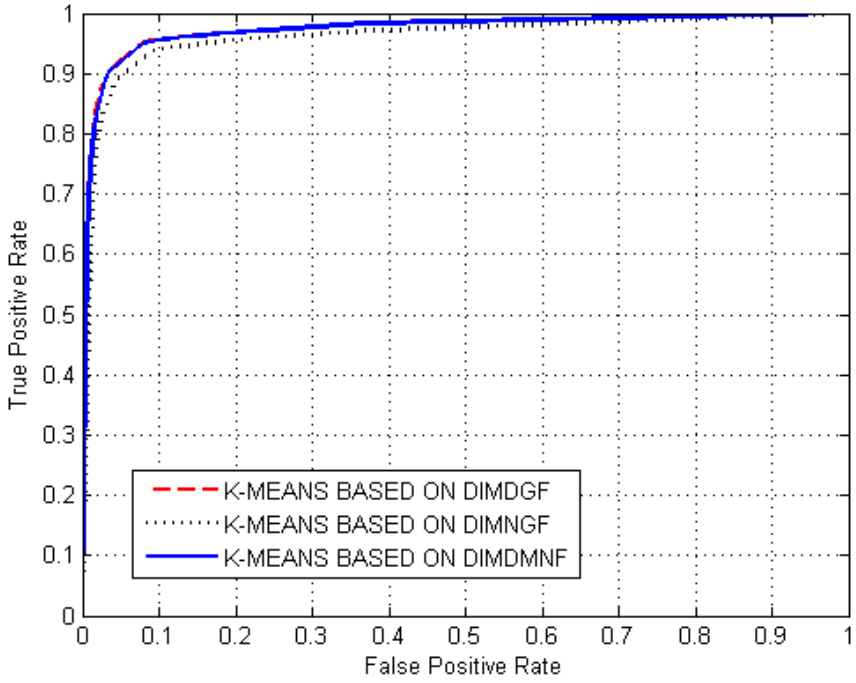

Figure B.15: ROC Curves Showing the Performance of K-Means Clustering Combined with each of the Hybrid Difference Image on STARE

References

[1] T. Mapayi, S. Viriri, and J.-R. Tapamo, "A new adaptive thresholding technique for retinal vessel segmentation based on local homogeneity information," in *Image and Signal Processing*. Springer, 2014, pp. 558–567.

[2] J. Westwood, H. Hoffman, D. Stredney, and S. Weghorst, "Computer-assisted image-guided surgery using the regulus navigator," *Medicine Meets Virtual Reality: Art, Science, Technology: Healthcare (r) evolution*, vol. 50, p. 103, 1998.

[3] H. Breithaupt, "Seeing is understanding," *EMBO reports*, vol. 7, no. 5, pp. 467–470, 2006.

[4] D. Cantor-Rivera and T. Peters, "Pervasive medical imaging applications–current challenges and possible alternatives," in *Paper presented at IEEE Conference on E-Health, Networking, Application and Services, Lyon*, 2010.

[5] A. Rajaei and L. Rangarajan, "Matching and retrieval of medical images," in *International Symposium on Distributed Computing and Artificial Intelligence*. Springer, 2011, pp. 27–33.

[6] R. Snyderman and R. S. Williams, "Prospective medicine: the next health care transformation," *Academic Medicine*, vol. 78, no. 11, pp. 1079–1084, 2003.

[7] C. M. Holloway, A. Easson, J. Escallon, W. L. Leong, M. L. Quan, M. Reedjik, F. C. Wright, and D. R. McCready, "Technology as a force for improved diagnosis and treatment of breast disease," *Canadian Journal of Surgery*, vol. 53, no. 4, p. 268, 2010.

[8] N. I. Parikh and R. S. Vasan, "Assessing the clinical utility of biomarkers in medicine," 2007.

[9] M. Matsui, T. Tashiro, K. Matsumoto, and S. Yamamoto, "[a study on automatic and quantitative diagnosis of fundus photographs. i. detection of contour line of retinal blood vessel images on color fundus photographs (author's transl)]." *Nippon Ganka Gakkai Zasshi*, vol. 77, no. 8, pp. 907–918, 1973.

[10] C. Baudoin, B. Lay, and J. Klein, "Automatic detection of microaneurysms in diabetic fluorescein angiography." *Revue d'épidémiologie et de santé publique*, vol. 32, no. 3-4, pp. 254–261, 1983.

[11] T. Teng, M. Lefley, and D. Claremont, "Progress towards automated diabetic ocular screening: a review of image analysis and intelligent systems for diabetic retinopathy," *Medical and Biological Engineering and Computing*, vol. 40, no. 1, pp. 2–13, 2002.

[12] N. Patton, T. M. Aslam, T. MacGillivray, I. J. Deary, B. Dhillon, R. H. Eikelboom, K. Yogesan, and I. J. Constable, "Retinal image analysis: concepts, applications and potential," *Progress in retinal and eye research*, vol. 25, no. 1, pp. 99–127, 2006.

[13] M. D. Abràmoff, M. K. Garvin, and M. Sonka, "Retinal imaging and image analysis," *Biomedical Engineering, IEEE Reviews in*, vol. 3, pp. 169–208, 2010.

[14] O. Faust, R. Acharya, E. Y.-K. Ng, K.-H. Ng, and J. S. Suri, "Algorithms for the automated detection of diabetic retinopathy using digital fundus images: a review," *Journal of medical systems*, vol. 36, no. 1, pp. 145–157, 2012.

[15] M. A. Pérez, B. B. Bruce, N. J. Newman, and V. Biousse, "The use of retinal photography in non-ophthalmic settings and its potential for neurology," *The neurologist*, vol. 18, no. 6, p. 350, 2012.

[16] B. Li and H. K. Li, "Automated analysis of diabetic retinopathy images: Principles, recent developments, and emerging trends," *Current diabetes reports*, vol. 13, no. 4, pp. 453–459, 2013.

[17] A. G. Marrugo, M. S. Millán, G. Cristóbal, S. Gabarda, M. Sorel, and F. Sroubek, "Image analysis in modern ophthalmology: from acquisition to computer assisted diagnosis and telemedicine," in *SPIE Photonics Europe*. International Society for Optics and Photonics, 2012, pp. 84 360C–84 360C.

[18] Y. Yang and S. Huang, "Image segmentation by fuzzy c-means clustering algorithm with a novel penalty term," *Computing and Informatics*, vol. 26, no. 1, pp. 17–31, 2012.

[19] D. C. Klonoff and D. M. Schwartz, "An economic analysis of interventions for diabetes." *Diabetes care*, vol. 23, no. 3, pp. 390–404, 2000.

[20] E. Ricci and R. Perfetti, "Retinal blood vessel segmentation using line operators and support vector classification," *Medical Imaging, IEEE Transactions on*, vol. 26, no. 10, pp. 1357–1365, 2007.

[21] A. Hoover, V. Kouznetsova, and M. Goldbaum, "Locating blood vessels in retinal images by piecewise threshold probing of a matched filter response," *Medical Imaging, IEEE Transactions on*, vol. 19, no. 3, pp. 203–210, 2000.

[22] J. Staal, M. D. Abràmoff, M. Niemeijer, M. A. Viergever, and B. van Ginneken, "Ridge-based vessel segmentation in color images of the retina," *Medical Imaging, IEEE Transactions on*, vol. 23, no. 4, pp. 501–509, 2004.

[23] J. V. Soares, J. J. Leandro, R. M. Cesar, H. F. Jelinek, and M. J. Cree, "Retinal vessel segmentation using the 2-d gabor wavelet and supervised classification," *Medical Imaging, IEEE Transactions on*, vol. 25, no. 9, pp. 1214–1222, 2006.

[24] M. M. Fraz, P. Remagnino, A. Hoppe, B. Uyyanonvara, A. R. Rudnicka, C. G. Owen, and S. A. Barman, "An ensemble classification-based approach applied to retinal blood vessel segmentation," *Biomedical Engineering, IEEE Transactions on*, vol. 59, no. 9, pp. 2538–2548, 2012.

[25] M. M. Fraz, A. R. Rudnicka, C. G. Owen, and S. A. Barman, "Delineation of blood vessels in pediatric retinal images using decision trees-based ensemble classification," *International journal of computer assisted radiology and surgery*, pp. 1–17, 2013.

[26] S. Chaudhuri, S. Chatterjee, N. Katz, M. Nelson, and M. Goldbaum, "Detection of blood vessels in retinal images using two-dimensional matched filters," *IEEE Transactions on medical imaging*, vol. 8, no. 3, pp. 263–269, 1989.

[27] T. Chanwimaluang and G. Fan, "An efficient blood vessel detection algorithm for retinal images using local entropy thresholding," in *Circuits and Systems, 2003. ISCAS'03. Proceedings of the 2003 International Symposium on*, vol. 5. IEEE, 2003, pp. V–21.

[28] D. Marín, A. Aquino, M. E. Gegúndez-Arias, and J. M. Bravo, "A new supervised method for blood vessel segmentation in retinal images by using gray-level and moment invariants-based features," *Medical Imaging, IEEE Transactions on*, vol. 30, no. 1, pp. 146–158, 2011.

[29] R. Nekovei and Y. Sun, "Back-propagation network and its configuration for blood vessel detection in angiograms," *Neural Networks, IEEE Transactions on*, vol. 6, no. 1, pp. 64–72, 1995.

[30] C. Sinthanayothin, J. F. Boyce, H. L. Cook, and T. H. Williamson, "Automated localisation of the optic disc, fovea, and retinal blood vessels from digital colour fundus images," *British Journal of Ophthalmology*, vol. 83, no. 8, pp. 902–910, 1999.

[31] A. Osareh and B. Shadgar, "Automatic blood vessel segmentation in color images of retina," *Iran. J. Sci. Technol. Trans. B: Engineering*, vol. 33, no. B2, pp. 191–206, 2009.

[32] C. A. Lupascu, D. Tegolo, and E. Trucco, "Fabc: retinal vessel segmentation using adaboost," *Information Technology in Biomedicine, IEEE Transactions on*, vol. 14, no. 5, pp. 1267–1274, 2010.

[33] B. Zhang, L. Zhang, L. Zhang, and F. Karray, "Retinal vessel extraction by matched filter with first-order derivative of gaussian," *Computers in biology and medicine*, vol. 40, no. 4, pp. 438–445, 2010.

[34] M. M. Fraz, A. Basit, and S. Barman, "Application of morphological bit planes in retinal blood vessel extraction," *Journal of digital imaging*, vol. 26, no. 2, pp. 274–286, 2013.

[35] M. Niemeijer, J. Staal, B. van Ginneken, M. Loog, and M. D. Abramoff, "Comparative study of retinal vessel segmentation methods on a new publicly available database," in *Medical Imaging 2004*. International Society for Optics and Photonics, 2004, pp. 648–656.

[36] S. Garg, J. Sivaswamy, and S. Chandra, "Unsupervised curvature-based retinal vessel segmentation," in *Biomedical Imaging: From Nano to Macro, 2007. ISBI 2007. 4th IEEE International Symposium on*. IEEE, 2007, pp. 344–347.

[37] J. I. Orlando and M. Blaschko, "Learning fully-connected crfs for blood vessel segmentation in retinal images," in *Medical Image Computing and Computer-Assisted Intervention–MICCAI 2014*. Springer, 2014, pp. 634–641.

[38] X. Jiang and D. Mojon, "Adaptive local thresholding by verification-based multithreshold probing with application to vessel detection in retinal images," *Pattern Analysis and Machine Intelligence, IEEE Transactions on*, vol. 25, no. 1, pp. 131–137, 2003.

[39] T. Chakraborti, D. K. Jha, A. S. Chowdhury, and X. Jiang, "A self-adaptive matched filter for retinal blood vessel detection," *Machine Vision and Applications*, vol. 26, no. 1, pp. 55–68.

[40] F. Zana and J.-C. Klein, "Segmentation of vessel-like patterns using mathematical morphology and curvature evaluation," *Image Processing, IEEE Transactions on*, vol. 10, no. 7, pp. 1010–1019, 2001.

[41] M. Vlachos and E. Dermatas, "Multi-scale retinal vessel segmentation using line tracking," *Computerized Medical Imaging and Graphics*, vol. 34, no. 3, pp. 213–227, 2010.

[42] V. M. Saffarzadeh, A. Osareh, and B. Shadgar, "Vessel segmentation in retinal images using multi-scale line operator and k-means clustering," *Journal of medical signals and sensors*, vol. 4, no. 2, p. 122, 2014.

[43] Y. Wang, G. Ji, P. Lin, E. Trucco *et al.*, "Retinal vessel segmentation using multiwavelet kernels and multiscale hierarchical decomposition." *Pattern Recognition*, vol. 46, no. 8, pp. 2117–2133, 2013.

[44] M. M. Fraz, P. Remagnino, A. Hoppe, B. Uyyanonvara, C. G. Owen, A. R. Rudnicka, and S. Barman, "Retinal vessel extraction using first-order derivative of gaussian and morphological processing," in *Advances in Visual Computing*. Springer, 2011, pp. 410–420.

[45] M. M. Fraz, S. Barman, P. Remagnino, A. Hoppe, A. Basit, B. Uyyanonvara, A. R. Rudnicka, and C. G. Owen, "An approach to localize the retinal blood vessels using bit planes and centerline detection," *Computer methods and programs in biomedicine*, vol. 108, no. 2, pp. 600–616, 2012.

[46] M. U. Akram and S. A. Khan, "Multilayered thresholding-based blood vessel segmentation for screening of diabetic retinopathy," *Engineering with computers*, vol. 29, no. 2, pp. 165–173, 2013.

[47] Q. Li, J. You, and D. Zhang, "Vessel segmentation and width estimation in retinal images using multiscale production of matched filter responses," *Expert Systems with Applications*, vol. 39, no. 9, pp. 7600–7610, 2012.

[48] M. A. Amin and H. Yan, "High speed detection of retinal blood vessels in fundus image using phase congruency," *Soft Computing*, vol. 15, no. 6, pp. 1217–1230, 2011.

[49] J. J. Capowski, J. A. Kylstra, and S. F. Freedman, "A numeric index based on spatial frequency for the tortuosity of retinal vessels and its application to plus disease in retinopathy of prematurity," *Retina*, vol. 15, no. 6, pp. 490–500, 1995.

[50] A. Chakravarty and J. Sivaswamy, "A novel approach for quantification of retinal vessel tortuosity using quadratic polynomial decomposition," in *Medical Informatics and Telemedicine (ICMIT), 2013 Indian Conference on.* IEEE, 2013, pp. 7–12.

[51] H. G. Scheie, "Evaluation of ophthalmoscopic changes of hypertension and arteriolar sclerosis," *AMA archives of ophthalmology*, vol. 49, no. 2, pp. 117–138, 1953.

[52] H. Azegrouz, E. Trucco, B. Dhillon, T. MacGillivray, and I. MacCormick, "Thickness dependent tortuosity estimation for retinal blood vessels," in *Engineering in Medicine and Biology Society, 2006. EMBS'06. 28th Annual International Conference of the IEEE.* IEEE, 2006, pp. 4675–4678.

[53] W. E. Hart, M. Goldbaum, B. Côté, P. Kube, and M. R. Nelson, "Measurement and classification of retinal vascular tortuosity," *International journal of medical informatics*, vol. 53, no. 2, pp. 239–252, 1999.

[54] C. Heneghan, J. Flynn, M. OKeefe, and M. Cahill, "Characterization of changes in blood vessel width and tortuosity in retinopathy of prematurity using image analysis," *Medical image analysis*, vol. 6, no. 4, pp. 407–429, 2002.

[55] W. Lotmar, A. Freiburghaus, and D. Bracher, "Measurement of vessel tortuosity on fundus photographs," *Albrecht von Graefes Archiv für klinische und experimentelle Ophthalmologie*, vol. 211, no. 1, pp. 49–57, 1979.

[56] M. E. Martinez-Perez, A. D. Hughes, A. V. Stanton, S. A. Thom, N. Chapman, A. A. Bharath, and K. H. Parker, "Retinal vascular tree morphology: a semi-automatic quantification." *IEEE transactions on bio-medical engineering*, vol. 49, no. 8, pp. 912–917, 2002.

[57] C. M. Wilson, K. D. Cocker, M. J. Moseley, C. Paterson, S. T. Clay, W. E. Schulenburg, M. D. Mills, A. L. Ells, K. H. Parker, G. E. Quinn *et al.*, "Computerized analysis of retinal vessel width and tortuosity in premature infants," *Investigative ophthalmology & visual science*, vol. 49, no. 8, pp. 3577–3585, 2008.

[58] W. E. Hart, M. Goldbaum, B. Cote, P. Kube, and M. R. Nelson, "Automated measurement of retinal vascular tortuosity." in *Proceedings of the AMIA Annual Fall Symposium*. American Medical Informatics Association, 1997, p. 459.

[59] E. Grisan, M. Foracchia, and A. Ruggeri, "A novel method for the automatic grading of retinal vessel tortuosity," *Medical Imaging, IEEE Transactions on*, vol. 27, no. 3, pp. 310–319, 2008.

[60] E. Bribiesca, "A measure of tortuosity based on chain coding," *Pattern Recognition*, vol. 46, no. 3, pp. 716–724, 2013.

[61] D. Onkaew, R. Turior, B. Uyyanonvara, N. Akinori, and C. Sinthanayothin, "Automatic retinal vessel tortuosity measurement using curvature of improved chain code," in *Electrical, Control and Computer Engineering (INECCE), 2011 International Conference on*. IEEE, 2011, pp. 183–186.

[62] I. D. Atlas, "6th edn," *International Diabetes Federation.–Brussels, Belgium*, p. 160, 2013.

[63] L. Ruta, D. Magliano, R. Lemesurier, H. Taylor, P. Zimmet, and J. Shaw, "Prevalence of diabetic retinopathy in type 2 diabetes in developing and developed countries," *Diabetic Medicine*, vol. 30, no. 4, pp. 387–398, 2013.

[64] W. H. Organization, *Action plan for the prevention of avoidable blindness and visual impairment, 2009-2013*. World Health Organization, 2010.

[65] J. W. Yau, S. L. Rogers, R. Kawasaki, E. L. Lamoureux, J. W. Kowalski, T. Bek, S.-J. Chen, J. M. Dekker, A. Fletcher, J. Grauslund *et al.*, "Global prevalence and major risk factors of diabetic retinopathy," *Diabetes care*, p. DC_111909, 2012.

[66] A. M. Joussen, T. W. Gardner, and B. Kirchhof, *Retinal vascular disease*. Springer, 2007.

[67] E. Rechtman, A. Harris, H. J. Garzozi, and T. A. Ciulla, "Pharmacologic therapies for diabetic retinopathy and diabetic macular edema," *Clinical ophthalmology (Auckland, NZ)*, vol. 1, no. 4, p. 383, 2007.

[68] V. S. Joshi, "Analysis of retinal vessel networks using quantitative descriptors of vascular morphology," 2012.

[69] T. Mapayi, S. Viriri, and J.-R. Tapamo, "Comparative study of retinal vessel segmentation based on global thresholding techniques," *Computational and Mathematical Methods in Medicine*, vol. 2015, 2015.

[70] G. Committee *et al.*, "2012 semdsa guideline for the management of type 2 diabetes mellitus," *Journal of Endocrinology, Metabolism and Diabetes of South Africa*, vol. 17, no. 1, pp. S1–S94, 2012.

[71] K. Gergely and A. Gerinec, "Retinopathy of prematurity–epidemics, incidence, prevalence, blindness." *Bratislavske lekarske listy*, vol. 111, no. 9, pp. 514–517, 2009.

[72] C. Gilbert, "Retinopathy of prematurity: a global perspective of the epidemics, population of babies at risk and implications for control," *Early human development*, vol. 84, no. 2, pp. 77–82, 2008.

[73] G. E. Quinn, C. Gilbert, B. A. Darlow, and A. Zin, "Retinopathy of prematurity: an epidemic in the making," *Chin Med J (Engl)*, vol. 123, no. 20, pp. 2929–37, 2010.

[74] S. Varughese, C. Gilbert, C. Pieper, and C. Cook, "Retinopathy of prematurity in south africa: an assessment of needs, resources and requirements for screening programmes," *British Journal of Ophthalmology*, vol. 92, no. 7, pp. 879–882, 2008.

[75] C. Gilbert, "Changing challenges in the control of blindness in children," *Eye*, vol. 21, no. 10, pp. 1338–1343, 2007.

[76] A. L. Ells, J. M. Holmes, W. F. Astle, G. Williams, D. A. Leske, M. Fielden, B. Uphill, P. Jennett, and M. Hebert, "Telemedicine approach to screening for severe retinopathy of prematurity: a pilot study," *Ophthalmology*, vol. 110, no. 11, pp. 2113–2117, 2003.

[77] T. Mapayi, S. Viriri, and J.-R. Tapamo, "Retinal vessel segmentation based on k-means clustering and difference image," in *Proceedings of the 2014 Pattern Recognition Association of South Africa (PRASA), RobMech and AfLaT International Joint Symposium, Cape Town, South Africa*, 2014, pp. 53–58.

[78] E. J. Sussman, W. G. Tsiaras, and K. A. Soper, "Diagnosis of diabetic eye disease," *Jama*, vol. 247, no. 23, pp. 3231–3234, 1982.

[79] L. Verma, G. Prakash, and H. K. Tewari, "Diabetic retinopathy: time for action. no complacency please!" *BULLETIN-WORLD HEALTH ORGANIZATION*, vol. 80, no. 5, pp. 419–419, 2002.

[80] T. Mapayi, S. Viriri, and J.-R. Tapamo, "Adaptive thresholding technique for retinal vessel segmentation based on glcm-energy information," *Computational and mathematical methods in medicine*, vol. 2015, 2015.

[81] A. P. Condurache and T. Aach, "Vessel segmentation in 2d-projection images using a supervised linear hysteresis classifier," in *Pattern Recognition, 2006. ICPR 2006. 18th International Conference on*, vol. 1. IEEE, 2006, pp. 343–346.

[82] M. G. Cinsdikici and D. Aydın, "Detection of blood vessels in ophthalmoscope images using mf/ant (matched filter/ant colony) algorithm," *Computer methods and programs in biomedicine*, vol. 96, no. 2, pp. 85–95, 2009.

[83] Z. Xiao, M. Adel, and S. Bourennane, "Bayesian method with spatial constraint for retinal vessel segmentation," *Computational and mathematical methods in medicine*, vol. 2013, 2013.

[84] A. M. Mendonca and A. Campilho, "Segmentation of retinal blood vessels by combining the detection of centerlines and morphological reconstruction," *Medical Imaging, IEEE Transactions on*, vol. 25, no. 9, pp. 1200–1213, 2006.

[85] E. Bullitt, G. Gerig, S. M. Pizer, W. Lin, and S. R. Aylward, "Measuring tortuosity of the intracerebral vasculature from mra images," *Medical Imaging, IEEE Transactions on*, vol. 22, no. 9, pp. 1163–1171, 2003.

[86] S. Pal and P. Bhowmick, "Estimation of discrete curvature based on chain-code pairing and digital straightness," in *Image Processing (ICIP), 2009 16th IEEE International Conference on*. IEEE, 2009, pp. 1097–1100.

[87] Y. Yin, M. Adel, and S. Bourennane, "Automatic segmentation and measurement of vasculature in retinal fundus images using probabilistic formulation," *Computational and mathematical methods in medicine*, vol. 2013, 2013.

[88] M. S. Miri and A. Mahloojifar, "Retinal image analysis using curvelet transform and multistructure elements morphology by reconstruction," *Biomedical Engineering, IEEE Transactions on*, vol. 58, no. 5, pp. 1183–1192, 2011.

[89] H. Huang, D. R. Aberle, R. Lufkin, E. G. Grant, W. N. Hanafee, and H. Kangarloo, "Advances in medical imaging," *Annals of internal medicine*, vol. 112, no. 3, pp. 203–220, 1990.

[90] D. L. Pham, C. Xu, and J. L. Prince, "Current methods in medical image segmentation 1," *Annual review of biomedical engineering*, vol. 2, no. 1, pp. 315–337, 2000.

[91] C. Cuspidi and C. Sala, "Retinal wall-to-lumen ratio: a new marker of endothelial function?" *Journal of hypertension*, vol. 29, no. 1, pp. 33–35, 2011.

[92] D. Huang, E. A. Swanson, C. P. Lin, J. S. Schuman, W. G. Stinson, W. Chang, M. R. Hee, T. Flotte, K. Gregory, C. A. Puliafito *et al.*, "Optical coherence tomography," *Science*, vol. 254, no. 5035, pp. 1178–1181, 1991.

[93] J. S. Schuman, M. R. Hee, A. V. Arya, T. Pedut-Kloizman, C. A. Puliafito, J. G. Fujimoto, and E. A. Swanson, "Optical coherence tomography: a new tool for glaucoma diagnosis," *Current opinion in ophthalmology*, vol. 6, no. 2, pp. 89–95, 1995.

[94] J. S. Schuman, M. R. Hee, C. A. Puliafito, C. Wong, T. Pedut-Kloizman, C. P. Lin, E. Hertzmark, J. A. Izatt, E. A. Swanson, and J. G. Fujimoto, "Quantification of nerve fiber layer thickness in normal and glaucomatous eyes using optical coherence tomography: a pilot study," *Archives of Ophthalmology*, vol. 113, no. 5, pp. 586–596, 1995.

[95] H. R. Novotny and D. L. Alvis, "A method of photographing fluorescence in circulating blood in the human retina," *Circulation*, vol. 24, no. 1, pp. 82–86, 1961.

[96] G. Klein, R. Baumgartner, and R. Flower, "An image processing approach to characterizing choroidal blood flow." *Investigative ophthalmology & visual science*, vol. 31, no. 4, pp. 629–637, 1990.

[97] E. H. Meijering, K. J. Zuiderveld, and M. A. Viergever, "Image registration for digital subtraction angiography," *International Journal of Computer Vision*, vol. 31, no. 2-3, pp. 227–246, 1999.

[98] J. Schallek and D. Ts'o, "Blood contrast agents enhance intrinsic signals in the retina: evidence for an underlying blood volume component," *Investigative ophthalmology & visual science*, vol. 52, no. 3, pp. 1325–1335, 2011.

[99] C. M. Poloschek and E. E. Sutter, "The fine structure of multifocal erg topographies," *Journal of vision*, vol. 2, no. 8, p. 5, 2002.

[100] R. J. Antcliff, M. R. Stanford, D. S. Chauhan, E. M. Graham, D. J. Spalton, J. S. Shilling, J. Marshall *et al.*, "Comparison between optical coherence tomography and fundus fluorescein angiography for the detection of cystoid macular edema in patients with uveitis," *Ophthalmology*, vol. 107, no. 3, pp. 593–599, 2000.

[101] V. Gupta, H. A. Al-Dhibi, and J. F. Arevalo, "Retinal imaging in uveitis," *Saudi Journal of Ophthalmology*, vol. 28, no. 2, pp. 95–103, 2014.

[102] Euroeye and F. Docchio, *Introduction to ocular fluorometry*, 1997.

[103] C. Bellmann, G. Rubin, S. Kabanarou, A. Bird, and F. Fitzke, "Fundus autofluorescence imaging compared with different confocal scanning laser ophthalmoscopes," *British journal of ophthalmology*, vol. 87, no. 11, pp. 1381–1386, 2003.

[104] C. Framme, J. Roider, H. G. Sachs, R. Brinkmann, and V.-P. Gabel, "Noninvasive imaging and monitoring of retinal pigment epithelium patterns using fundus autofluorescence-review," *current Medical Imaging reviews*, vol. 1, no. 1, pp. 89–103, 2005.

[105] S. Schmitz-Valckenberg, F. G. Holz, A. C. Bird, and R. F. Spaide, "Fundus autofluorescence imaging: review and perspectives," *Retina*, vol. 28, no. 3, pp. 385–409, 2008.

[106] M. F. Marmor, D. C. Hood, D. Keating, M. Kondo, M. W. Seeliger, and Y. Miyake, "Guidelines for basic multifocal electroretinography (mferg)," *Documenta Ophthalmologica*, vol. 106, no. 2, pp. 105–115, 2003.

[107] A. C. Fok, Y. W. Yip, J. W. Ngai, and T. Y. Lai, "The use of multifocal electroretinography in the assessment of retinal toxicity caused by pharmacological agents."

[108] N. Larsen, J. Godt, M. Grunkin, H. Lund-Andersen, and M. Larsen, "Automated detection of diabetic retinopathy in a fundus photographic screening population," *Investigative ophthalmology & visual science*, vol. 44, no. 2, pp. 767–771, 2003.

[109] K. W. Tobin, E. Chaum, V. P. Govindasamy, and T. P. Karnowski, "Detection of anatomic structures in human retinal imagery," *Medical Imaging, IEEE Transactions on*, vol. 26, no. 12, pp. 1729–1739, 2007.

[110] D. Cornforth, H. J. Jelinek, J. Leandro, J. Soares, R. Cesar Jr, M. J. Cree, P. Mitchell, and T. Bossomaier, "Development of retinal blood vessel segmentation methodology using wavelet transforms for assessment of diabetic retinopathy," 2005.

[111] J. Lowell, A. Hunter, D. Steel, A. Basu, R. Ryder, E. Fletcher, and L. Kennedy, "Optic nerve head segmentation," *Medical Imaging, IEEE Transactions on*, vol. 23, no. 2, pp. 256–264, 2004.

[112] A. Osareh, "Automated identification of diabetic retinal exudates and the optic disc," Ph.D. dissertation, University of Bristol, 2004.

[113] R. Chrástek, M. Wolf, K. Donath, H. Niemann, D. Paulus, T. Hothorn, B. Lausen, R. Lämmer, C. Y. Mardin, and G. Michelson, "Automated segmentation of the optic nerve head for diagnosis of glaucoma," *Medical Image Analysis*, vol. 9, no. 4, pp. 297–314, 2005.

[114] Z. Liu, C. Opas, and S. M. Krishnan, "Automatic image analysis of fundus photograph," in *Engineering in Medicine and Biology Society, 1997. Proceedings of the 19th Annual International Conference of the IEEE*, vol. 2. IEEE, 1997, pp. 524–525.

[115] A. Pinz, S. Bernogger, P. Datlinger, and A. Kruger, "Mapping the human retina," *Medical Imaging, IEEE Transactions on*, vol. 17, no. 4, pp. 606–619, 1998.

[116] H. Li and O. Chutatape, "Automated feature extraction in color retinal images by a model based approach," *Biomedical Engineering, IEEE Transactions on*, vol. 51, no. 2, pp. 246–254, 2004.

[117] K. Akita and H. Kuga, "A computer method of understanding ocular fundus images," *Pattern recognition*, vol. 15, no. 6, pp. 431–443, 1982.

[118] A. Hoover and M. Goldbaum, "Fuzzy convergence," in *Computer Vision and Pattern Recognition, 1998. Proceedings. 1998 IEEE Computer Society Conference on.* IEEE, 1998, pp. 716–721.

[119] T. Walter and J.-C. Klein, "Segmentation of color fundus images of the human retina: Detection of the optic disc and the vascular tree using morphological techniques," in *Medical Data Analysis.* Springer, 2001, pp. 282–287.

[120] B. Wasan, A. Cerutti, S. Ford, and R. Marsh, "Vascular network changes in the retina with age and hypertension." *Journal of hypertension*, vol. 13, no. 12, pp. 1724–1728, 1995.

[121] B. V. Davitt and D. K. Wallace, "Plus disease," *Survey of ophthalmology*, vol. 54, no. 6, pp. 663–670, 2009.

[122] T. Spencer, J. A. Olson, K. C. McHardy, P. F. Sharp, and J. V. Forrester, "An image-processing strategy for the segmentation and quantification of microaneurysms in fluorescein angiograms of the ocular fundus," *Computers and biomedical research*, vol. 29, no. 4, pp. 284–302, 1996.

[123] M. J. Cree, J. A. Olson, K. C. McHardy, P. F. Sharp, and J. V. Forrester, "A fully automated comparative microaneurysm digital detection system," *Eye*, vol. 11, no. 5, pp. 622–628, 1997.

[124] G. Gardner, D. Keating, T. Williamson, and A. Elliott, "Automatic detection of diabetic retinopathy using an artificial neural network: a screening tool." *British journal of Ophthalmology*, vol. 80, no. 11, pp. 940–944, 1996.

[125] K. A. Goatman, M. J. Cree, J. A. Olson, J. V. Forrester, and P. F. Sharp, "Automated measurement of microaneurysm turnover," *Investigative ophthalmology & visual science*, vol. 44, no. 12, pp. 5335–5341, 2003.

[126] C. Sinthanayothin, J. Boyce, T. Williamson, H. Cook, E. Mensah, S. Lal, and D. Usher, "Automated detection of diabetic retinopathy on digital fundus images," *Diabetic Medicine*, vol. 19, no. 2, pp. 105–112, 2002.

[127] D. Usher, M. Dumskyj, M. Himaga, T. Williamson, S. Nussey, and J. Boyce, "Automated detection of diabetic retinopathy in digital retinal images: a tool for diabetic retinopathy screening," *Diabetic Medicine*, vol. 21, no. 1, pp. 84–90, 2004.

[128] B. M. Ege, O. K. Hejlesen, O. V. Larsen, K. Møller, B. Jennings, D. Kerr, and D. A. Cavan, "Screening for diabetic retinopathy using computer based image analysis and statistical classification," *Computer methods and programs in biomedicine*, vol. 62, no. 3, pp. 165–175, 2000.

[129] S. C. Lee, E. T. Lee, R. M. Kingsley, Y. Wang, D. Russell, R. Klein, and A. Warn, "Comparison of diagnosis of early retinal lesions of diabetic retinopathy between a computer system and human experts," *Archives of ophthalmology*, vol. 119, no. 4, pp. 509–515, 2001.

[130] A. Feroui, M. Messadi, I. Hadjidj, and A. Bessaid, "New segmentation methodology for exudate detection in color fundus images," *Journal of Mechanics in Medicine and Biology*, vol. 13, no. 01, 2013.

[131] "Research section, digital retinal image for vessel extraction (drive) database. utrecht, the netherlands, univ. med. center utrecht, image sci. inst. [online]. available: http://www.isi.uu.nl/Re-search/Databases/DRIVE."

[132] "Stare (structured analysis of the retina) projectwebsite. clemson, sc, clemson univ. [online], available: http://www.ces.clemson.edu/~ahoover/stare/," 2000.

[133] X. You, Q. Peng, Y. Yuan, Y.-m. Cheung, and J. Lei, "Segmentation of retinal blood vessels using the radial projection and semi-supervised approach," *Pattern Recognition*, vol. 44, no. 10, pp. 2314–2324, 2011.

[134] T. Yedidya and R. Hartley, "Tracking of blood vessels in retinal images using kalman filter," in *Digital Image Computing: Techniques and Applications (DICTA), 2008.* IEEE, 2008, pp. 52–58.

[135] M. E. Martínez-Pérez, A. D. Hughes, A. V. Stanton, S. A. Thom, A. A. Bharath, and K. H. Parker, "Retinal blood vessel segmentation by means of scale-space analysis and region growing," in *Medical Image Computing and Computer-Assisted Intervention–MICCAI99.* Springer, 1999, pp. 90–97.

[136] S. Jiménez, P. Alemany, I. Fondón, A. Foncubierta, B. Acha, and C. Serrano, "Automatic detection of vessels in color fundus images," *Archivos de la Sociedad Española de Oftalmología (English Edition)*, vol. 85, no. 3, pp. 103–109, 2010.

[137] Q. Li, J. You, D. Zhang, and P. Bhattacharya, "A multiscale approach to retinal vessel segmentation using gabor filters and scale multiplication," in *Systems,*

Man and Cybernetics, 2006. SMC'06. IEEE International Conference on, vol. 4. IEEE, 2006, pp. 3521–3527.

[138] Z. L. Szpak and J. R. Tapamo, "Automatic and interactive retinal vessel segmentation: pattern recognition special edition," *South African Computer Journal*, vol. 40, pp. 23–30, 2008.

[139] Y. Q. Zhao, X. H. Wang, X. F. Wang, and F. Y. Shih, "Retinal vessels segmentation based on level set and region growing," *Pattern Recognition*, vol. 47, no. 7, pp. 2437–2446, 2014.

[140] A. G. Salazar-Gonzalez, Y. Li, and X. Liu, "Retinal blood vessel segmentation via graph cut," in *Control Automation Robotics & Vision (ICARCV), 2010 11th International Conference on.* IEEE, 2010, pp. 225–230.

[141] W. Cai and A. C. Chung, "Multi-resolution vessel segmentation using normalized cuts in retinal images," in *Medical Image Computing and Computer-Assisted Intervention–MICCAI 2006.* Springer, 2006, pp. 928–936.

[142] P. Kovesi, "Image features from phase congruency," *Videre: Journal of computer vision research*, vol. 1, no. 3, pp. 1–26, 1999.

[143] T. Zhu, "Fourier cross-sectional profile for vessel detection on retinal images," *Computerized Medical Imaging and Graphics*, vol. 34, no. 3, pp. 203–212, 2010.

[144] M. Tagore, G. B. Kande, E. Rao, and B. P. Rao, "Segmentation of retinal vasculature using phase congruency and hierarchical clustering," in *Advances in Computing, Communications and Informatics (ICACCI), 2013 International Conference on.* IEEE, 2013, pp. 361–366.

[145] B. Dai, W. Bu, X. Wu, and Y. Zheng, "Retinal blood vessel detection using multiscale line filter and phase congruency."

[146] Y. A. Tolias and S. M. Panas, "A fuzzy vessel tracking algorithm for retinal images based on fuzzy clustering," *Medical Imaging, IEEE Transactions on*, vol. 17, no. 2, pp. 263–273, 1998.

[147] G. B. Kande, P. V. Subbaiah, and T. S. Savithri, "Unsupervised fuzzy based vessel segmentation in pathological digital fundus images," *Journal of Medical Systems*, vol. 34, no. 5, pp. 849–858, 2010.

[148] Y. Yang, S. Huang, and N. Rao, "An automatic hybrid method for retinal blood vessel extraction," *International Journal of Applied Mathematics and Computer Science*, vol. 18, no. 3, pp. 399–407, 2008.

[149] K. Sun, Z. Chen, S. Jiang, and Y. Wang, "Morphological multiscale enhancement, fuzzy filter and watershed for vascular tree extraction in angiogram," *Journal of medical systems*, vol. 35, no. 5, pp. 811–824, 2011.

[150] C. A. Lupaşcu, "Unsupervised segmentation of retinal vessels."

[151] A. J. Bedell, "Retinal vessel proliferation in diabetes," *Transactions of the American Ophthalmological Society*, vol. 43, p. 271, 1945.

[152] J. Kylstra, T. Wierzbicki, M. Wolbarsht, M. Landers III, and E. Stefansson, "The relationship between retinal vessel tortuosity, diameter, and transmural pressure," *Graefe's archive for clinical and experimental ophthalmology*, vol. 224, no. 5, pp. 477–480, 1986.

[153] M. Patasius, V. Marozas, A. Lukosevicius, and D. Jegelevicius, "Model based investigation of retinal vessel tortuosity as a function of blood pressure: preliminary results," in *Engineering in Medicine and Biology Society, 2007. EMBS 2007. 29th Annual International Conference of the IEEE*. IEEE, 2007, pp. 6459–6462.

[154] L. S. Lim, C. Y. Cheung, X. Lin, P. Mitchell, T. Y. Wong, and S.-M. Saw, "Influence of refractive error and axial length on retinal vessel geometric characteristics," *Investigative ophthalmology & visual science*, pp. iovs–10, 2010.

[155] M. B. Sasongko, J. J. Wang, K. C. Donaghue, N. Cheung, P. Benitez-Aguirre, A. Jenkins, W. Hsu, M.-L. Lee, and T. Y. Wong, "Alterations in retinal microvascular geometry in young type 1 diabetes," *Diabetes Care*, vol. 33, no. 6, pp. 1331–1336, 2010.

[156] G. Dougherty, M. J. Johnson, and M. D. Wiers, "Measurement of retinal vascular tortuosity and its application to retinal pathologies," *Medical & biological engineering & computing*, vol. 48, no. 1, pp. 87–95, 2010.

[157] J. K. Kristinsson, M. S. Gottfredsdóttir, and E. Stefánsson, "Retinal vessel dilatation and elongation precedes diabetic macular oedema," *British journal of ophthalmology*, vol. 81, no. 4, pp. 274–278, 1997.

[158] C. G. Owen, R. S. Newsom, A. R. Rudnicka, S. A. Barman, E. G. Woodward, and T. J. Ellis, "Diabetes and the tortuosity of vessels of the bulbar conjunctiva," *Ophthalmology*, vol. 115, no. 6, pp. e27–e32, 2008.

[159] N. Taarnhøj, I. Munch, B. Sander, L. Kessel, J. Hougaard, K. Kyvik, T. I. Sørensen, and M. Larsen, "Straight versus tortuous retinal arteries in relation to blood pressure and genetics," *British Journal of Ophthalmology*, vol. 92, no. 8, pp. 1055–1060, 2008.

[160] J. S. Wolffsohn, G. A. Napper, S.-M. Ho, A. Jaworski, and T. L. Pollard, "Improving the description of the retinal vasculature and patient history taking for monitoring systemic hypertension," *Ophthalmic and Physiological Optics*, vol. 21, no. 6, pp. 441–449, 2001.

[161] G. Dougherty and J. Varro, "A quantitative index for the measurement of the tortuosity of blood vessels," *Medical engineering & physics*, vol. 22, no. 8, pp. 567–574, 2000.

[162] E. Grisan, M. Foracchia, and A. Ruggeri, "A novel method for the automatic evaluation of retinal vessel tortuosity," in *Engineering in Medicine and Biology Society, 2003. Proceedings of the 25th Annual International Conference of the IEEE*, vol. 1. IEEE, 2003, pp. 866–869.

[163] A. W. Setiawan, T. R. Mengko, O. S. Santoso, and A. B. Suksmono, "Color retinal image enhancement using clahe," in *2013 International Conference on ICT for Smart Society (ICISS)*.

[164] M. C. Morrone and R. A. Owens, "Feature detection from local energy," *Pattern Recognition Letters*, vol. 6, no. 5, pp. 303–313, 1987.

[165] S. Venkatesh and R. Owens, "An energy feature detection scheme," in *ICIP'89: IEEE International Conference on Image Processing: conference proceedings, 5-8 September 1989, Singapore*. IEEE, 1989.

[166] S. S. Al-Amri, N. V. Kalyankar *et al.*, "Image segmentation by using threshold techniques," *arXiv preprint arXiv:1005.4020*, 2010.

[167] N. Otsu, "A threshold selection method from gray-level histograms," *Automatica*, vol. 11, no. 285-296, pp. 23–27, 1975.

[168] R. M. Haralick, K. Shanmugam, and I. H. Dinstein, "Textural features for image classification," *Systems, Man and Cybernetics, IEEE Transactions on*, no. 6, pp. 610–621, 1973.

[169] J. S. Weszka, C. R. Dyer, and A. Rosenfeld, "A comparative study of texture measures for terrain classification," *Systems, Man and Cybernetics, IEEE Transactions on*, no. 4, pp. 269–285, 1976.

[170] L.-K. Soh and C. Tsatsoulis, "Texture analysis of sar sea ice imagery using gray level co-occurrence matrices," *Geoscience and Remote Sensing, IEEE Transactions on*, vol. 37, no. 2, pp. 780–795, 1999.

[171] C.-I. Chang, K. Chen, J. Wang, and M. L. Althouse, "A relative entropy-based approach to image thresholding," *Pattern recognition*, vol. 27, no. 9, pp. 1275–1289, 1994.

[172] J. Kapur, P. K. Sahoo, and A. K. Wong, "A new method for gray-level picture thresholding using the entropy of the histogram," *Computer vision, graphics, and image processing*, vol. 29, no. 3, pp. 273–285, 1985.

[173] S.-S. Lee, S.-J. Horng, H.-R. Tsai, and Y.-H. Lee, "Image processing on a reconfigurable array of processors with wider bus networks," *Pattern recognition*, vol. 30, no. 9, pp. 1521–1532, 1997.

[174] N. R. Pal and S. K. Pal, "Entropic thresholding," *Signal processing*, vol. 16, no. 2, pp. 97–108, 1989.

[175] M. M. Mokji and S. A. R. Abu Bakar, "Adaptive thresholding based on co-occurrence matrix edge information," in *Modelling & Simulation, 2007. AMS'07. First Asia International Conference on.* IEEE, 2007, pp. 444–450.

[176] Y. Li, M. Cheriet, and C. Suen, "A threshlod selection method based on multiscale and graylevel co-occurrence matrix analysis," in *Document Analysis and Recognition, 2005. Proceedings. Eighth International Conference on.* IEEE, 2005, pp. 575–578.

[177] M. Mokji and S. Abu Bakar, "Gray level co-occurrence matrix computation based on haar wavelet," in *Computer Graphics, Imaging and Visualisation, 2007. CGIV'07.* IEEE, 2007, pp. 273–279.

[178] G. B. Coleman and H. C. Andrews, "Image segmentation by clustering," *Proceedings of the IEEE*, vol. 67, no. 5, pp. 773–785, 1979.

[179] O. R. P. Bellon, A. I. Direne, and L. Silva, "Edge detection to guide range image segmentation by clustering techniques," in *Image Processing, 1999. ICIP 99. Proceedings. 1999 International Conference on*, vol. 2. IEEE, 1999, pp. 725–729.

[180] J. C. Dunn, "A fuzzy relative of the isodata process and its use in detecting compact well-separated clusters," 1973.

[181] G. M. Foody, "Classification accuracy comparison: hypothesis tests and the use of confidence intervals in evaluations of difference, equivalence and non-inferiority," *Remote Sensing of Environment*, vol. 113, no. 8, pp. 1658–1663, 2009.

[182] M. Martínez-Pérez, A. Hughes, A. Stanton, S. Thom, A. Bharath, and K. Parker, "Scale-space analysis for the characterisation of retinal blood vessels," in *Medical image computing and computer-assisted intervention-MICCAI*, vol. 99, 1999, pp. 90–7.

[183] "Messidor, methods for evaluating segmentation and indexing techniques dedicated to retinal ophthalmology. [online], available: http://messidor.crihan.fr/index-en.php," 2004.